Methods to enhance the stability and sensitivity of NEMS biosensors

by

Wei Zheng

A thesis submitted in partial fulfillment of the requirements for the degree of

Doctor of Philosophy

in

MEMS and Nanosystems

Department of Electrical and Computer Engineering
University of Alberta

Abstract

Mass sensitive mechanical resonator based biosensors are a promising label free biological sensing platform due to the capability for high sensitivity, fast response, accurate and real time measurement, integration with traditional electronics and flexible readout techniques. With the advancement of top down nano fabrication techniques, the dimensions of mechanical resonators scale from the micrometer down to the nanometer scale. Silicon carbonitride (SiCN) nanomechanical string resonator biosensors are advantageous in terms of large array integration, extremely high sensitivity and potential for multiple targets detection.

However, there are two bottle-neck issues that have limited this type of biosensors from moving out of research labs and using in clinical applications. First, the biological detection sensitivity is determined by the mass of the string itself. Traditional methods of reducing the size of the strings are limited by lithography. Second, the commonly used surface modification techniques are either chemically unstable on SiCN surfaces or biologically incompatible, which causes instability and unreliability of the biosensing system. In this work, two novel methods have been proposed and implemented to solve these two problems and enhance the performance of this type of biosensors.

First, a novel type of porous nanostring has been fabricated to reduce the mass of the string while avoiding the limitations of electron beam lithography (EBL). A helium ion beam was used to perform post-fabrication modification of the nanomechanical resonators. More precisely, arrays of pores were milled by ion beam along the length of glassy nanostrings. This post-fabrication method has the advantage of flexible and precise control over the dimensions, locations and the numbers of the milled patterns while with a high yield. The porous nanostrings had reduced mass and

increased surface adsorption area. This method provides an alternative technique to achieve small-mass string and opens a new route to enhance the detection sensitivity of mechanical resonator based biosensors.

In order to solve the second problem, diazonium salt reduction induced aryl film grafting was used, for the first time, on the SiCN nanostrings for bio-functionalization. This chemistry provides strong chemical adhesion and long term stability. First, diazonium chemistry was used to modify the surface of bare SiCN chip. The strong interfacial chemical bonding between the aryl film and SiCN surfaces was verified by X-ray photoelectron spectroscopy. Rabbit immunoglobulin G (IgG) sandwich immunoassays, with FITC and AuNP labels respectively, were performed on the modified SiCN surfaces. Scanning electron microscopic and confocal microscopic inspection of the samples showed uniform and dense coverage of the detection target on the samples. After this initial verification, the diazonium chemistry was adopted to bio-functionalize SiCN nanostring arrays. Anti-rabbit IgG and rabbit IgG were respectively immobilized onto diazonium modified nanostrings as probe and target. Immobilization of the probe and target were individually successfully observed by the significant downshifts of mechanical resonant frequencies of the nanostrings. A high resolution helium ion microscope was used to inspect the functionalized nanostrings and further verify the grafting of the analyte molecules on the nanostrings. As a proof of concept, diaznonium chemistry was demonstrated to be an effective modification method to functionalize SiCN nanostring mechanical resonator for its use as biosensor.

These strategies enhance the detection sensitivity and stability of nanomechanical biosensors and potentially pave the way for the clinical applications.

Preface

This thesis is an original work by Wei Zheng. The work has been published in three journal papers, in which Wei was the lead author and mainly responsible for the experiment design and implementation.

Acknowledgements

At the beginning of composing my dissertation, the very first part I choose to write was the acknowledgements. When it finally came to the stage of finalizing my PhD program, in a country located on the other end of the earth to my home country, my mind is often drawn into the memory of the past five years' study and research journey.

My first acknowledgement is given to my supervisor, Dr. Stephane Evoy. The accomplishment of this thesis would not have been possible without his continuous confidence, trust, support and patience all through my doctoral research program. I feel fortunate to have walked into Dr. Evoy's office and expressed my interest to join his group in September 2011. The three minutes talk with him totally changed my career path. Now I know I made the correct decision. At that time, I was full of enthusiasm and keen to learn about nanotechnology, but had zero experience in a cleanroom environment. Compared with experienced students, I was like a piece of blank white paper and thus often questioned my capability to make a successful chip. It was Dr. Evoy who offered me trust and support, opened the door of nanotechnology world to me, and provided me with the opportunity to work in NanoFab. During my doctoral research journey, he has always given me freedom and encouraged me to explore topics that interest me. He respected my ideas and plans, and never rejected them out of hand. He kindly guided me into more feasible and fruitful directions when my proposals were underdeveloped. He supported my experiments financially, with access to top facilities and through collaboration with other research labs. It is impossible to comprehensively describe his contributions to this thesis and my future career path with lines of simple words. The precious gift he has given to me is to turn my interest in research into love. I cherish him as a supervisor, mentor and life-long friend.

Many thanks to current and past members of Dr. Stephane Evoy's group including Remko van den Hurk for sharing his extensive knowledge and skills in biochemistry, Khaled Ramadan for sharing his expertise in finite element method, Csaba Guthy for sharing his expertise in laser interferometry, Alex Janzen for sharing his expertise in nanofabrication and Dr. Upasana Singh for their support and friendship.

I feel fortunate to have had Dr. Mark McDermott and his group members, Dr. Rongbing Du, Yong Cao as collaborators. Their consistent and dedicated collaboration and advice were critical to the success of my experiment, publications and this thesis. I owe countless thanks to this group for their help with diazonium surface chemistry and biological work.

I would like to thank Dr. Douglas Barlage for allowing me to use and program the Keithley semiconductor parameter analyzer for long term autonomous runs, as well as for the lab technician Ben Bathgate's initial training. The results got from this instrument comprised the major data for my first international conference proceedings and oral presentation, which built my confidence as a first year PhD student.

I would like to thank Dr. Steve Dew for his course microfabrication and nanofabrication topics II. This course covered extensive knowledge over all aspects of microfabrication and also included cutting edge technologies. He was a splendid teacher and spent a lot of time answering my questions after each session of the class all through that semester. I appreciate his time and patience with me, a student without any previous fabrication knowledge but full of questions. His group member Dr. Mohammad Ali Mohammad was also a wonderful collaborator and teacher, who spent long hours teaching me Raith 150 *Two* electron beam lithography from scratch, shared his expertise

of SEM, and gave suggestions on the overall process flow and each fabrication step when I just started cleanroom fabrication as a beginner.

I am grateful to the University of Alberta and the Nanofab. University education is like a transformation which reshapes students. The world-class academic, teaching and research environment of University of Alberta has enabled me to learn extensive knowledge, conduct quality research, interact with talented researchers and develop professionalism. One main reason why I chose University of Alberta for my PhD study was the Nanofab and its state-of-the-art nanofabrication facilities. Before being admitted to University of Alberta, my research concerned radio frequency circuits and devices. Without access to fabrication facilities at that time, my task was to build empirical models based on the electrical measurements of previously fabricated devices from other research labs. This made me rather curious about the fabrication technology itself and I was eager to design and make chips with my own brain and hands. The NanoFab is the place where my scientific fantasy was fully realized. In addition to serving as a platform for research and experiments, the Nanofab is also a great place to meet and talk to scientists and researchers with many different backgrounds and areas of expertise. Communicating with all of them broadened my horizons and inspired my interdisciplinary interests.

The majority of the thesis work was done in University of Alberta NanoFab. Much appreciation should go to current and past staff members for their training and technical assistance. Thanks Dr. Eric Flaim and Keith Franklin for their coordination; thanks Stephanie Bozic and Jolene Jolato for the wet etching and optical lithography training ; thanks Les Schowalter for the PVD, CVD and annealing training ; thanks Scott Munro for the SEM, plasma etch, Zygo interferometry, critical point dryer, Ellipsometer and Filmetrics training of; thanks Peng Li for the technical assistance with the helium ion microscopy; thanks Gayle Hatchard for the SEM and EDX training of; thanks

Dr. Shihong Xu, Dr Anqiang He and Dr. Dimitre Karpuzov for their assistance with the XPS and SEM measurements.

Part of the experimental work of this thesis was conducted in multiple research labs on campus. I would like to acknowledge the technical support of the following labs and people. Thanks Paul Conception and Dr. Kai Cui from the Electron Microscopy Lab of NINT (National Institute for Nanotechnology) for the SEM training; thanks Dr. Urmila Basu from the AFNS (Agricultural, Food and Nutritional Science) central labs for training on the microplate reader and the fluorescent microscopy suggestions; thanks Dr. Xuejun Sun from the Cell Imaging Facility of Cross Cancer Institute for the confocal microscopy training.

In addition, I would like to express my gratitude to many present and past colleagues and friends in University of Alberta for their friendship and support. Thanks Dr. Zhu Diao, Dr. Joe Losby, Dr. Aaron Hryciw, Yiyu Wang, Dr. Zhen Wang, Chao Chen, Meng Kan, Lingju Meng, Qiuyang Xiong, for sharing their expertise and beneficial discussions. A special note of appreciation is for graduate student advisor Ms. Pinder Bains. Thanks for her valuable advice all through my program.

I would like to give many thanks to my friends from the local industry. Most notably I want to express my appreciation for Rui Xu from Norcada for her immeasurable help with the technical tricks of wet etching, plasma etching, furnace annealing and inspection microscopy during my early days in cleanroom. Thanks Dr. Yuebin Ning and Athena Salyzyn from Norcada and Yuan Zhang from Micralyne for your friendship and encouragement. Thanks Robert Peters from Applied Nanotools, Dr. Ashok Prabhu Masilamani, previously from Applied Nanotools, and Steve Buswell from Preciseley Microtechnology for sharing your expertise in electron beam lithography. Looking into the past five years, there are so many people who have helped, assisted and influenced

my professional and personal development and growth. This makes me feel rather warm in my heart even living in this high-latitude, cold city with extremely long winters.

Last but not least, I am indebted to my parents Guojie Zheng and Shufen Kang for their spiritual support, endless love and encouragement. Their presence is the source of my strength.

Table of Contents

List of tables

List of Figures

List of Abbreviations

AFM Atomic force microscope

AlN Aluminium Nitride

AuNP Gold nanoparticle

BHF Buffered hydrofluoric acid

BOE Buffered oxide etch

BSA Bovine serum albumin

CO_2 Carbon dioxide

CPD Critical point drying

CVD Chemical vapor deposition

Da Dalton

DI Deionized water

DNA Deoxyribonucleic acid

DRIE Deep reactive ion etch

DUV Deep ultraviolet

EBL Electron beam lithography

EDX Energy-dispersive X-ray spectroscopy

ELISA Enzyme-linked immunosorbent assay

EUV Extreme ultraviolet

FIB Focused ion beam

FITC Fluorescein-5-Isothiocyanate

FTIR Fourier transform infrared spectroscopy

FWHM Full width half maximum

H_2O_2 Hydrogen peroxide

H_2SO_4 Sulfuric acid

HF Hydrofluoric acid

HSQ Hydrogen silsesquioxane

IgG Immunoglobulin G

IPA Isopropyl alcohol

KOH Potassium hydroxide

LiOH Lithium hydroxide

LPCVD Low pressure chemical vapour deposition

MEMS Microelectromechanical systems

MIBK Methyl isobutyl ketone

NaOH Sodium hydroxide

NEMS Nanoelectromechanical systems

PECVD Plasma enhanced chemical vapor deposition

PMMA Polymethylmethacrylate

PBS Phosphate buffered saline

PECVD Plasma enhanced chemical vapor deposition

PMMA Polymethyl methacrylate

PSD Position sensitive detector

QCM Quartz crystal microbalance

RF Radio frequency

RIE Reactive ion etch

PMMA Polymethylmethacrylate

PBS Phosphate Buffered Saline

PBST Phosphate Buffered Saline Tween-20

SAM Self-assembled monolayer

sccm Standard cubic centimeter per minute

SiC Silicon carbide

SiCN Silicon carbonitride

SEM Scanning electron microscope

SiN Silicon nitride (non-stoichiometric)

Si_3N_4 Silicon nitride

SOI Silicon on insulator

SPR Surface plasmon resonance

TEM Transmission electron microscopy

TiN Titanium nitride

TMAH Tetra methyl ammonium hydroxide

ToF-SIMS Time-of-Flight Secondary Ion Mass Spectrometry

UV Ultraviolet

XPS X-ray photoelectron spectroscopy

Chapter 1 Introduction

1. 1 Motivation for mechanical resonator biosensors

1. 1. 1 Biosensors

Technologies for biological detection play an important and beneficial role in many scientific research areas such as disease biomarker detection and monitoring, new drug discovery, and molecular recognition [1–7]. It is required for bio-detection technologies to provide rapid, sensitive and selective recognition of target analytes [7–10]. Established techniques include enzyme-linked immunosorbent assay (ELISA), western blotting, polymerase chain reaction (PCR), and fluorescence conjugated reagents. These methods are widely employed and are very efficient for biological analysis; however, they all require labels, like fluorescent dyes and enzymes, to identify investigated targets. The introduced labels, in some circumstances, are toxic to the biological reagents and interfere with the normal biological or chemical processes, which lead to inaccuracy of the measured results.

Label-free detections, on the contrary, do not rely on those labels or tags and keep the natural environment unperturbed for the biochemical system. Hence, compared with the traditional bioassay techniques, label-free detection offers relatively more accurate and reliable measurement results [11,12]. Intensive research has been carried out for developing novel label-free detection methods by the biochemistry, medical, and bio-engineering communities in the recent years. Current mainstream methods include surface plasmon resonance (SPR) [13–20], surface-enhanced Raman scattering (SERS) [21], mass spectroscopy (MS) [22], fiber-optic sensors [23] and mass

sensitive sensors such as quartz crystal microbalance (QCM) [24,25], surface acoustic wave (SAW) [26] and micromechanical resonators [27–33].

1.1.2 MEMS/NEMS resonator biosensors

Among the various label-free biological detection techniques, micromechanical beam resonators based platform particularly excel because of high sensitivity, fast response, accurate and real time measurement, compatibility with integrated circuits and flexibility of readout techniques [34–40]. One obvious compelling merit of the micromechanical resonator sensors is the relatively shorter detection time. The of molecular transmission is fast due to the hemi-cylindrical diffusion. This is superior to other type of label-free biosensors. For example, detection time of SPR is longer because of the planar diffusion of molecule transport.

The recent advancements in nanofabrication, especially electron beam lithography, enables the dimensions of beams to scale from the micrometer (MEMS) down to the nanometer (NEMS) range [31,41–43]. These NEMS resonaotor biosensors have received increased attention due to their sensitivity, amenability to large scale integration [35,44–48] and the possibility of multiple target detection. Compared to other label-free bio-detection methods, the NEMS resonaotor sensors have larger dynamic range, for example, in nM and pM level. Such devices assess the addition or loss of bound analytes through monitoring of the change in resonant frequency. The resonant frequency shift is proportional to the ratio of the mass of the bound molecule to the mass of the nanostring. Decreasing the mass of the strings therefore improves the sensitivity to captured analytes. Shrinking the size, especially the width, of the string is an effective approach for lowering the mass without altering the physical and mechanical parameters of the sensor system.

Multiplexed analysis can be accomplished with arrays of nanostrings by employing different molecular probes on devices of different regions, physically isolating the sub-regions, and/or taking advantage of different working modes of the devices [11,40,49–51]. Nanostring resonators can readily be scaled up to large arrays featuring up to one million devices per square centimetre [43]. High-density multiplexed assays could be accomplished by dividing such an array into sub-arrays with each sub-array targeting a specific analyte.

1.2 MEMS beam biosensors

1.2.1 Definition

A typical micromechanical beam is similar to a bridge or diving board. As shown in Fig. 1.1, there are two types of beams. In a double clamped beam, both ends are fixed to the substrate and the beam is suspended with a gap to the substrate. In a single clamped cantilever, only one end is anchored to the substrate and the other end is free to move. The mechanical behavior of the cantilevers changes with the environment conditions, such as mechanical energy, temperature, electromagnetic filed *etc.* The mechanical responses to these factors can then be transduced into measurable signals. Depending on the type of the stimuli factors they are designed to detect, mechanical cantilever sensors can be characterized as physical, chemical and biological sensors.

1.2.2 Working mode

There are typically two working modes for beam sensors: static mode and dynamic mode. Static mode refers to the bending or deformation of the cantilever cause by the differential surface stress between the two sides of the cantilever when subject to a change in physical, chemical or biological parameters. Dynamic mode beam sensors operate through resonance. Specifically, the resonant

frequency changes due to changes of the mass of the loaded beam, or of its spring constant. The theory of these two working principles is discussed in the following two sub-sections.

(a) (b)

Fig. 1.1 Basic beam types: (a) single end anchored; (b) double ends anchored

1.2.2.1 Static deflection

In a static deflection mode, analytes absorb onto only one side of the cantilever leaving the other side of cantilever unchanged, as shown in Fig. 1.2 [37,52,53]. For this purpose, the cantilever is either fabricated as a bi-material cantilever or passivated on one side. The differential stress on the two sides of cantilever induces a bending curvature of the beam. Theoretical calculations based on Stoney's formula predict the radius of cantilever's curvature as follows:

$$\frac{1}{R} = \frac{6(1-\nu)}{Et^2}\delta s \tag{1.1}$$

where R is the radius of curvature of the bent cantilever, ν is Poisson's ratio of the cantilever material, E is the Young's modulus of the material, t is the thickness of the cantilever, δ_s is the film stress. Further the cantilever displacement can be calculated as:

$$z = \frac{3L^2(1-\nu)}{Et^2}\delta s \tag{1.2}$$

where Z is the deflection of cantilever and L is the length of the cantilever.

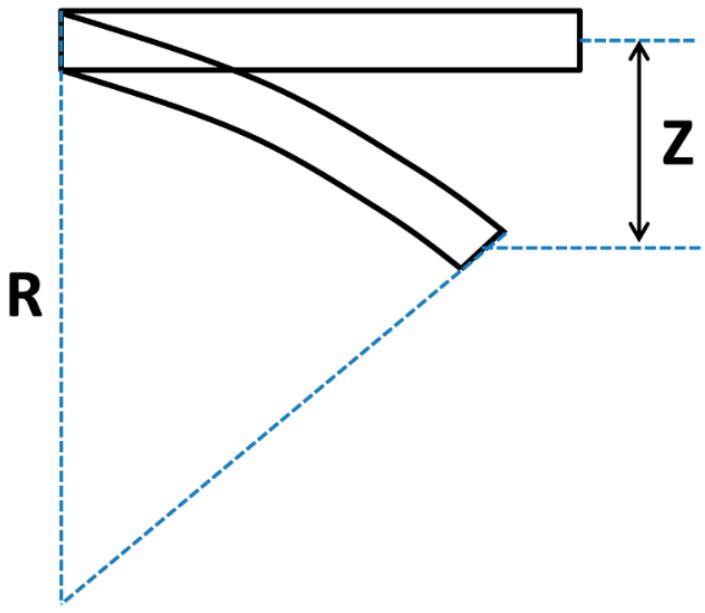

Fig. 1.2 Static deflection of cantilever

1.2.2.2 Dynamic resonance

For dynamic resonance calculations, the mechanical system of the suspended beam can be approximated as a spring-mass system. The mechanical model of the beam can then be simplified as Hook's law. The effective mass of the beam is determined by the suspended mass of the beam as well as the geometry and material of beam. In short,

$$M_{\mathrm{e}} = nm_b \tag{1.3}$$

where M_{e} is the effective mass of the beam, m_b is the total mass of the beam and n stands for a geometry-based parameter. In the case of a rectangular beam, $n = 0.24$ [37,53,54]. Then m_0 term includes both the concentrated and distributed mass of the suspended beam system.

The spring constant for a rectangular beam is determined by the material and dimensions of the beam and can be expressed as:

$$k = \frac{Ewt^3}{4l^3} \tag{1.4}$$

where k stands for the spring constant, E is the young's modulus of the material of the beam and w, t and l stand for the width, thickness, and length of the beam respectively [37].

According to the Hook's law, the resonant frequency can be calculated as follows:

$$f_0 = \frac{1}{2\pi}\sqrt{\frac{k}{M_{\mathrm{e}}}} \tag{1.5}$$

It is clear from equation 1.5 that variation of the mass or spring constant results in changes in the resonant frequency (Fig. 1.3).

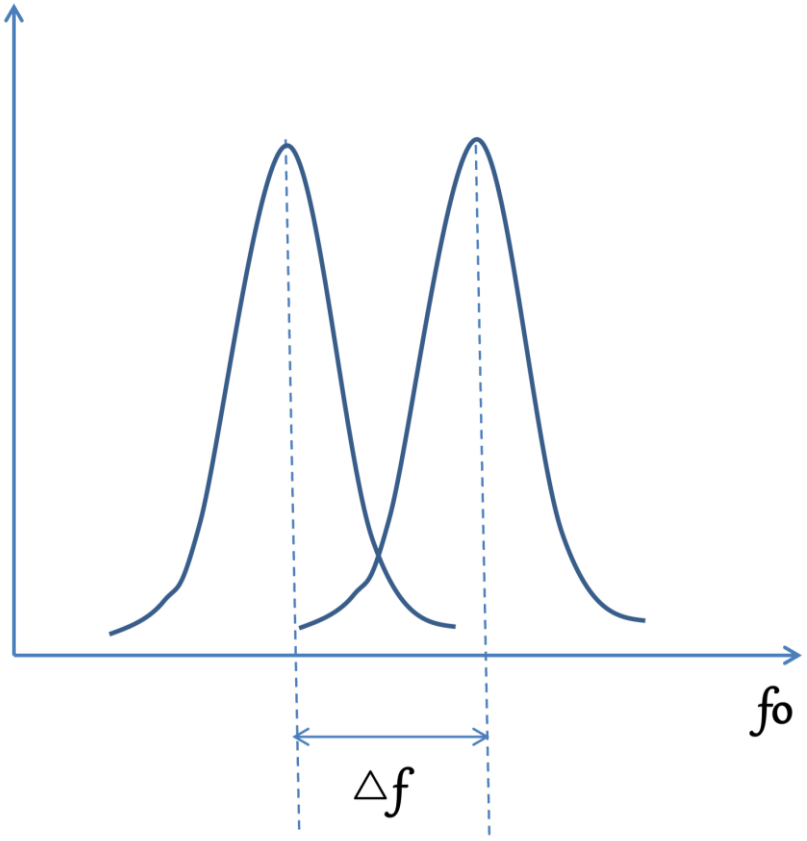

Fig. 1.3 Dynamic frequency change of resonant beam

In the case of biosensors, any adsorption or desorption onto or from the beam result in frequency shift. The addition or loss of mass changes the spring constant. Therefore, the change in frequency can be estimated by the following equation:

$$\Delta f = -\frac{1}{2}\frac{\Delta m}{M_e} f_0 \qquad (1.6)$$

1.3 Readout methods

1.3.1 Optical

1.3.1.1 Optical lever

The optical lever technique is a common transduction method for cantilevers which is used to measure deflection and frequency in AFM [55,56]. The principle of the optical lever technique for the monitoring of cantilever deflection is shown in Fig. 1.4. A laser beam is focused on the tip of the cantilever surface. The reflected laser beam is detected by a position sensitive detector (PSD). As the cantilever deforms, the reflection angle changes, and the reflected beam spot moves on the surface of PSD. Since the position of beam spot corresponds to the output electrical signal, by monitoring the output voltage of PSD, the position of light spot and thus the cantilever deflection can be calculated [52,53,57]. A resolution of 1 nm or better is achievable by this method [53]. This method can also be sued to measure the resonant frequency of a cantilever beam. The measureable frequency range is limited to hundreds of kilohertz however, due to the bandwidth of PSD. Furthermore, it is obvious that the medium around the cantilever affects the optical properties of the technique, which adds complexity to the subsequent data interpretation.

In most applications using the optical lever technique, only one cantilever is read at a time. Some more recent sensor platforms enable the simultaneous readout of multiple cantilevers for comparison. One such platform allows an array of eight cantilevers to be analyzed simultaneously using one laser. The PSD detects the reflected light from the eight cantilevers because of the narrow gap between the cantilevers [58–60]. A commercial version of this platform is currently available [61]. Alternatively, a wide laser beam can be used to illuminate all the cantilevers in the

array simultaneously while a large CCD camera detects the output from each individual cantilever [62–64]. Additionally, to obtain physical and chemical parameters along the full length of a cantilever rather than only on the free end, the bending profile of a cantilever can be captured by using a scanning laser along the beam [65].

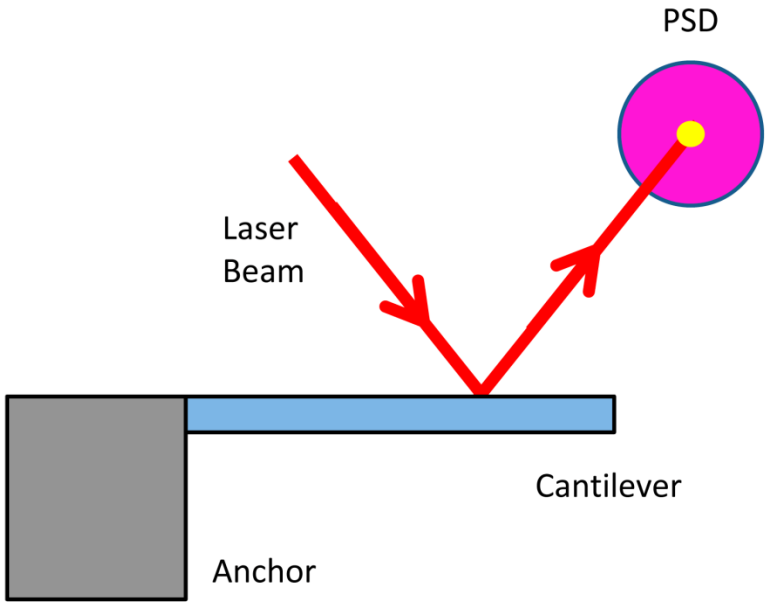

Fig. 1.4 Principle of optical lever for detection of cantilever deflection

1.3.1.2 Laser Doppler vibrometery

The operating principle of LDV is based on the Doppler effect and interferometry. As shown in the Fig. 1.7, a laser beam is first divided into two paths, the reference beam and the measurement beam, by beam splitter 1. The reference beam is directed to the photodetector by a mirror and beam splitter 3. The measurement beam is focused by a lens onto the beam surface from which it is

reflected. The oscillation of the beam causes a Doppler effect in the reflected wave. The Doppler frequency and phase of the measurement beam is then determined by the velocity and displacement of the oscillation of the beam as shown in Equation 1.7.

$$f_d = 2\frac{v(t)cos(\alpha)}{\lambda} \tag{1.7}$$

where f_d is the Doppler frequency, $v(t)$ stands for the velocity of the beam movement as a function of time, λ is the wavelength of the laser light and α stands for the angle between the measurement beam and the direction of beam movement. In the case of $\alpha = 0$, Eq.1.7 is simplified as Eq.1.8

$$f_d = 2\frac{v(t)}{\lambda} \tag{1.8}$$

To obtain the Doppler frequency, the reflected measurement beam is then directed by the beam splitter 2 towards the photo detector where it interferes with the reference beam. Subsequently, the coherent beam is detected by photodetector and the Doppler frequency is extracted. By analyzing the photodetector signal, the velocity and displacement of the beam are obtained.

To obtain the vibration direction, a Bragg cell can be added between the mirror and beam splitter 3 which acts as carrier frequency. The Doppler frequency is the modulation frequency. Demodulation of the signal process can be used to obtain the direction of beam movement.

This commercially available tool makes it possible to obtain substantially more information about the mechanical parameters of beam resonance. This tool is also bulky however, due to the complicated optical components required to make the measurements. Moreover, it works well for

large MEMS devices, but has limited resolution. Nanometer-scale NEMS beam, for example, produce very little or no signal.

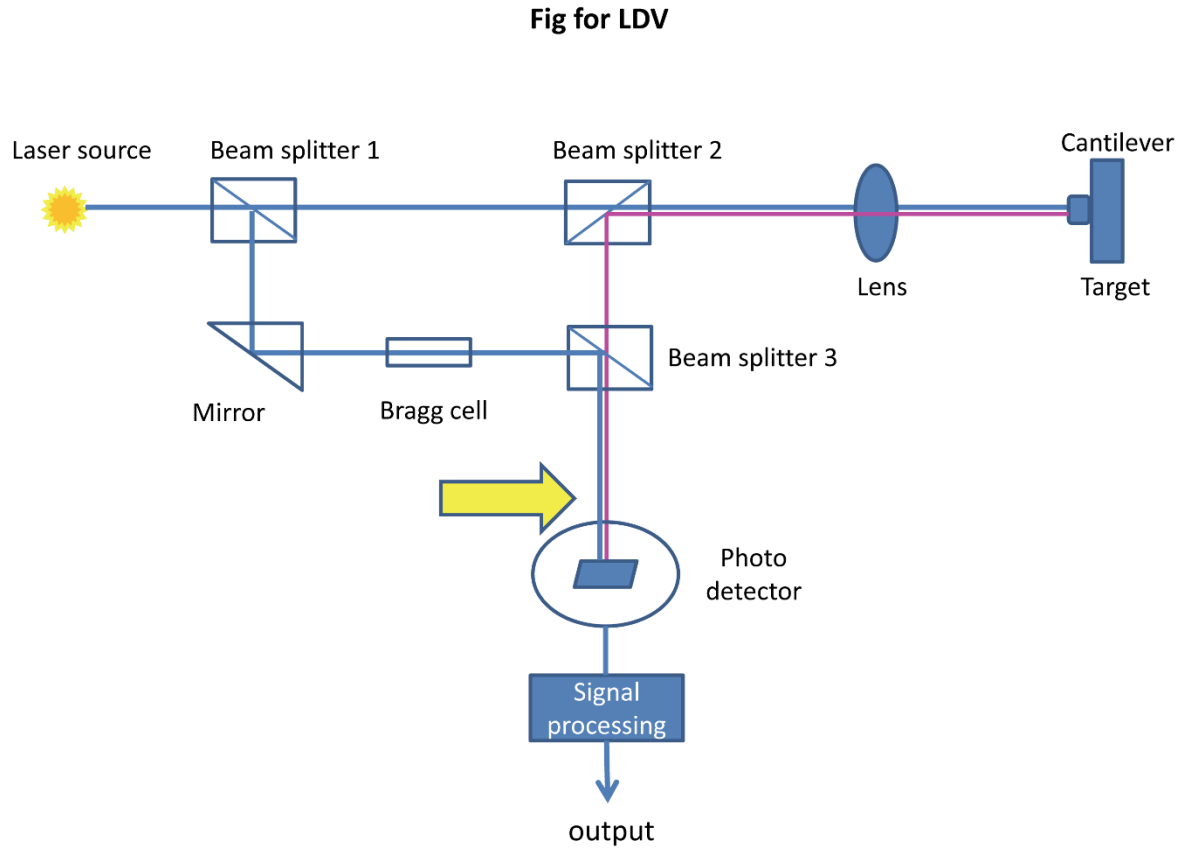

Fig. 1.5 Configuration of Laser Doppler vibrometer

1.3.1.3 Interferometry

Interferometry-based transduction methods are based on the interference effects [66–68] between an incident and a reflected beam of light. There are many methods and configurations used in

interferometry-based transduction methods. One robust method is the Fabry-Perot type interferometer [69] shown in Fig. 1.5. This type of interferometry provide resolution as high as 20 nm. The interferometric effect occurs due to the gap between beam and surface, and the resulting reflected signal is directed to the photodetector by beam splitter. The resonant frequency is determined using a spectrum analyzer. This method has been employed to measure the resonant frequency of NEMS beams throughout this work.

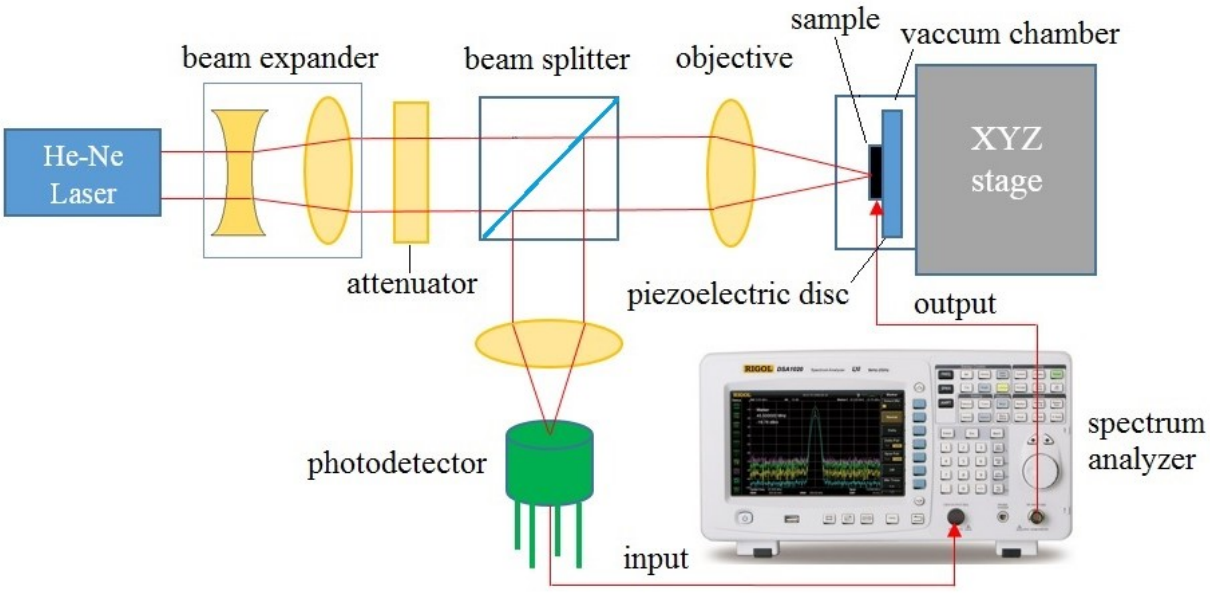

Fig. 1.6 Fabry-Perot type interferometer setup. From reference [70]

The principle schematic representation of the interference process is shown in Fig. 1.6. The suspended SiCN beam and the silicon substrate act as Fabry-Perot cavity. The gap Δd between the beam and the substrate introduces a phase difference of the two beams of reflected light thus inducing interferometric modulation of the signal. As the beam oscillates, the changing

gap distance Δd results in a time-varying phase difference between the two beams of reflected light. A moving fringe pattern is thus created which impinges on the photo-detector. The intensity of the light is then transduced into an electrical signal by the photo-detector which is sent to the spectrum analyzer. The time domain signal is then Fourier transformed into a frequency domain signal. The resonant frequency of the beam is the frequency where the peak electrical signal amplitude occurs [71]. This method is highly sensitive, but the measurement system is bulky and difficult to miniaturize.

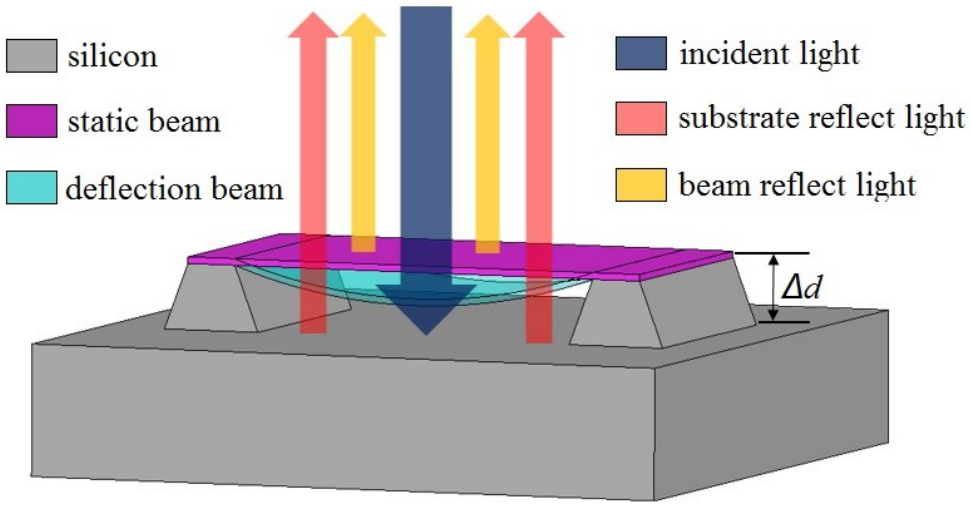

Fig. 1.7 Schematic view of the interference created by the optical path difference between the light reflected from the substrate and beam.

1.3.2 Electrical

1.3.2.1 Capacitance

A suspended beam can be approximated as a parallel plate capacitor when the substrate and the beam are both conducting materials. Deflection of the beam changes the height of the gap between

the substrate and the beam. This then induces a change in the capacitance. This method was initially used in AFM [72]. This read out method easily integrates with standard semiconductor technology and it has been demonstrated for NEMS sensor signal transduction [73,74]. The medium of the gap affects measured capacitance, something which needs to be considered in data interpretation. This method can lead to sensitivity on the order of picofarads. Therefore, non-uniformity in the fabrication process, such as high surface roughness of substrate and the suspended beam as well as the variations in initial gap, affect the value of capacitance measurement. When used in liquid medium, the faradaic current between the plates brings a disturbance factor to the value of the capacitance [52]. Therefore, this method it is not applicable in liquids. Similarly to the beam snap-down effect of parallel plate RF MEMS switches, when the displacement of beam exceeds 1/3 of the original gap, the beam is drawn down into contact with the substrate. Thus, this method also does not work for large displacements.

1.3.2.2 Tunneling

The tunneling read-out method was first used in AFM [75]. It was later applied to determine the deflection of beams in 1991 [76]. Presently, it is frequently used in Scanning Tunneling Microscopy (STM). The tunneling read-out method requires beams made from conductive materials or coated with a conductive layer. When a voltage is applied between the conducting beam and the electrode, the electrostatic force pulls the beam very close to the electrode. The electron tunneling effect occurs between this very small gap [75,77]. The tunneling current is calculated as Eq. 1.9

$$I \propto Ve^{-a\sqrt{\phi s}} \tag{1.9}$$

where V is the applied voltage, a is conversion factor, ϕ is the barrier height and s is the gap height [77,78]. It can be seen from Equation 1.9 that the tunneling current is extremely sensitive to the gap distance, in other words, the displacement of beam. Tunneling read-outs with a sensitivity as high as 10^{-4} nm have been reported [77]. This method has been used as a transduction method for dynamic mode nanostrings [79,80]. However, this method requires meticulous fabrication processes because of the high sensitivity of the tunneling current to the material between the electrodes and the required tiny gap between the beam to the electrode. For these reasons, this method is not widely used.

1.4 Fabrication of MEMS/NEMS beam

The fabrication process of MEMS and NEMS beams was developed from the fabrication techniques used for traditional semiconductors. It includes thin film deposition, lithography patterning and etching processes. The differences between MEMS device and semiconductor fabrication processes are obvious. There are usually several layers in semiconductor devices, especially transistors, to form the drain, source, and gate regions. A critical factor determining the success of fabrication is the alignment of lithography. Misalignment of different layers commonly leads to failure of the device. For example, misaligned contact vias cannot interconnect metals between the two layers. Therefore, the complexity of semiconductor device fabrication mainly depends on the number of layers. This is not the same case for MEMS device, however, which usually does not involve as many layers as semiconductors.

The purpose of a MEMS device is to either create mechanical movement based on an input signal or convert mechanical movement into a readable output. To obtain movable structures, usually hollow structures are created. Micro- and nanobeams are commonly fabricated by creating the

cantilever or bridge structures and etching away the layer underneath. This layer is often referred to as a sacrificial layer. There are multiple methods that can be used to etch away the sacrificial layer. Selection of the most appropriate method for a given application is largely based the chemistry selectivity between types of materials in the device. For the process to be successful, the sacrificial layer must be etched away while the device layer remains intact. Depending on the properties of the sacrificial layer, these methods may be categorized as bulk micromachining or surface micromachining. In bulk micromachining, the substrate itself, usually silicon, works as sacrificial material. In surface micromachining, sacrificial layer is purposely deposited before the device layer and is etched away. In either case, the yield of the MEMS fabrication mainly depends on whether the beam is successfully released or not.

1.4.1 Bulk micromachining

Bulk micromachining has been developed and widely used because of the simplicity of process compared to that of surface micromachining. The bulk material is removed by an etchant either from the top side or backside of the wafer. These simplified fabrication processes are illustrated in Fig. 1.8. As seen in the topside etching process, the device layer is defined by lithography and works as etch mask. The exposed surface of the bulk material is an etching window for the etchant. The suspended structure is formed by the undercut of bulk etching process. The undercut can be achieved either by anisotropic or isotropic etching. A typical isotropic wet etchant for silicon is composed of a mixture of hydrofluoric acid, nitric acid, and acetic acid (HNA). HNA does not etch silicon dioxide or silicon nitride so they can work as etch masking layer. Another way to isotopically etch silicon is by using plasma composed of SF_6 and O_2 gasses. A frequently used silicon wet etchant is aqueous KOH. The etch process is anisotropic, and forms an undercut angle

of 54.7^0. By controlling etching rate and time, the length of hanging structures can be precisely controlled.

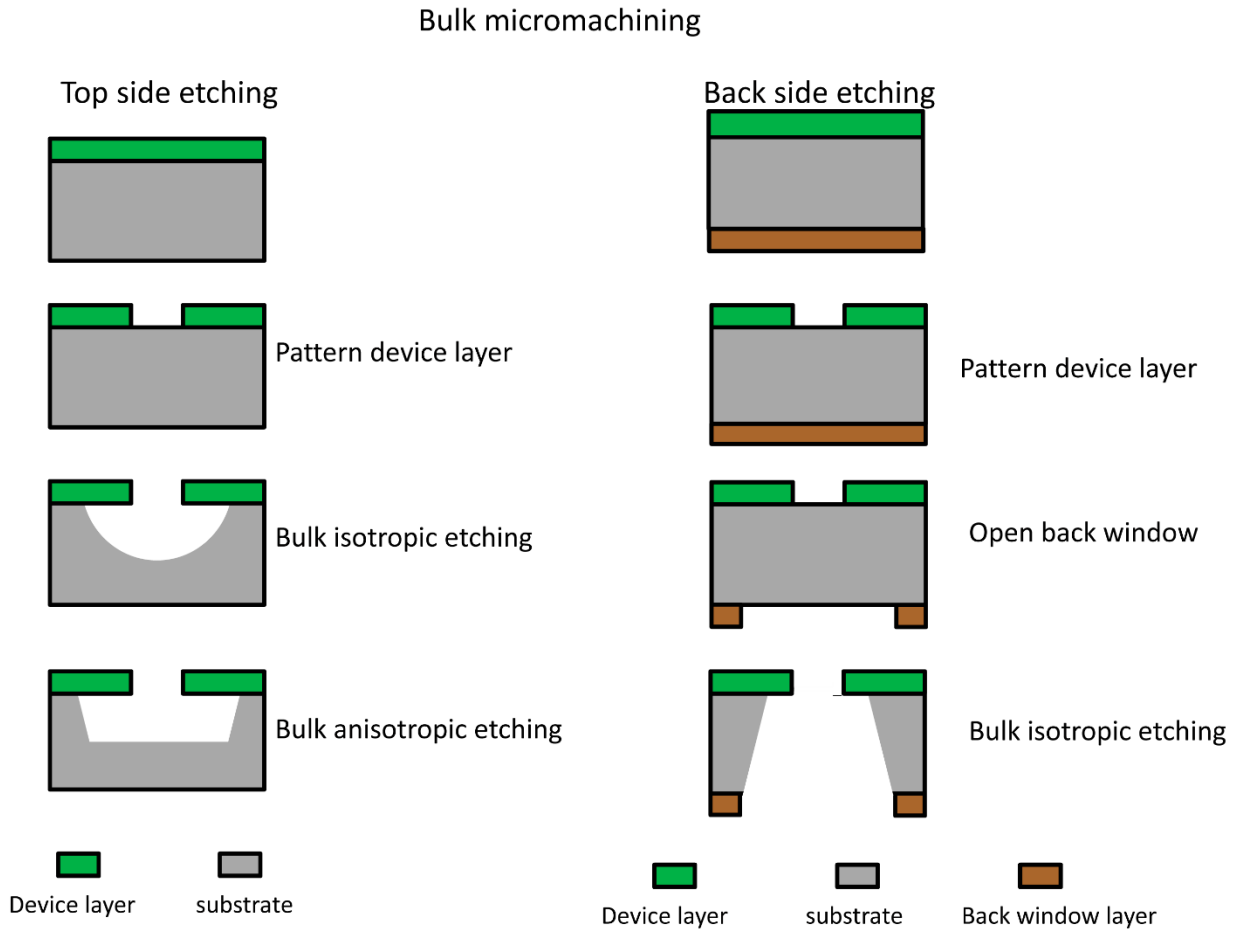

Fig. 1.8 Simplified bulk micromachining process for beam fabrication

A frequent issue associated with MEMS beam release is the stiction effect. When the sacrificial layer is removed by wet etchant, the beam is attracted onto the substrate by capillary force. There is increased probability for stiction to happen when the gap between the suspended structure and the substrate is small. In order to prevent stiction, critical point drying (CPD) is often used immediately after the sacrificial release step. The basic principle is that at the critical point, gas phase and liquid phase are most indistinguishable. The critical point of CO_2 has relative low pressure and temperature compared to that of water. Therefore, when a MEMS device is loaded in the CPD chamber, liquid CO_2 replaces the water between the beam and substrate/ and transforms into gas phase at the critical point. This liquid-phase transition does not cause any capillary force so stiction is avoided. The drawback of this method is the possibility of contamination from the CPD chamber being deposited onto the surface of the MEMS.

The most widely used bulk micromachining method for MEMS beam fabrication is backside anisotropic etching. A window layer is deposited on the backside of the substrate as an etching mask. Traditionally, the bulk material consists of silicon and the backside window protection layer is made of silicon dioxide since an aqueous KOH solution etches silicon quickly but etches dioxide slowly. The device layer and the backside window layer are patterned by two individual lithography steps. The device layer patterning is relatively straightforward. However, the size of the backside window is calculated based on the angle of the anisotropic etching undercut, the required beam length and the thickness of the wafer. The wet etchant etches through the whole wafer to release the beam. Obviously, the etching time is long. In some cases, the backside protection layer does not need to be removed because it is used for addressing and connecting with electronic devices in the same wafer.

1.4.2 Surface micromachining

In surface micromachining, a sacrificial layer is purposely deposited onto the wafer prior to the deposition of device layer. As shown in Fig. 1.9, the device layer is patterned by lithography to create the desired geometry so that the underlying sacrificial layer becomes exposed. Isotropic etching of the sacrificial layer leads to a suspended beam. It is noticeable that in the case of very small lateral dimension, etching holes or channels need to be created in the device layer to allow access of the etchant to the sacrificial material and removal of the chemical products. Ideally, the etchant only reacts with the sacrificial material and leaves the device layer and substrate intact. A widely used example of such a sacrificial release process is based on SOI. After patterning the device layer on top of the silicon, the buffered oxide etch (BOE) removes the buried oxide layer and releases the silicon beam because of the high etch selectivity of the BOE for silicon dioxide over silicon.

Compared to bulk micromachining, surface micromachining is more flexible. There is a large range of sacrificial materials to choose from for different types of device materials. The physical and chemical properties of sacrificial materials can be customized to facilitate the successful release of the beams. Tuning the chemistry of the sacrificial layer can increase the etch selectivity of the substrate compared to the beam. The thickness of the sacrificial layer, i.e. the gap between the substrate and beam, affects the physical properties of the MEMS device.

However, stiction effects happen more frequently in surface micromachining than bulk micromachining. This is prominent when the sacrificial layer is rather thin. In this case, CPD needs to be used right after the sacrificial layer etch release process in order to prevent the failure of the

beam. Another method to avoid stiction is to adjust the beam stress so that the beam does not bend much after release.

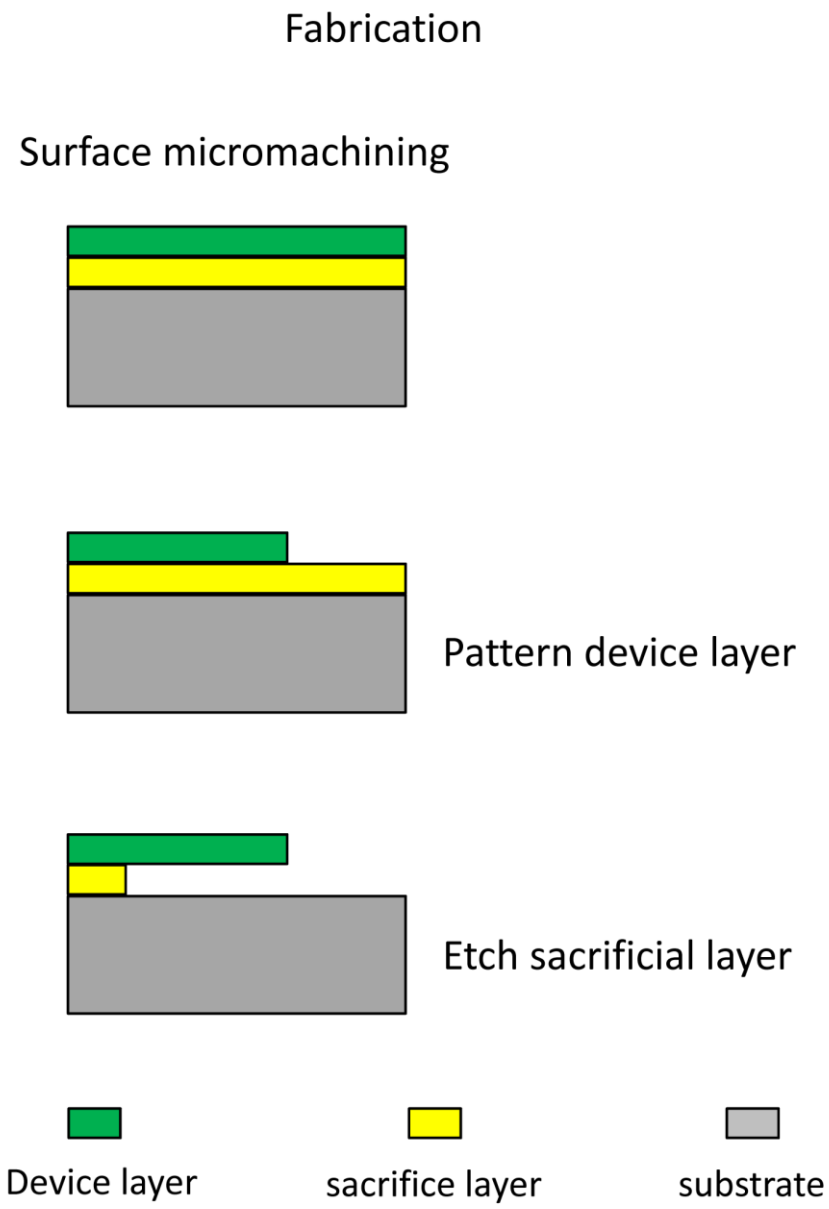

Fig. 1.9 Simplified surface micromachining process of beam

1.5 Future trends

For biological detection, the ultimate goal is single molecule detection. First, it is important for the biosensors to detect target analytes in extraordinary low concentration for reliable biological analysis and medical diagnosis. Due to the limitation of detection, bio-detection methods sometimes provide inaccurate or inconclusive results. Extremely sensitive biosensors are expected to make a large impact on clinical assays and drug discovery [81,82]. NEMS string-based biosensors have impressive sensitivity and have the potential capability of single molecule detection. Based on that, a concept for NEMS mass spectroscopy (MS) has been proposed [83]. This novel type of NEMS MS is expected to be advantageous over traditional MS because the NEMS MS is capable of capturing neutral molecules and particles without the requirement of ionization and pre-separation. The structure of molecules therefore remains unaltered [83]. Another strength of the NEMS MS is the relatively small consumption of sample analytes. Once the analytes are absorbed onto the NEMS, the mechanical response is induced. However, in a traditional MS system, as many as 108 molecules are involved in the measurement [84].

According to previous theoretical calculations, a detection sensitivity as low as 1 Da is achievable by NEMS biosensors [47,83,84]. Experimental efforts to reduce the detection sensitivity have been carried out over the past decade. In 2003, relatively large commercially available beams were milled into smaller strings using FIB. The small strings have been reported to detect femtogram level changes in mass [85]. More recent experiments have demonstrated high resolution mass sensing at 1000 Da and 200 Da levels respectively [44,86,87]. In 2009, based on the statistical analysis of hundreds of mass adsorption events on NEMS string, single molecule based NEMS

MS was demonstrated [83]. In 2012, further improvement of multimode analysis was used to decouple the role of absorption location on mass sensing. As a result, real time single molecule detection based NEMS MS was demonstrated [84].

As discussed previously, the mass sensitivity of a NEMS string is related to the mass of string itself. Resolving a signal induced by a single molecule requires the mass of the NEMS string to be comparable to the mass of the molecule. Considering the intrinsic noise floor of NEMS sensors, the mass induced frequency shifts are expected to be as large as possible relative to a same amount of mass loaded. Therefore, to increase the probability of the extreme small mass detection of single molecule, it is essential to improve the fabrication skills for strings with ultra-small mass. The huge beam milled into smaller size by FIB used in reference [85] is an example.

As same as other label-free detection methods, surface modification layer is needed for specific detection. To increase the probability and reliability of analytes absorption onto the NEMS strings, the surface need to be uniformly bio-activated. Otherwise, analytes only bond to part of the surface which leads to non-uniform coverage of the bonding sites. This reduces the chance of molecules to be immobilized on the NEMS string and reduces the reliability of the sensor. Hence, improvement of surface modification for uniform and stable bonding site coverage is imperative for single molecule detection.

1.6 Research scope & thesis structure

This thesis involves the fabrication, functionalization and measurement of the nanomechanical string resonator based biosensors. The aim of this work was to increase the detection sensitivity and stability of NEMS string biosensors, as shown in the flow block diagram of Fig. 1.10.

The physical transducer determines the sensitivity of the mass-sensitive sensors. To be specific, a string with reduced mass enhances the sensitivity. For this purpose, two strategies to lower the string mass are carried out. A traditional method is to simply minimize the string. Lithographic technique is the primary limiting factor in the fabrication of ultra-small scale devices. Materials with appropriate mechanical properties able to withstand the nanomachining process are also critical to successful fabrication. Therefore, both lithographic and materials aspects were studied. A novel method to reduce the string mass is to fabricate nanopores through the string. More specifically, a FIB technique was used to mill the nanopores into the nanostrings. A comprehensive study of the nanofabrication of the regular nanostrings and nanowires is described in chapter 2. The fabrication of the porous nanostrings is described in Chapter 3.

The bio-interfacial layer is an important component in the stability and reliability of the biosensing system. A common surface modification method, diazonium salt reduction induced aryl film grafting, is employed and for the first time applied to nanostrings for bio-functionalization. This diazonium chemistry is reported to form strong and stable chemical bonds with substrate. The diazonium chemistry was tested on bare silicon carbonitride surfaces to determine if the diazonium chemistry would be applicable to the nanostring material. A rabbit IgG sandwich assay, in which anti-rabbit IgG as recognition molecule, rabbit IgG as target molecule and labelled anti- rabbit IgG as detection molecule, was performedto validate the effectiveness of the bio-functionalization. These experiments and their results are discussed in chapter 4. After successfully implementing the diazonium chemistry, biological detection was successfully performed using the nanostrings and the diazonium chemistry. These experiments are discussed in chapter 5.

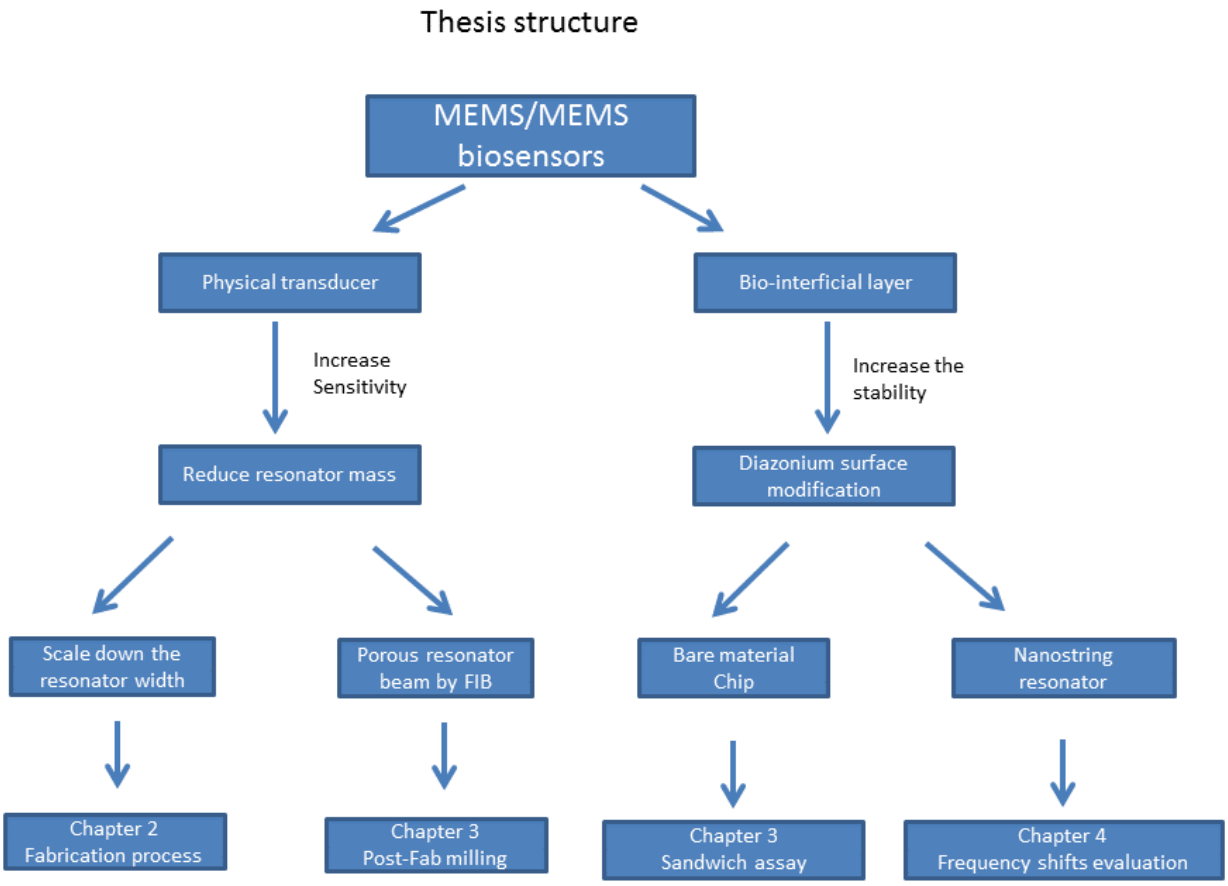

Fig. 1.10 Thesis structure

Chapter 2 Fabrication of nanostrings and nanowires

2.1 Introduction

2.1.1 Nanometer-wide beam devices

A trend toward miniaturization occurs during the development almost all types of electronic devices. This tendency has been accelerated during the past decades to implement the ultimate in small device dimensions. From device fabrication perspective, shrinking the unit size is necessary to increase integration on a single wafer. Electronic device and system is fabricated in a relatively smaller area within a wafer and thus the manufacturing cost is reduced. From the point of view of consumer electronics, portability—having the smallest possible handle size and weight—is one of the driving forces of the market. MEMS sensors, such as accelerometers, are widely used in consumer electronics such as iPad and Apple Watch. As with any type of electronic devices, the size of MEMS devices needs to be pushed to the ultimate lower limit to meet the needs of integration, portability, and reduced cost.

To increase the detection sensitivity of a mechanical-beam-based resonator biosensor device, a beam of small dimensions—and therefore low mass—is required to induce a relatively large response signal. Devices with small sizes also make large array integration possible, enabling detection of multiple targets within a single chip. The detection sensitivity of a beam is determined by its mass. To obtain a resolvable signal, the mass of the beam needs to be comparable to the

mass of the target. The ultimate goal with respect to detection sensitivities is single-molecule detection. In this case, it is therefore a pre-requisite to shrink the size of beam down to deep nanoscale. Depending on the width of the nanobeams, they are categorized as nanostrings and nanowires.

In terms of the technical implementation of such suspended nanostrings and nanowires, there exist several nanofabrication bottlenecks. The first technical difficulty is lithographic patterning. The most commonly used UV contact photolithography is limited to ~500 nmresolution. Alternative lithography methods are able to resolve feature sizes less than 100 nm and pattern NEMS devices on the scale of tens to hundreds of nanometers. In the extreme case, nanowires with widths less than 10 nm present a significant challenge for lithography. Furthermore, fabricating a 10-nm-wide suspended nanowire involves many more difficulties than patterning a 10 nm line in solid-state transistors. To make such a suspended nanowire, the underlying material is etched away to release the nanowire. After this etch release process, the nanowire may break due to the stress of the material. Thus, the selection of a proper material for the nanowire is critical for the success of the fabrication. This aim of this chapter is to solve these lithography and material problems to achieve the ultra-small nanostrings and nanowires.

2.1.2 Lithography

As predicted by Moore's law, the semiconductor device size has been reducing by half every two years, and the transistor integration on a single wafer has been increasing at an exponential rate over the past decades. Up to date, the resolution of commercial semiconductor transistors has been shrunk down to 14nm line by Intel. The demands from the semiconductor industry have been

pushing the development of lithography techniques. The evolution of MEMS towards NEMS directly benefits from the advancement and maturation of lithography tools.

Traditionally, UV lithography is the most widely used technique because of its ability of batch fabrication, simple configuration, fast speed, relatively high yield, low maintenance and unit cost of each wafer. The resolution limit of lithography is determined by the wavelength of the light as shown in Equation 2.1

$$W_{min} = K\frac{\lambda}{NA} \tag{2.1}$$

Here W_{min} is the minimum feature resolution, λ is the wavelength and NA is the numerical aperture. As seen from Equation 2.1, the most effective way to reduce the feature resolution of lithography patterning is to either reduce the wavelength of the light source or increase the numerical aperture. Based on the theory, a variety of advanced lithography methods, such as DUV (deep ultraviolet), EUV (extreme ultraviolet), laser lithography, x-ray lithography, EBL (electron beam lithography), and IBL (ion beam lithography), have been developed.

Besides the above mentioned mainstream lithography tools, other categories of lithography methods exist. Instead of decreasing the wavelength of the light source, liquid immersion lithography increases the numerical aperture. By introducing a liquid as a medium between the lens and wafer, the refractive index increases as well as the numerical aperture. Immersion lithography is often used in combination with DUV. Other lithography methods, such as soft lithography and nano imprint lithography (NIL), offer good alternative to EBL. But these processes involve steps to create the template first and then use the template to pattern the target material layer, which is rather complicated.

2.1.3 Electron beam lithography

In terms of high resolution patterning of nano structures, especially less than 10 nm, EBL is the most mature and accurate lithography tool compared to other methods.

The first generation of EBL was developed more than 40 years ago [88,89] from an alteration of a traditional SEM. The electron beam is controlled by the beam blanker and pattern generator to spot on the target area on the sample surface, which is coated with resist. Similar to the chemical responsive property of photoresist to UV light in traditional photolithography, the molecular structure of this chemical compound changes due to exposure to the rastering electron beam. As a result, the solubility of the exposed area in the chemical developer changes while unexposed areas of the resist remains the same. Therefore, the surface resist is selectively removed and kept in the following development step. Due to the extremely tiny wavelength of the electron beam, the patterned feature size is readily made as small as a few nanometers. Since the designed pattern is transferred to resist by electron beam writing, this process does not require a physical mask. Compared to the commercial available tool for nanoscale patterning, like EUV, EBL is rather slow process and not suitable for batch fabrication. However, the cost of EBL tool is significantly cheaper than EUV tool. Therefore, EBL is advantageous and widely used in research labs.

The original application of EBL was to make photomasks not direct lithography on device surface [90]. The reason is mainly due to the slow writing speed of the electron beam. The extended exposure time is not suitable for batch fabrication for industry application. Although EBL excels due to its advantages like controllability, flexibility, precision in deep nanometer scale and mask-free nature, it has been limited to mask-making and research labs for two decades. Numerous efforts have been made to improve the electron beam-control system to improve the productivity

of EBL. Until recently, multi-beam writers have been developed by industry and to allow high throughput for commercial applications [91–93].

2.1.4 SiCN material for nano-resonators

The most problematic and challenging part of fabrication of NEMS/MEMS resonator beams usually lie in the etch-release step. The selection of an optimal material is critical to prevent the nanowire from breaking when etch-released. A variety of materials, Si, SiN, AlN and TiN, have been explored to fabricate NEMS. But most of them are not suitable for the fabrication of ultra-narrow nanowires.

Single crystal silicon is the most simple and easily available material. Silicon resonators with width from micrometer down to nanometer have been successfully fabricated [94,95]. However, there are significant drawbacks of the fabrication of silicon resonators. First, silicon is a brittle material by nature. As the silicon nanowires narrow down to deep nanometer, the chance for the string to break during etch-release process increases. Especially when the lengths of the nanowires are more than a few micrometers, the yield is as low as almost zero [96]. Second, the fabrication of silicon resonators is limited to SOI wafer. The silicon beam is released by isotropic etching of buried oxide layer. If the oxide layer is thick, the isotropic etching leads to a big undercut in the anchoring pad. The over-hanging of silicon resonators causes energy loss and reduce the Q factor. To avoid this issue, the oxide layer need to be thin. In etch-release process, the small gap between resonator beam and substrate easily causes stiction effect. Therefore, CPD is necessary to prevent stiction and mechanical failure of the device. But CPD introduces contaminations to the silicon surface. which is adverse to the subsequent surface modification.

Other crystalline materials, like SiN, AlN, are not good candidate for NEMS resonator beam either. In fact, both single and poly crystalline materials are not resilient to defects and tends to crack along grain boundaries during the etch-release process. Therefore, the selection scope is limited to glassy amorphous materials that are resilient to defects and do not break easily during etch-release. For instance, glassy TiN and SiCN based nano-resonators have been fabricated [96,97].

Another issue with the etch-release process is the mismatch of stress between the device film and the underlying sacrificial layer/substrate. When the substrate is etched away and the film is released, a high compressive film tends to break whereas a low tensile stress film tends to stay suspended. Therefore, a glassy film exhibiting low tensile stress is preferred.

Glassy SiCN material has been studied extensively by Evoy and his coworkers [31,42,96,98,99]. Previous studies show that SiCN thin film is highly compressive as deposited because of the bonded hydrogen in the film. A subsequent annealing process is able to effectively drive away the bonded hydrogen from SiCN film and thus change the film stress from compressive to tensile. By adjusting the annealing parameters, time and temperature, the stress of the annealed film is tunable over a broad range from low compressive to almost zero stress, low tensile stress and even very high tensile stress. This tunability is a highly useful feature for fabrication of nanostring and nanowire.

2.1.5 Structure of this chapter

The structure of this chapter is divided into three sections. The first part is the description of SiCN film deposition and annealing. This includes the SiCN film deposition, elemental and stress characterization and thermal annealing method. The second part describes the EBL resists used for the fabrication of nanostrings and nanowires. The commonly used EBL resist PMMA and the high

resolution resist HSQ were employed as part of this work. The properties and mechanisms of these two resists are introduced. The third part is the description of fabrication process. SOI based nanostrings, SiCN nanostrings and nanowires, were fabricated. Complete process flow and fabrication method are given. The final part is the SEM and HIM inspection of these nanostring and nanowire arrays the dimensions of which are measured.

2.2 Experiment

2.2.1 SiCN film

2.2.1.1 SiCN film deposition

A single-crystal (100) silicon wafer was subjected to a routine 15 min piranha clean (3:1 96% H_2SO_4: 30% H_2O_2) to eliminate surface organics. For ultra-thin film deposition, piranha clean is essential to make the surface of silicon free of contamination and the deposited film continuous and uniform across the whole wafer. After piranha clean, the wafer was thoroughly rinsed in water.

Usually, a thin layer of native oxide exists on top of the silicon wafer. In addition, the piranha clean possibly causes oxidation on the silicon surface. It is crucial to remove this native oxide layer to ensure the successful final step of bulk silicon etching and release of SiCN nanostring and nanowire. If the silicon surface is covered by the native oxide layer, depending on the etch selectivity of the chemical etchant to silicon over dioxide, the etchant is either prevented from contacting the underlying silicon or etch the dioxide away before contacting the silicon surface. As a result, the silicon fails to be etched or etches in an unpredictable slow rate with possible contamination from oxide etch. For this reason, after the piranha clean, the silicon wafer is

immediately transferred to a buffered oxide etch (BOE, 10:1 HF: NH_4F) solution to strip the native oxide. After 3 min, the silicon wafer is water rinsed and nitrogen blow dried.

The SiCN film was deposited onto the clean silicon wafer by plasma enhanced chemical vapor deposition (PECVD). First, the Trion Orion PECVD chamber was pre-conditioned at a mixed gases flow of 25 sccm DES, 40 sccm NH_3, 55 sccm N_2 at a temperature of 300 ^{0}C, a pressure of 500 mTorr, and a power of 50 W for 1200 s. Then the silicon wafer was loaded into the reactor. The chamber was purged by 55 sccm N_2 under pressure of 500 mTorr and a temperature of 300 ^{0}C for 10 s. The chamber was prepared for the deposition by a mixed gases flow of 25 sccm DES, 40 sccm NH_3, 55 sccm N_2 at a temperature of 300 ^{0}C, a pressure of 500 mTorr for 10 s. The SiCN thin film was deposited with at a mixed gases flow of 25 sccm DES, 40 sccm NH_3, 55 sccm N_2 at a temperature of 300 ^{0}C, a pressure of 500 mTorr, and a power of 50 W. Different deposition times from 100 s to 1200 s are used for different film thicknesses on nine silicon wafers.

The thickness and uniformity of the deposited SiCN film is characterized by a Filmetrics F50 reflectometer thickness mapping system (Filmetrics, San Diego, CA, USA) over 13 points on the wafer. The stress of the as-deposited SiCN film is measured by a Flexus 2320 wafer stress measurement system (KLA Tencor, Milpitas, CA, USA). Table 2.1 shows the thickness parameters and the stress of the SiCN film for different deposition times.

For the purpose of small mass nanostrings and nanowires, films as thin as possible are preferred. But according to past experience in our lab, 50 nm SiCN is the thinnest film that can stand the KOH etching at the final Si etch step. Films less than 50 nm thick are easy to break in a KOH bath. In contrast to LPCVD deposited SiN film, which has a rather dense and chemically stable structure, PECVD SiCN has a slow etch rate in a KOH bath. Considering this trade-off, SiCN films roughly

around 52 nm thick, rather than 42nm, is selected for the nanostring and nanowire processing. As seen from Table 2.1, the uniformity and standard deviation of 52 nm thick SiCN films are within good tolerance.

Table 2.1 Parameters of PECVD deposited SiCN film

Silicon wafer	Deposition time (sec)	Thickness (nm)	Uniformity (+/- %)	Stand. Dev (nm)	Stress (Mpa)
1	100	41.95	2.7	0.72	-968.3
2	125	52.85	5.6	1.76	-775
3	125	52.03	7.2	1.98	-764
4	125	54.5	3.3	1.44	-779
5	125	53.98	5.3	1.61	-760
6	140	60.1	3.4	1.34	-840
7	250	106.1	4.6	2.96	-940.1
8	370	156.8	3.3	3.55	-920.6
9	1200	660nm	N/A	N/A	N/A

2.2.1.2 SiCN film element characterization

Surface XPS analyses were performed to characterize the elemental composition of the deposited film, namely the ratio of silicon, carbon and nitride. The XPS was performed in a Kratos Axis Ultra spectrometer using a monochromatic Al Kα source (hν=1486.6 eV). Instrument base pressure was lower than 5 x 10^{-8} Pa. The survey scans were acquired with a pass energy of 160 eV.

2.2.1.3 SiCN film stress tuning

Table 2.2 Parameters of PECVD deposited SiCN film

Wafer #	Original stress (MPa)	Anneal tool	Anneal temp. (^{0}C)	Anneal time (hr)	Stress after annealing (MPa)
4	-779	Flexus 2320	450	2	-400
5	-760		500	2	-271
2	-775	MiniBrute Furnace	500	2	-1.6
3	-764		525	2	169

Silicon wafers # 4 and # 5 were respectively annealed in the heater plate of the Flexus 2320 wafer stress measurement system with stress monitoring. As shown in Table 2.2, annealing at 450 ^{0}C for

2 h takes the film from a high compressive stress to mid-range compressive stress. A temperature increase to 500 ^{0}C for 2 h effectively reduces the film stress to a low compressive range. However, due to the maximum limitation of 500 ^{0}C of the heater plate of Flexus 2320, higher temperatures cannot be experimented with. The same thermal condition of 500 ^{0}C for 2 h was applied in a MiniBrute 3 zone tube furnace (Thermco, Lafayette, NJ, USA). But the annealed wafer film exhibited almost zero stress. The difference of the two annealed stresses from the two tools is liekly related to chamber conditions of the MiniBrute Furnace and Flexus. In the Flexus, the heater is only applied to the bottom of the wafer and the temperature is not uniform in the chamber whereas the temperature in the MiniBrute Furnace is stable and uniform. A further temperature increase to 525 ^{0}C for 2 h annealed the film to a low tensile stress of 169 MPa, which fits the requirement for nanostring fabrication. Hence, wafer #3 was used for further processing and diced into 0.7 cm × 0.7 cm square samples for the handling of EBL.

2.2.2 EBL photoresist

There are more than two dozen resists used for electron beam lithography [100–102]. Similar to the case of photoresists, which are sensitive to UV light, the electron resists are physically and chemically sensitive and responsive to the electron beam. Depending on the different behaviors due to exposure to the electron beam, the electron resists are divided into positive and negative resists. The bond in a positive electron resist breaks and produces short-chain products which are easily dissolvable in specific solutions. In contrast, the short chains of a negative electron resist bond into long chains and become harder to dissolve in solutions. In order to select proper resists from the many types of electron resists to pattern nanostring and nanowire based resonators, the resists should meet the following criteria: simple developer chemistry, high resolution and sensitivity, physical and chemical stability, strong adhesion to the surface of silicon and SiCN, and

easy to be stripped off from the sample surface after development. To meet these requirements, PMMA and HSQ have been chosen for this work. PMMA is the most widely used positive electron resist for its stable performance in terms of sensitivity and resolution. In this chapter PMMA is used to pattern nanostrings. Although recent reports show the patterning of sub-20 nm and even sub-10 nm lines by using PMMA, HSQ is commonly regarded superior to other types of electron resists in the case of patterning extremely high resolution ultra-small features. HSQ is a less frequently used resist because of the physio-chemical instability, the relatively complicated storage and handling procedure and expensive cost. Hence, HSQ is not chosen to pattern relatively wide beams.

2.2.2.1 PMMA

PMMA is short for polymethyl methacrylate, also known as acrylic. The molecular structure of PMMA is shown in Fig. 2.1 [94]. Depending on the length of the polymer chain, PMMA products for EBL purposes are named under their molecular weights, which vary from 50,000 to 2.2 million. The bigger the molecular weight, the higher the develop contrast and resolution after lithography. PMMA 950 and PMMA 495 are the common commercially available products. PMMA A means that the PMMA polymer is formulated in anisole solvent. PMMA A2 means the concentration of PMMA in anisole is 2%. The concentration of PMMA in solvent determines the thickness of the resist after spin coating. Resists with smaller thickness tend to have a higher resolution due to the reduced scattering effect of the electron beam. Therefore, PMMA 950 A2 is selected for EBL.

The mechanism of chain scission of PMMA upon exposure to the electron beam is shown in Fig. 2.2 [94,103]. There are two ways to degrade a PMMA long chain, either by removing the ester

group or by direct bond breakage of the chain. The reaction products are short chains of the original unexposed unit.

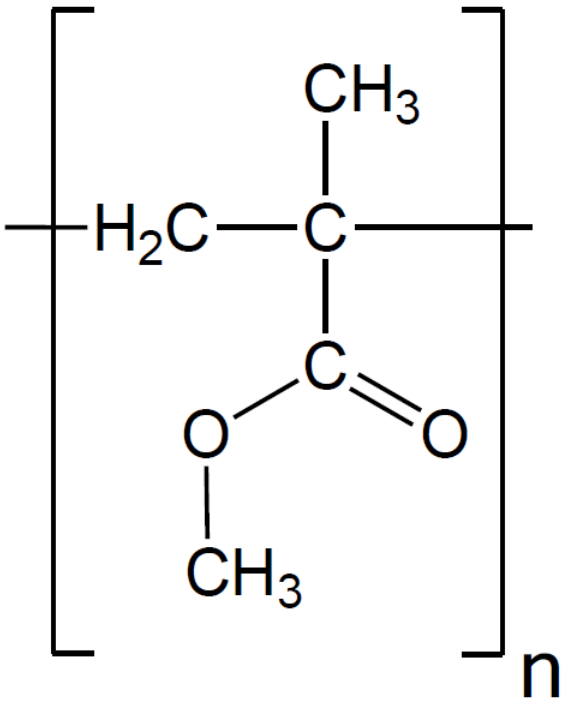

Fig. 2.1 The molecular structure of PMMA. Copyright © Mohammad Ali Mohammad's PhD thesis [94]. Reprinted with permission.

There are multiple choices of developer chemistry for PMMA. The Methyl isobutyl ketone (MIBK) has good sensitivity but comes with a swelling issue [104,105]. Isopropyl alcohol (IPA), in contrast, has low sensitivity but does not have much swelling issue [104,106,107]. Therefore, mixtures of MIBK and IPA as developer solutions have a balanced result. Different combination ratios have been investigated [104,107–109], MIBK:IPA 1:3 (v/v) is most commonly used for high resolution lithography [110]. In the following sections, PMMA is chosen to pattern both SOI and SiCN nanostring resonators.

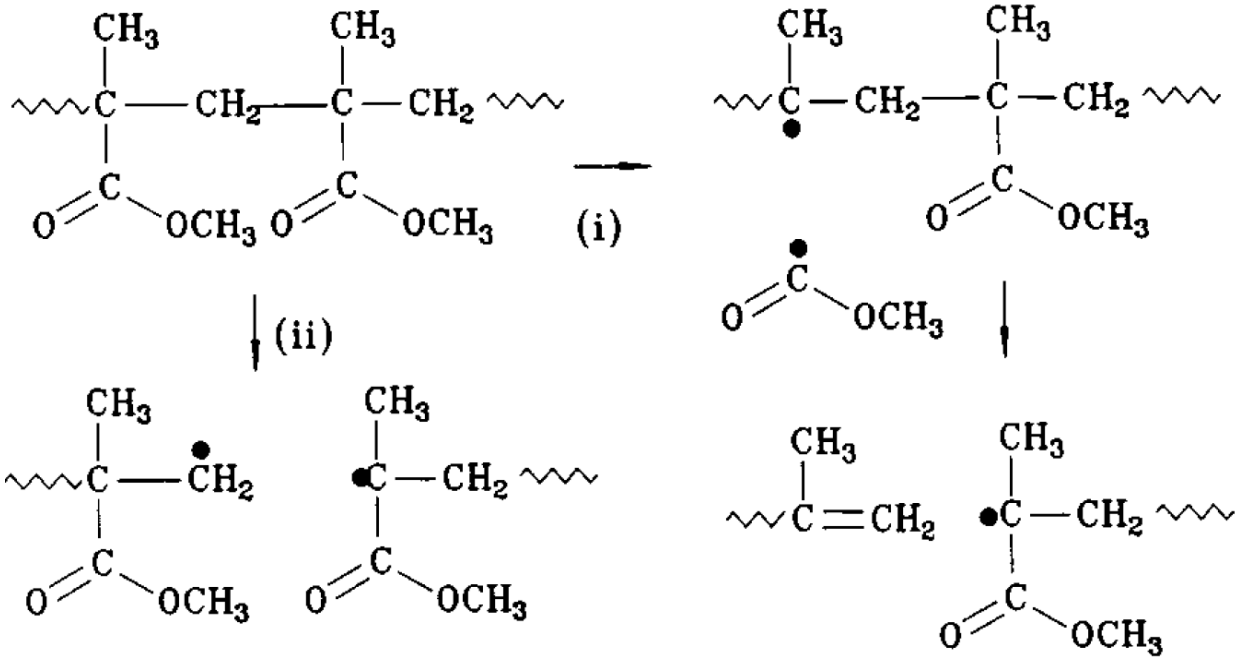

Fig. 2.2 The chemical mechanism of main chain scission of PMMA decomposition by electron exposure. (i) removal of the ester group, leading to a terminal =CH2; (ii) a direct process. The radical intermediates can undergo further reaction or decomposition (not shown). Reprinted with permission from [103]. Copyright © 1999, American Vacuum Society.

2.2.2.2 HSQ

HSQ is an electron resist known for its extremely high resolution. The molecular structure of HSQ is shown in Fig. 2.3 [94]. Different from PMMA, which is composed of polymer chain, the HSQ molecule is structured as a cubic cluster. In the cage unit, each silicon at the vertices is bonded to three oxygen; each oxygen at the edge is bonded to two silicon atoms.

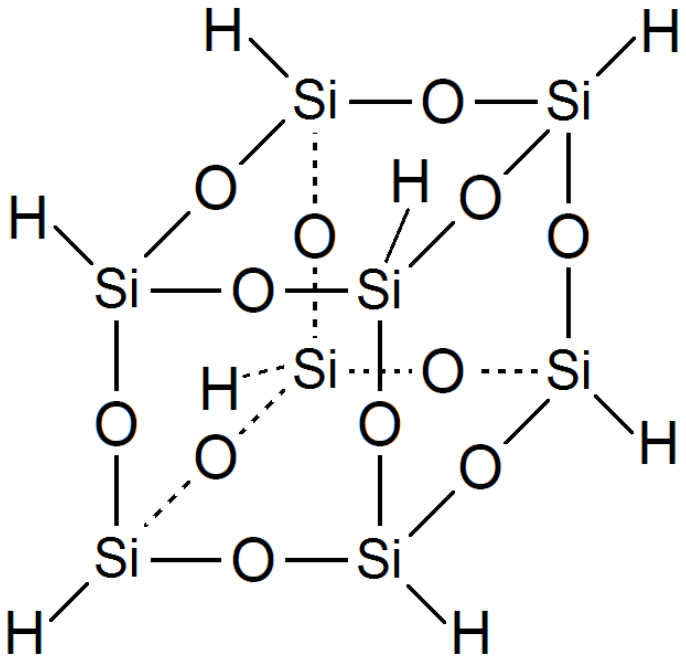

Fig. 2.3 The molecular structure of HSQ. Copyright © Mohammad Ali Mohammad's PhD thesis [94]. Reprinted with permission.

Upon exposure to electron radiation or thermal curing, the individual cage structure cross-links to a network structure [111,112]. The transformation mechanism from cage to network is not yet clearly concluded so far. The speculation is that the Si-H bonds break to create free radicals, the cages with silicon radicals at the vertices are connected by forming Si-O-Si linkage as shown in Fig. 2.4 [111,112].The most commonly used development chemistry for HSQ is based on an aqueous base, for instance, KOH, TMAH, NaOH and LiOH. Among these choices, TMAH with a high concentration is most suitable for patterning deep nanoscale because of its capability of high resolution [113,114]. Further, several techniques like adding salts into the developer, changing developer temperature, and HF trimming as an additional development step affect the

development rate and sensitivity. Properly adjusting these factors improves the lithography result. In a later section, HSQ is used to pattern SiCN nanowire resonators.

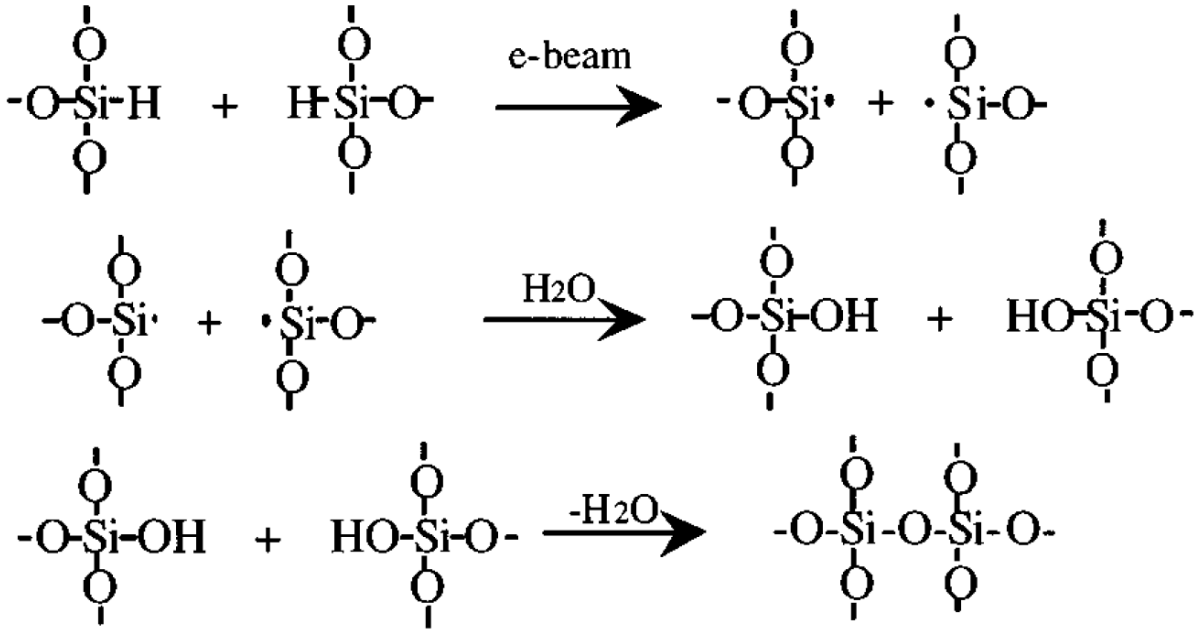

Fig. 2.4 Mechanism of cross-linking of HSQ caused by electron exposure. Reprinted with permission from [111]. Copyright © 1998, American Vacuum Society.

2.2.3 Silicon nanostring

The silicon nanostring was patterned to the desired geometry by using PMMA. Electron beam lithography patterns the resist by slow speed e-beam writing. The nano resonator feature takes a relatively small area of the design layout compared to the background substrate of the sample surface. The small geometry area of nano resonators were exposed to the electron beam and the left large area remained unexposed. As a positive resist, exposed PMMA is removed after

development. To form an etch mask for the desired silicon resonator geometry, a thin layer of metal is deposited and selectively lifted off by removing unexposed PMMA. The remaining metal became the etch mask. However, a frequent problem with the lift off process is the unwanted metal deposition along the sidewalls of the developed resist. During the removal of the unexposed resist, this part of the metal becomes floating and randomly sticks onto the surface of the sample. This causes inaccuracy or even failure of the lithography patterning, especially when the resist is thick and the developed resist has a high sloping profile, as depicted in the left panel of Fig. 2.5. To avoid this problem from occurring, bilayer PMMA is a solution. The PMMA 495 is spun on the bottom and the PMMA 950 is spun as the top layer. Because of the smaller molecular weight, PMMA 495 is more sensitive and forms a larger undercut than PMMA 950 as the result of EBL and favors the lift off, as shown in the right panel of Fig. 2.5.

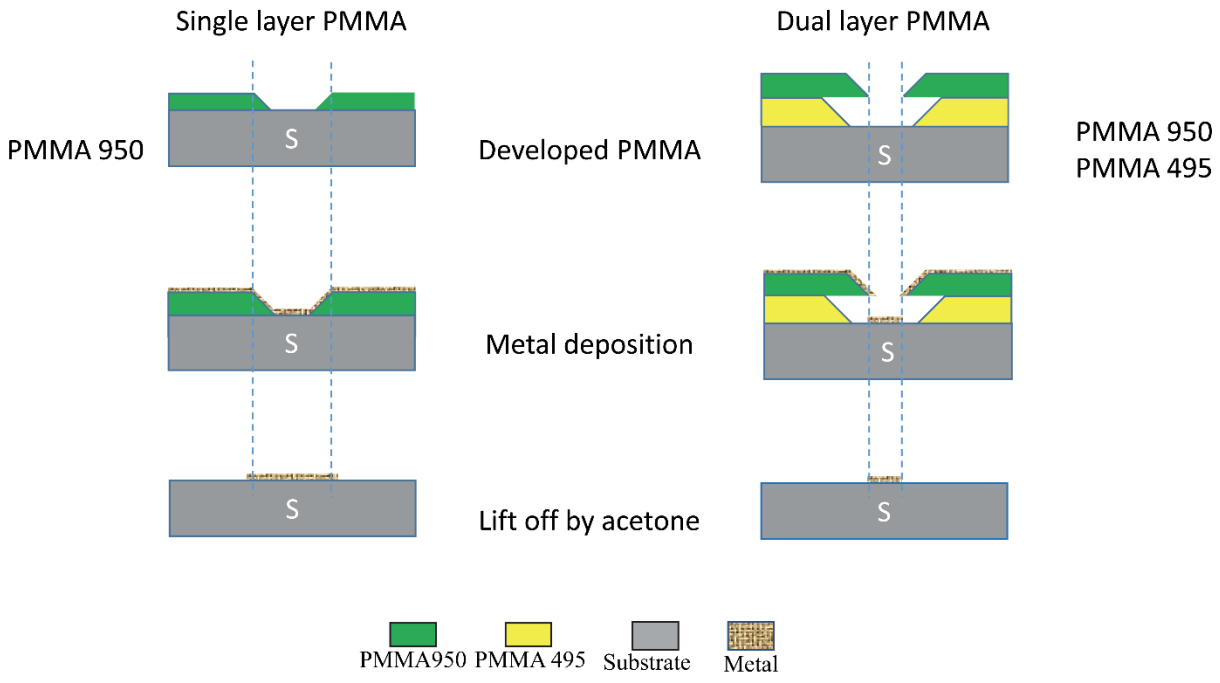

Fig. 2.5 Comparison of lift-off of single layer and double layers of resists

The fabrication process flow of silicon nanostring arrays from SOI wafer is shown in Fig. 2.6. First, the SOI wafer (Soitec) was diced into 1cm x 1cm chips. Then the SOI chip was piranha cleaned for 15 min and baked at 180^0C on a hotplate for 5 min to drive away the moisture. PMMA 495 A2 resists (Microchem) was spread at 500 rpm and spun at 3000 rpm onto the SOI chip. The chip was baked at 180^0C on hotplate for 10 min and cooled down for 2 min. The PMMA 950 A2 (Microchem) was spread at 500 rpm, spun at 3000 rpm on top and then baked at 180^0C on hotplate for 10 min. The total thickness of bilayer PMMA was 120-140 nm measured by Filmetrics. Bilayer PMMA was exposed to an electron beam at 10 kV acceleration energy, 20μm aperture under the area dose of 125 μc/cm^2. Exposed PMMA is developed by MIBK:IPA 1:3 for 60 s, rinsed by IPA for 15 s, DI water for 60 s and N_2 dried. A 25nm thick chrome layer is deposited on the developed sample by electron beam evaporation system (Gomez) at a pressure of 10^{-7} Torr. A 4mA current is controlled to confine the deposition rate lower than 1.5 Å/s in order to deposit this thin Cr layer. Cr layer on top of unexposed PMMA is lifted off by soaking in acetone with an ultrasonic bath for 5 min. The remaining Cr serves as mask layer protecting the underneath Si in the subsequent DRIE etch of silicon. Exposed silicon was anisotropically etched in ICP-RIE (Bosch) with alternative gas of C_4F_8 and SF_6. Then chrome was removed by dissolving in Cr-etchant for 25 s. Finally, the buried oxide layer was isotropically etched by BOE. The narrow nanostring was released while the big silicon pad was anchored to the substrate.

2.2.4 SiCN nanostring

Fig. 2.7 shows the fabrication process of the SiCN nanostring. The PECVD SiCN film was patterned by using a Raith 150 ^{Two}° EBL system. PMMA is chosen to pattern SiCN nanostring wider than 50 nm. The protocol of EBL patterning PMMA is similar to the one used for SOI wafer. Dual layer PMMA structure, with PMMA 950 A2 on top of PMMA 495 A2, is used to develop a

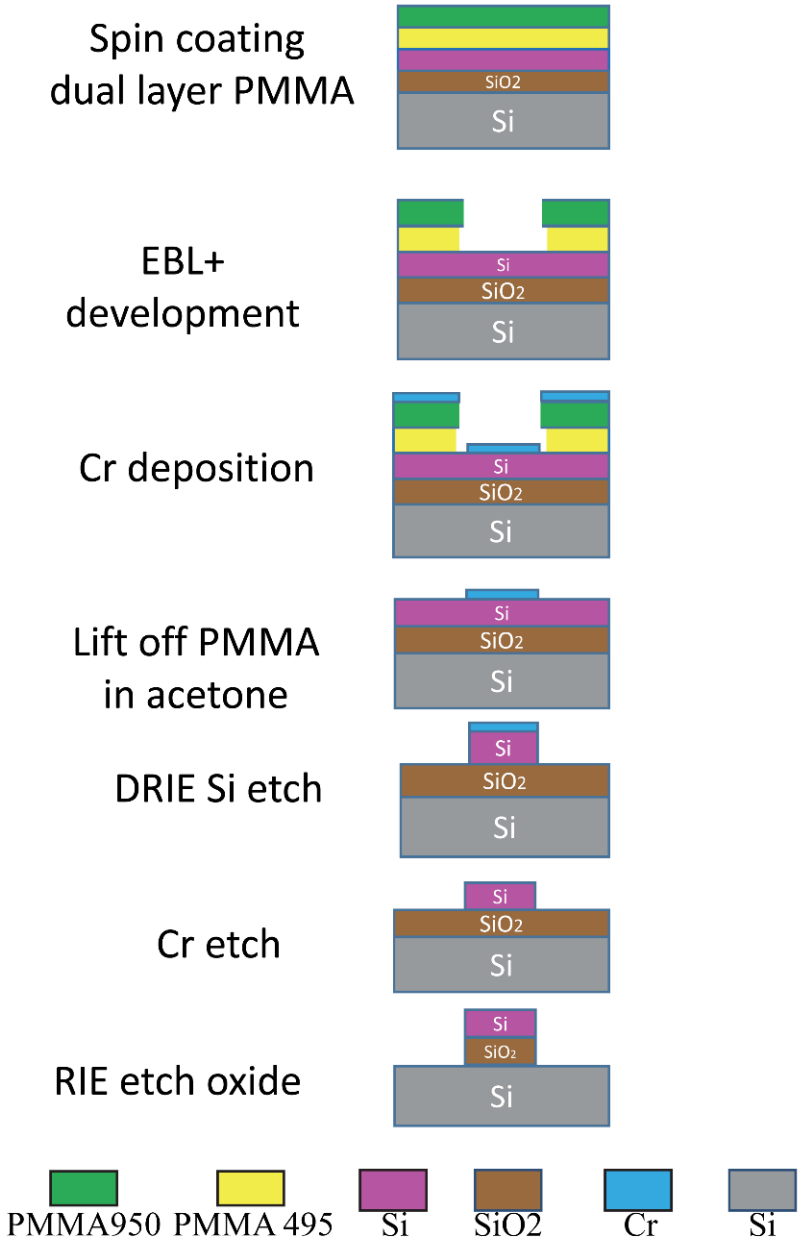

Fig. 2.6 Process flow of silicon nanostrings from SOI wafer

resist profile with wider opening on bottom than the top, which effectively prevents the failure of chrome lift-off in the following steps. Both PMMA 495 A2 and PMMA 950 A2 resists were spread at 500 rpm and spin at 3000 rpm. The EBL patterning of PMMA, metal deposition and metal lift-off were conducted using the same procedure and parameters for the case of SOI wafer as elaborated in the previous section. After lift-off, the Cr became the mask for the SiCN etch. The SiCN is RIE (Trion) etched away by using an etching recipe of 4:1 SF_6:O_2. An over etch of 35 s is used to guarantee thoroughly vertical etching. The chrome layer is removed in chrome-etchant.

Cleaning the sample before immersion in KOH solution is critical to a successful SiCN nanostring release. Because impurities introduced by previous processing steps contaminate the KOH solution, debris are produced and stick to the surface of the released resonators randomly. This type of debris is neither removable by cold piranha nor organic solvents like acetone and IPA. Even though the debris does not cause the fabrication failure of the nanostring, it affects the measuring accuracy and even causes the failure of the biosensor because the mass introduced by debris largely reduces the resonant frequency. However, it has been observed that the debris on nanostring surface is removed during the diazonium functionalization step, which may be due to the solubility of debris in the surface functionalization chemistry. As a result, the initial resonating frequency does not make sense and is not comparable to the protein loaded resonating frequency. Hence, before the KOH release process, the sample is cleaned in acetone and IPA and rinsed with water. Finally, the SiCN resonator is released by Si anisotropic etch in 35% KOH solution saturated with IPA at 75^0C for 40-135 s.

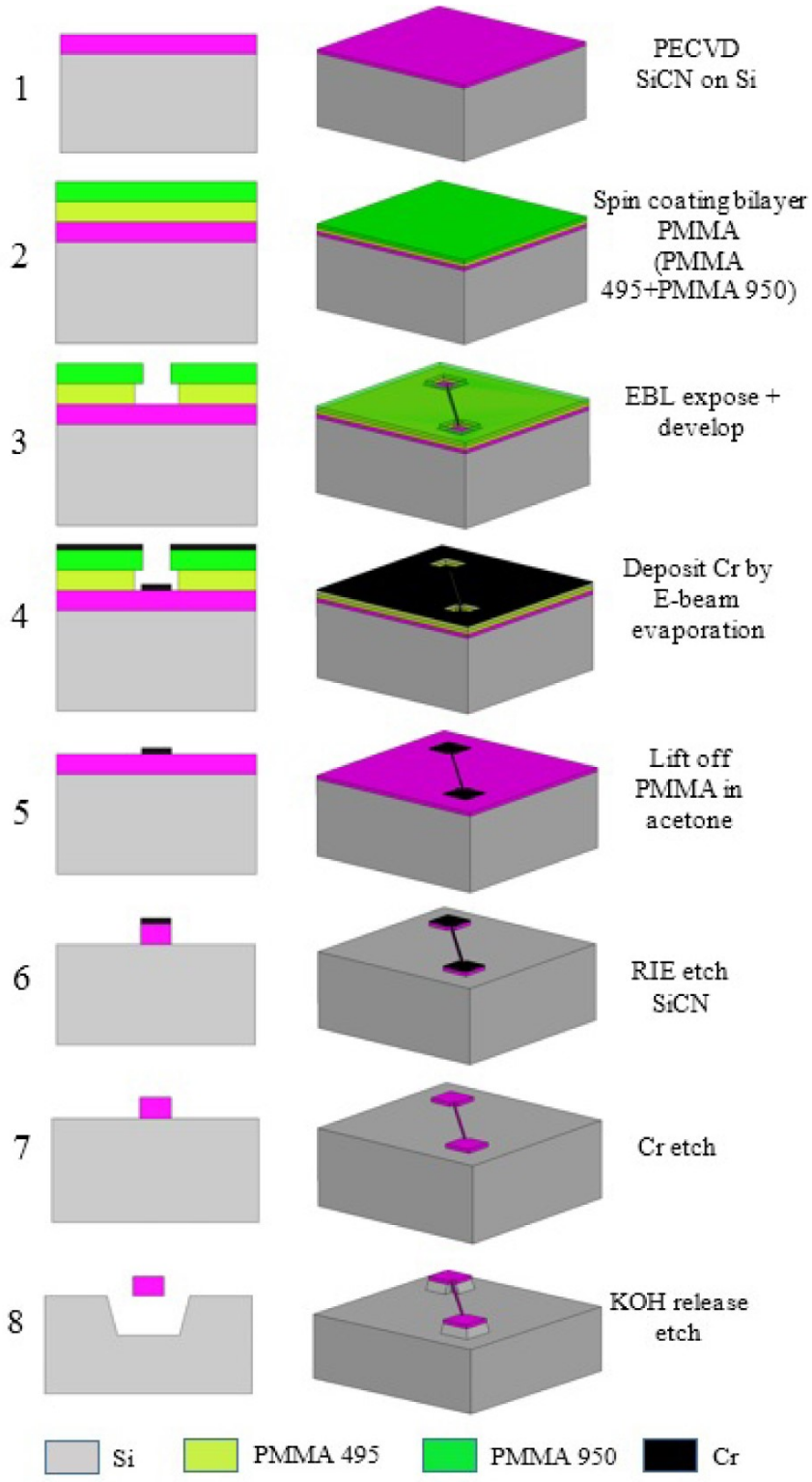

Fig. 2.7 Fabrication process flow of SiCN nanostring

2.2.5 SiCN nanowire

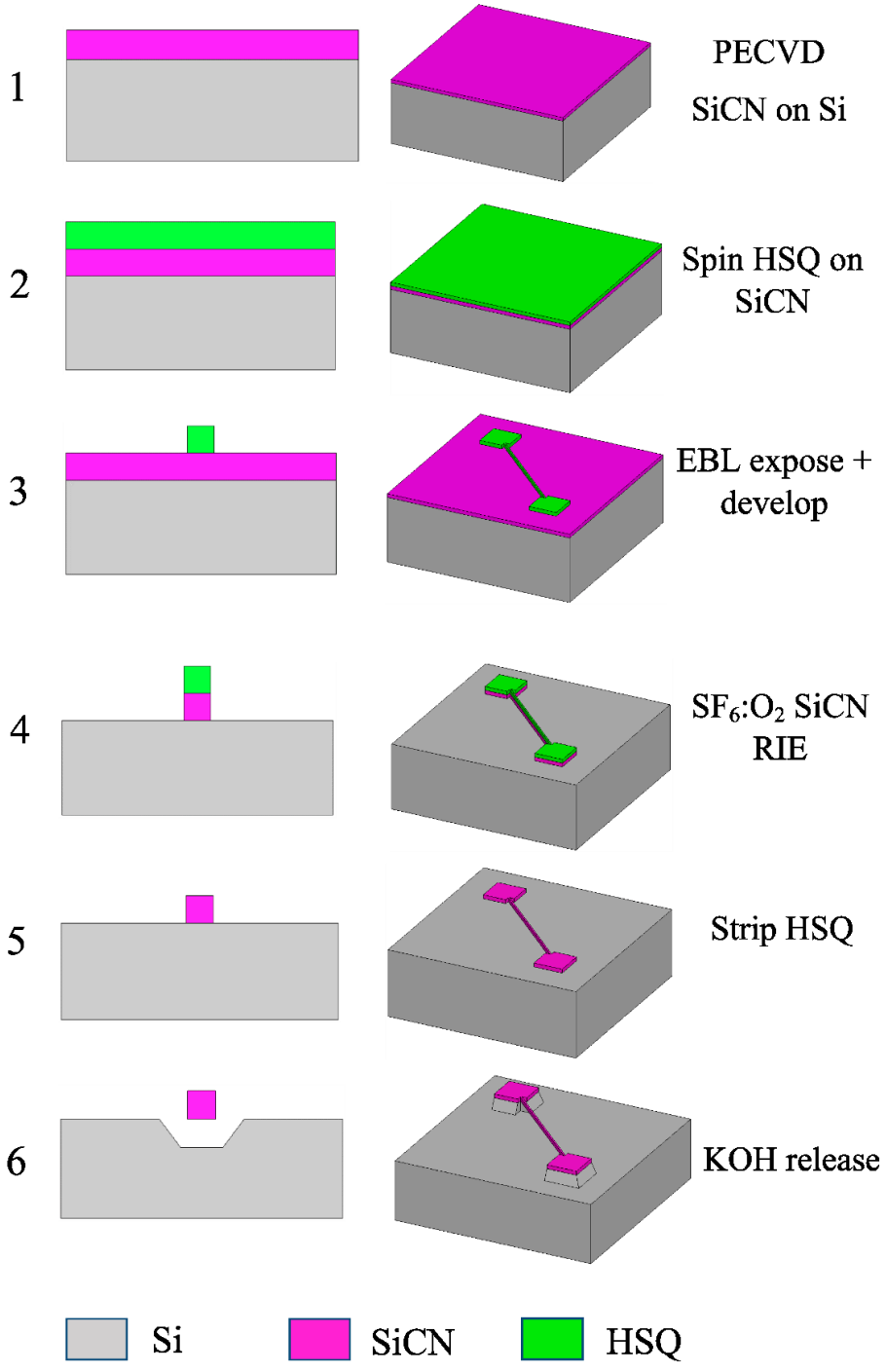

Fig. 2.8 Fabrication process flow of the SiCN nanowires

Besides the unbeatable high resolution below 50 nm line, another benefit of using HSQ is the simplified process sequence as compared in Figure 2.7 and Figure 2.8. When using the positive resist PMMA for EBL, a lift off procedure is needed. Chrome is deposited and selectively removed by EBL and lift off. The remaining chrome serves as mask for SiCN RIE etch. Lift off is a risky factor to lower the yield of fabrication. In the case in which metal is deposited along the sidewalls of the developed resist and fails to be lifted off with PMMA removal by acetone, the metal falls onto the substrate and results in an unexpected pattern of SiCN etch mask. But HSQ as a negative resist does not require the lift off process. After EBL exposure and development, the remaining HSQ itself serves as the etch mask for SiCN.

With the developed HSQ serving as a protection mask, the SiCN film was selectively etched by reactive ion etching (RIE) using 4:1 SF_6:O_2 for 35 s. The HSQ protection layer was then stripped by a 30 s dip in BOE. Finally, the SiCN strings were released as doubly clamped suspended strings by Si anisotropic etch in 35% KOH solution saturated with IPA at 75 °C for 40–135 s, depending on the string length.

Large arrays of nanostrings and nanowires with thicknesses of 50 nm, string lengths ranging from 5 to 15 μm, and widths varying from 10 to 300 nm were fabricated employing the above two processes that respectively use PMMA and HSQ as e-beam resist.

2.2.6 Microscopy inspection

SEM was performed to inspect the surface and bulk morphology of silicon nanostring, SiCN nanostring and nanowire resonators. For different scenarios and also due to the availability of the SEM tools, several SEM were used, which includes Zeiss LEO 1430 (Zeiss, Oberkochen,

Germany), JEOL 6301F SEM (JEOL, Tokyo, Japan) and Hitachi S4800 cold field emission SEM (Hitachi, Tokyo, Japan).

In addition, the SiCN nanostrings were individually imaged by ORION NanoFab Helium Ion Microscopy (Zeiss, Oberkochen, Germany) under a beam energy of 31 kV and a beam current of 0.4 pA.

2.3 Results

2.3.1 SiCN film elemental composition

Table 2.3 Elemental composition analysis of SiCN film

Element	Atomic concentration %	Mass Concentration %
N 1s	30	22
C 1s	31	20
Si 2p	39	58

Fig. 2.9 displays an x-ray photoelectron spectroscopy (XPS) survey of a typical SiCN film. Significant binding energy peaks are observed for silicon, carbon and nitrogen. Data analysis yields the quantitative elemental composition of the films (Table 2.3). The atomic Si:C:N composition ratio was roughly 4:3:3.

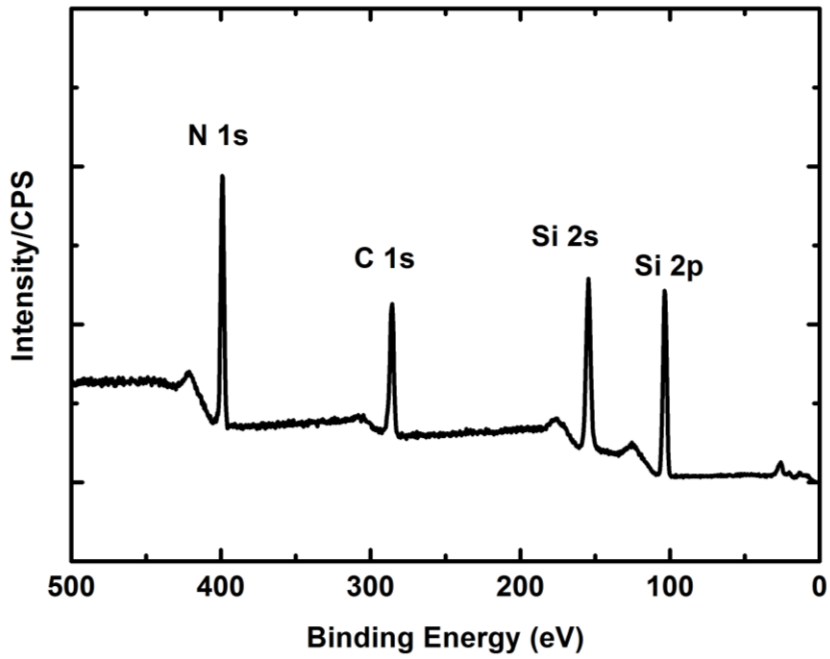

Fig. 2.9 XPS survey of SiCN film

2.3.2 SOI Nanostring

Fig. 2.10 shows the SEM images of silicon nanostrings inspected with a tilted angle. Panel A shows the overall view of nanostring arrays. As shown in panel B, multiple suspended nanostrings share the same pair of anchoring pads. This design layout increases the number of devices per unit area and thus saves the fabrication cost of each unit device. Panels C and D show the details of an individual nanostring, especially the gap between the nanostring and the substrate. Panels E and F show the anchoring pad. The undercut of oxide due to the isotropic etch of BOE is displayed.

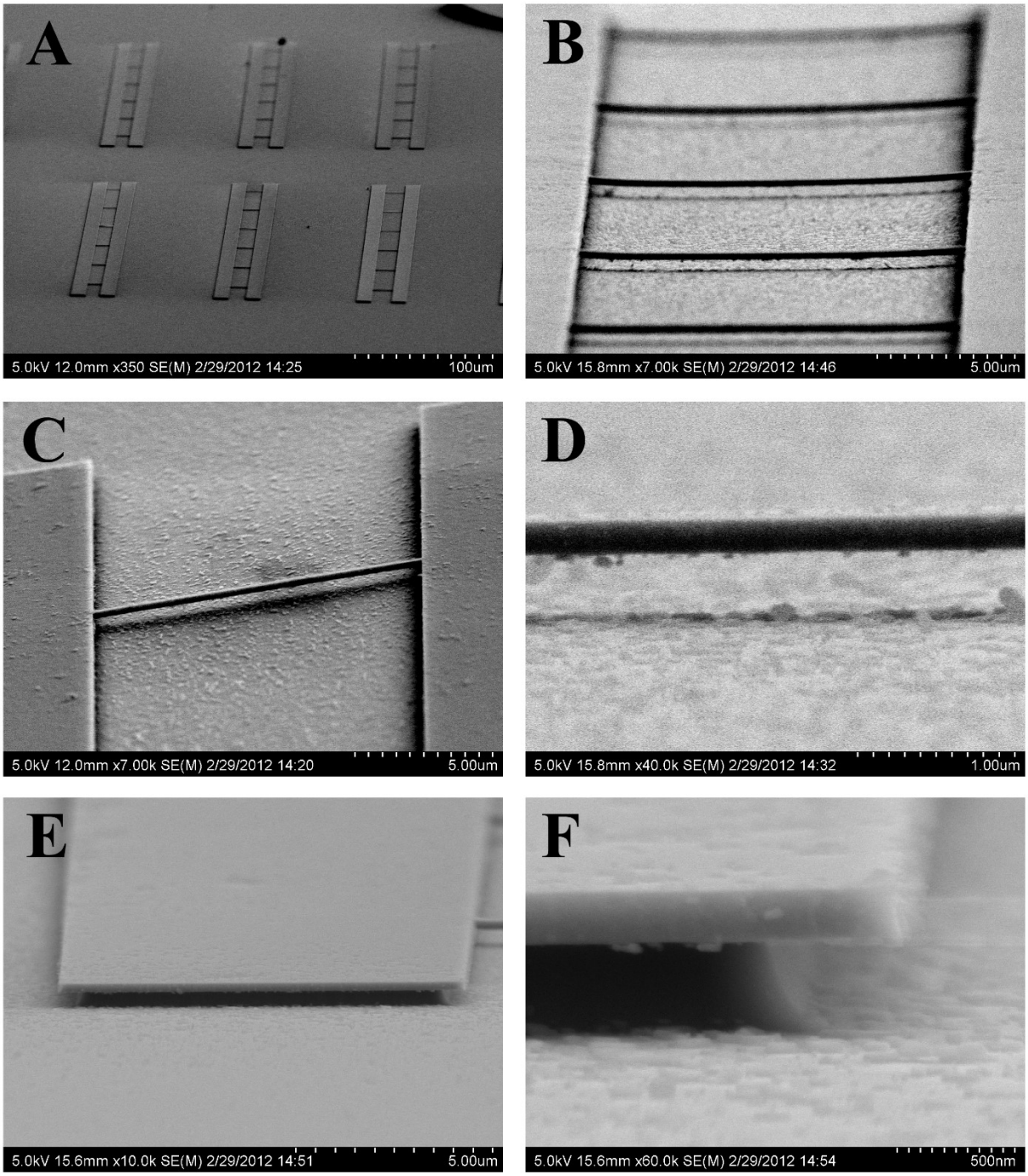

Fig. 2.10 SEM images of silicon nanostrings inspected with a tilted angle

Fig. 2.11 shows both the double clamped and single clamped nanostrings. Panels A and B respectively show the arrays. Random individual double clamped and single clamped nanostrings are shown in Panels C and D, with measured dimensions.

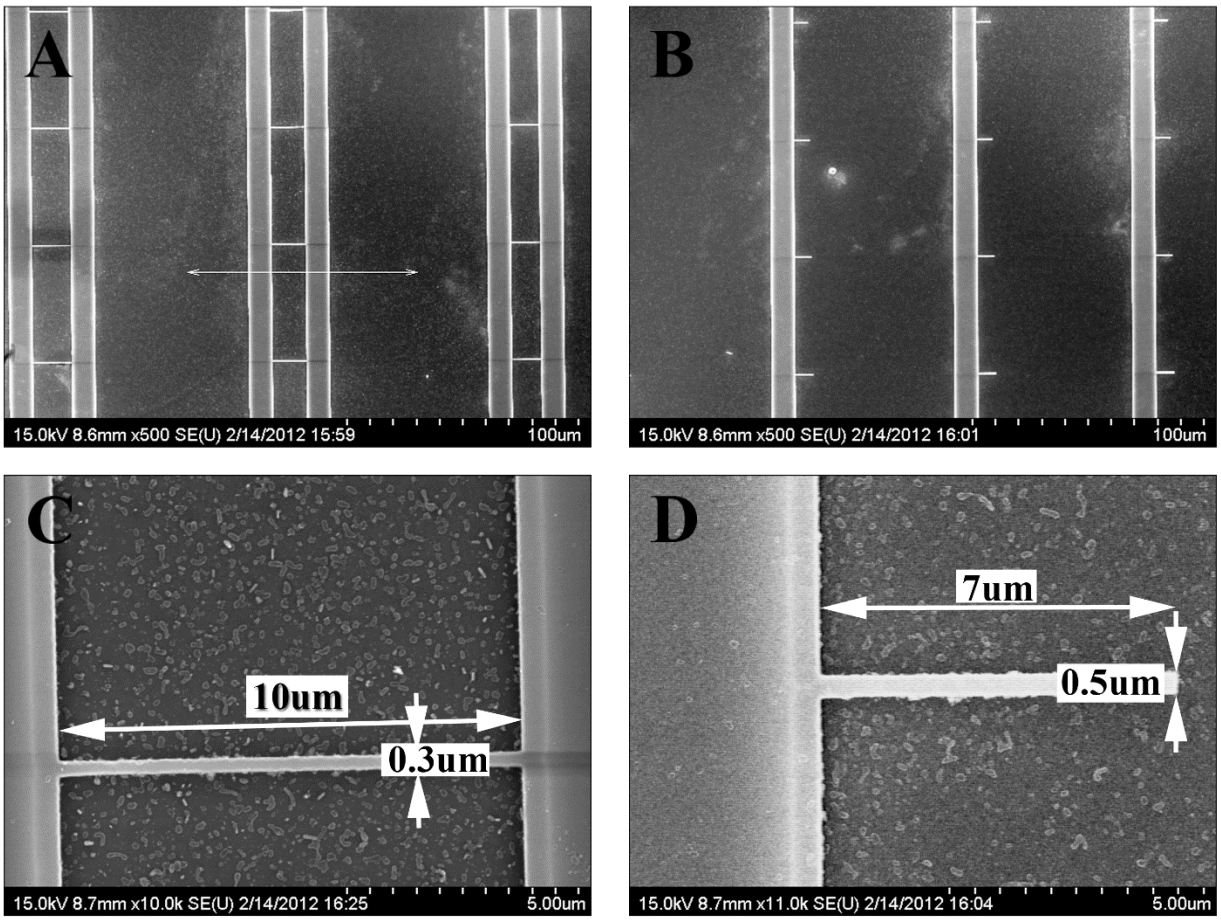

Fig. 2.11 SEM images of top view of silicon nanostrings

The sample was tilted 85^0 for SEM imaging (Fig. 2.12) in order to measure the height of the gap between the nanostring and the substrate. The gap height varies from 240 nm to 336 nm along the string, the center points are with smaller gap heights compared to the anchoring ends. This variation agrees with the observation shown in panel B of Fig. 2.10.

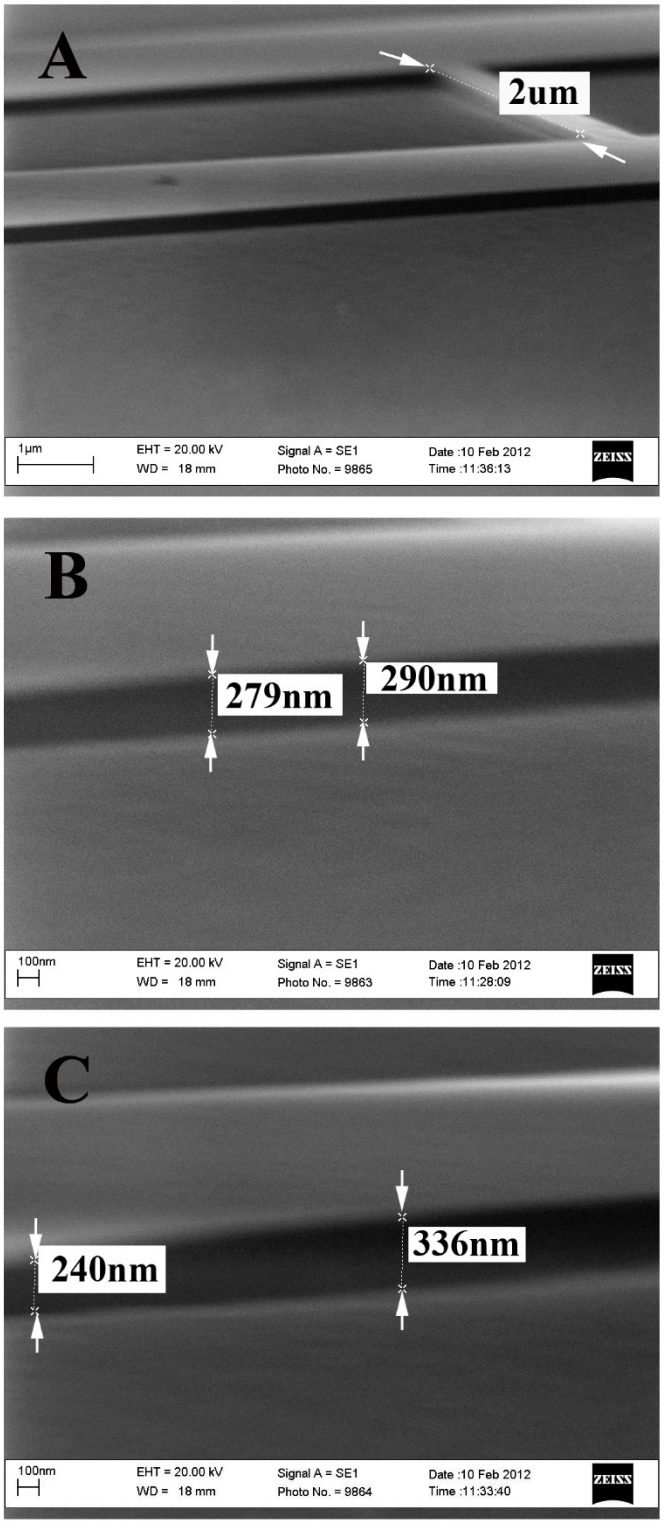

Fig. 2.12 SEM images of side view of silicon nanostrings

2.3.3 SiCN nanostring and nanowire

The SEM images of SiCN nanostrings and nanowires are shown in Fig. 2.13. Panel A displays an array of nanostrings. The width of the nanostrings ranges from 300 nm down to 180 nm as labeled at the left column of the array. For each width, there are five identical nanostrings in the row. Panel B shows a random individual nanowire. Both the suspended SiCN nanowire and the anchoring pads are displayed. The bulk silicon of the anchoring pads shows a pyramid profile. This is due to the anisotropic silicon etch by KOH solution. The thin SiCN film of the anchoring pads shows big undercuts in the three corners which do not connect with the suspended nanowire. This is due to the superimposed anisotropic etching effect from both the vertical directions. The corner of the anchoring SiCN that connects to the nanowire shows a relatively smaller undercut because of the design of the inward corner. This design avoids the big overhanging SiCN area. Panels C and D show the comparison of proper etch and over etch of bulk silicon using KOH. Panel C shows an example of proper timing of silicon etch, in which the SiCN film shows a sharp edge at the anchoring point. As contrast, panel D shows the result of over etch in KOH. The SiCN film shows a rather rounding anchoring point. The reason is that KOH etches SiCN, although at a slower rate than Si. Timing of the KOH etch is critical to the successful release of SiCN nanowire. In the silicon etching process, proper etching time ensures the gap between the nanowire and the substrate is big enough. At the optimum time, it does not cause obvious etching of SiCN as shown in panel C. But if the etching time is more than enough, KOH etches the SiCN, as displayed in panel D. In the worst case, prolonged KOH etching leads to breaking of the SiCN nanowire and nanostring. In panels E and F, the nanowire was imaged under 500 000 and 800 000 times magnification for the accurate measurement of its width. Panel E shows the ultimate large magnification view of the

nanowire, the measured width of which is 10 nm. In panel F, three random sampling points show different widths of 11nm, 12nm, and 13nm along this nanowire. Due to the tolerance of EBL, SiCN etch, KOH etch and the SEM meausrment, the differences are acceptable. The implementation of ultra-narrow nanowire is a prerequisite for ultrasensitive biosensor capable ofdetecting individual molecules. Previous studies employed complicated processes for HSQ development to obtain as high as 10 nm resolution [42]. Increasing the temperature of the developer to 40-50^{0}C or using HF dip as an additional development step can help improve feature resolution. However, in this process, merely regular simple development of HSQ achieves this same goal.

SiCN is an electrically non-conductive material. Since the thickness of the SiCN nanostring is as thin as 52 nm and the SiCN thin film is connected to the underlying silicon, no significant charging effect occurs during the SEM inspections. An imaging instrument, which does not produce electron charge at all, is able to discover finer details of the device morphology. Hence, helium ion microscopy is performed to image the SiCN nanostrings, the result of which is displayed in Fig. 2.14. Seen from panel A and panel B, the bulk silicon pyramid was anisotropically etched. The four etching planes at the corner of the silicon anchoring point are displayed. The edges along the sides of the SiCN anchoring pad are thinner than the majority middle area because of the KOH etch of SiCN. The same thinning edge effect is observed for SiCN strings as shown in panel C.

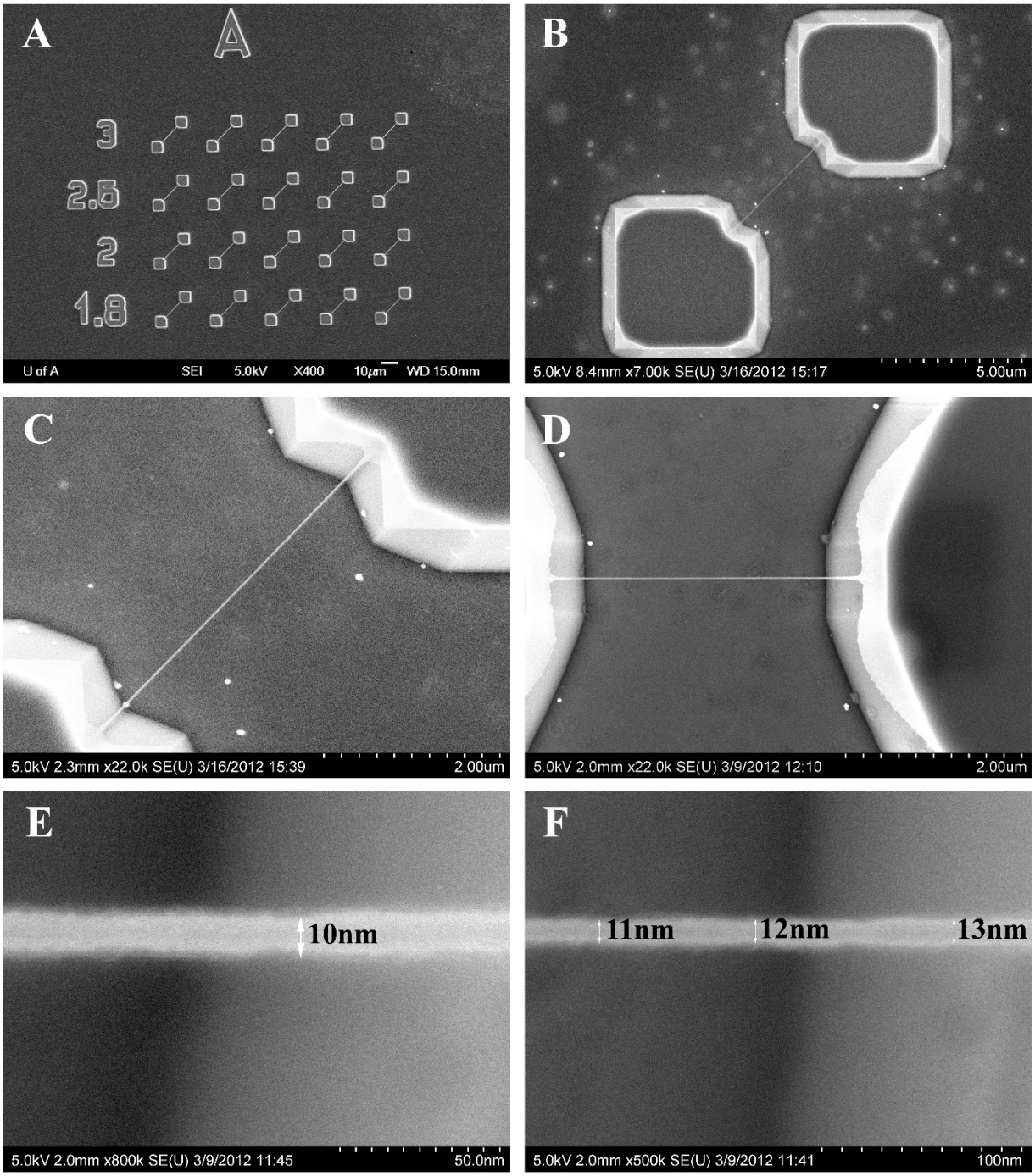

Fig. 2.13 SEM images of SiCN nanostrings and nanowires

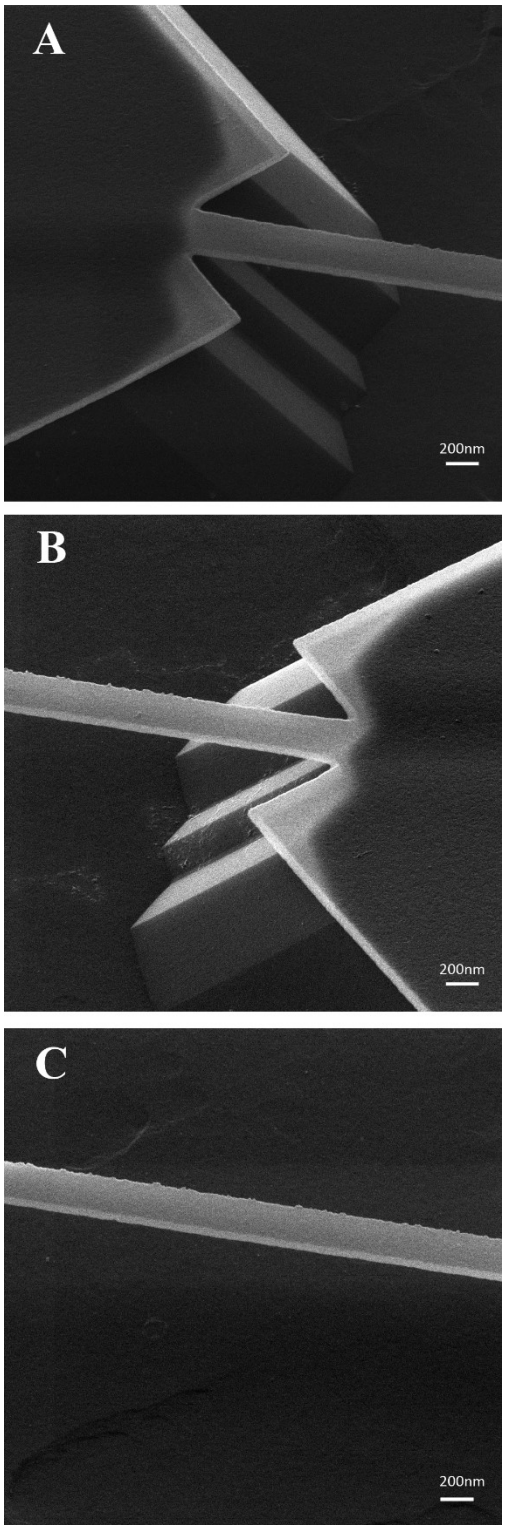

Fig. 2.14 HIM images of SiCN nanostrings

The advantage of using HIM is obvious by direct comparison of HIM and SEM images. At the locations of overhanging SiCN pads and suspended SiCN nanostring, where no underlying silicon exists, HIM images show as high resolution as they do on the centering area of SiCN pads and the silicon substrate. This is because helium ion beam does not build charge on the surface of SiCN. In contrast, the SEM images of the locations without underlying Si is relatively blurry compared to the SEM images at the locations where bulk silicon is present as background substrate and anchoring material beneath SiCN. This is due to the accumulated charge by the electron beam.

Compared to Si nanostrings, the advantages of SiCN nanostrings and nanowires are obvious. The anisotropic etch of bulk silicon makes big gap between the nanostring/nanowire and the substrate and a relatively small undercut in the anchoring pads. This etch-release process does not have stiction effect even without the assistance of CPD.

2.4 Conclusion

This chapter describes the fabrication of nanostrings and nanowires. Common electron resist PMMA and high resolution resist HSQ were respectively used for e-beam lithography patterning. SOI based nanostrings were fabricated by etching the sacrificial layer and release of the silicon film. The SiCN nanostrings and nanowires were released by bulk etching of silicon. SiCN nanowires as narrow as 10 nm wide have been achieved, which pave the way for single molecule detection. These fabrication processes have high yield and repeatability.

Chapter 3 Helium ion beam milled porous nanostrings

3.1 Introduction

3.1.1 Novel structure of porous nanostring

As stated in the previous chapter, reducing the mass of the string is crucial to enhance the detection sensitivity. Narrowing down the string width is direct and effective to lower the mass. However, there are technical bottlenecks in terms of fabrication and measurement of ultra-narrow nanostrings and nanowires. First, the dimensions of the nanostring and nanowire are defined by the lithography process. Therefore, the widths of nanostring and nanowire are confined by the intrinsic limitation of the lithography technique, which is EBL in this thesis work. Etch-release process is another factor limiting the widths of the nanostrings and nanowires. Nanostrings and nanowires with narrower widths have increased risk to break during etch-release process. Second, the interferometry measurement of nanowires becomes challenging because of the increased difficulties to focus and align the laser paths precisely on the extremely narrow nanowires.

To circumvent the issues, a novel structure of porous nanostring is proposed, which has the same width but significantly reduced mass due to the removal of material volume from hollow pores. By accurate calculation and control of the number and the size of pores along the string, the reduced mass of nanostring is precisely controlled. The mechanical property, like the film stress, of the nanostring is tuned because of the distribution of pores. Additionally, the surface adsorption

area of the string could be increased as long as the radius of the pores is smaller than the thickness of the string. This extra benefit provides a larger amount of absorbed biological molecules and a higher output signal compared to regular non-porous strings. This novel porous structure is expected to simplify the fabrication and measurement as well as tune the physical and chemical properties of nanostrings.

3.1.2 Fabrication challenge of porous nanostring

Despite the expected merits of the porous nanostring, fabrication by the traditional top-down process is technically challenging. Due to the small size and dense distribution of the pores along the nanostring, there exists uncertain issues in the process of lithography photoresist development, etching of the pores and etch-release of string. For example, the pores need to be etched through by RIE. Etching relatively big and sparse pores should not be a problem for an RIE etch of SiCN. But when the pores become extremely tiny and densely neighbored, it is hard for the etching gases to reach the bottom of the trench and the reaction products to escape from the trench. Since RIE etch of SiCN is isotropic, over-etch may result in lateral etch, which enlarges the pore size. Besides, as shown in the SEM image and discussed in the previous section, KOH etches the SiCN film. The circular edges of the small pores could be etched by KOH. In the case of dense distribution of pores, the nanostring may break by KOH etching. It is estimated that traditional top-down fabrication may have device failure and low yield. Hence, a method which does not alter the existing process of regular nanostrings but only etches pores in the suspended nanostring is preferred.

3.1.3 Post-fabrication of ion beam milling

Since there is no material etch selectivity between the target pores and the rest of string, the target material should be removed by a physical method. FIB milling is directional with high energy, which sputters away the target material at accurate locations without interfering with the non-target area. Hence, FIB technique is a good candidate to mill the nanostring from the top surface until etching through the bottom to form the pores. Based on the nature of FIB technique, this proposed novel fabrication method could precisely control the dimension, location and the number of pores in the nanostring.

There are two main stream sources of ion beam for both imaging and milling purpose, Gallium and Helium. Although Gallium ion beams are more frequently used, Helium ion beam was chosen instead considering the specific characteristics of the SiCN nanostring sample. The reasons are stated in detail as follows. First, the FIB milling needs to be performed under microscopy so that the ion beam can precisely locate the target area of the sample. Helium ions provide higher imaging resolution compared to Gallium ions. The sample SiCN nanostrings have width varying from 180nm-300nm. Thus, Helium is a better option as an imaging source. Second, when the Gallium ion beam mills, the ions tend to deposit a relatively thick layer on the surface of the target sample. As the SiCN film is as thin as 50 nm, the added thickness caused by Galium ion deposition increases the thickness and the mass of the nanostring. This causes side effects to the mass sensitive sensors as the added mass lowers the sensitivity. In contrast, the Helium ion beam does not introduce as significant of a deposition layer while milling. Third, Gallium element is chemically active and the deposited Gallium ions on the sample may possibly alter the chemical properties of the surface. When applied as a biosensor, the surface modification may be affected by the deposited Gallium ions. However, as a noble element, Helium is not chemically active and less

likely to cause problems for surface functionalization. In summary, Gallium ion beams potentially bring physical and chemical alternation to the milled sample while having a weak resolution compared to Helium. Hence, Helium ion beam is selected to mill pores along the regular SiCN nanostrings.

Recently, Helium ion beams have been reported for the in-situ modification and imaging of nanoscale features [115–120]. More specifically, finely focused Helium ion beams have been used for the milling of pores in SiN [121,122] and Si [123] membranes. Such accuracy offers potent possibilities for the tuning of mechanical properties of suspended structures. More specifically, local milling of nanostrings would enable design of resonant mode shapes and possible control over clamping issues [96,99,124].

3.1.4 Content of this chapter

In this chapter, a novel structure of porous SiCN nanostring has been proposed [125]. The method of helium ion microscope-assisted nanomachining of resonant nanostrings has been first demonstrated. More specifically, the helium ion beam is used to locally mill pores along the length of the glassy nanostrings. This effect of this machining on resonant mode shape and frequency is assessed using both finite element analysis and experimental observation.

3.2 Experiment

3.2.1 Helium ion beam milling of SiCN nanostrings

As a typical post fabrication process, focused ion beam milling was performed on the regular SiCN nanostrings which were already fabricated from top-down process as described in Chapter 2. As

initial demonstration of the feasibility of the ion beam milling process, relatively large nanostrings with width from 180nm-300nm were selected. Nanowires are very delicate, which means the energy of bombarding ions need to be tuned and controlled to avoid physical damage to the nanowire.

Helium ion milling of holes on 200 nm-wide nanostrings was performed in a Zeiss Orion NanoFab Helium Ion Microscope (Carl Zeiss AG, Oberkochen, Germany). The milling was performed using an ion beam current of 13.7 pA, a beam energy of 31 keV, and a nominal beam size of 0.5 nm. The patterning was performed with a step size of 1 nm at a dose of 30 nC/m^2. For a given device, the initial beam alignment took 10 min. The sample positioning and stage settle-down took an additional 10 min. The holes were then patterned successively with a milling time of 5 s per hole. The modification consisted of milling a linear array of holes along the length of the string. The individual holes had a diameter D = 45 nm, with a center-to-center spacing of s = 120 nm.

3.2.2 Laser interferometry measurement

An optical interferometric technique [32,71] was employed to measure the resonance frequency of the nanostrings. The resonator chip was attached to a piezoelectric disc and placed in a vacuum chamber (10^{-3} Torr). The piezoelectric element was actuated using the tracking output of a spectrum analyzer (Agilent E4411B). The beam of a 633 nm He-Ne laser source was expanded, power attenuated, directed by a 50: 50 beam splitter and focused by a microscope objective lens on the resonator string surface. The respective reflections from the vibrating string and the underlying substrate induce interferometric modulation of the optical signal. The resulting fringe pattern was passed through the objective lens, redirected by the beam splitter, focused by a convex

lens, and impinged on the AC coupled photo-detector. The photodetector output is then fed back to the spectrum analyzer. The resonant frequency was measured at the largest amplitude of vibration.

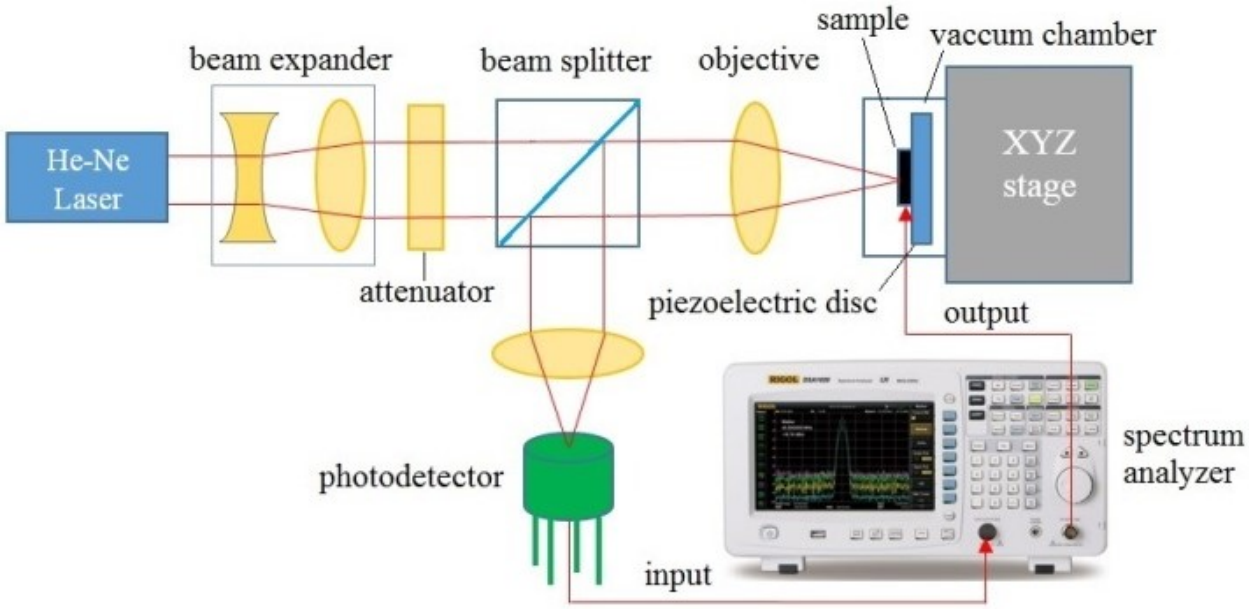

Fig. 3.1 Fabry-Perot type interferometer setup. From reference [70]

3.2.3 Finite element analysis

Finite element analyses were performed using COMSOL Multiphysics version 4.3 (COMSOL Group, Burlington, MA, USA) in 3D solid, stress-strain mode using its structural mechanics module. The doubly clamped beam was modelled as a rectangular box with dimensions of 15 μm in length, 200 nm in width, and 50 nm in thickness, and clamped at both extremities along the long axis. The material properties employed were a density ρ = 2200 kg/m3 and a Young's modulus of E = 108 GPa, as per experimentally measured values reported in ref. [98]. The intrinsic

tensile stress was defined along the longer axis in the linear elastic material model as an initial stress.

For the unmilled beams, a mesh composed of 7703 tetrahedral elements was created using the physics-controlled meshing technique. The eigenfrequency analysis was performed in two steps. Firstly stationary analysis was performed to solve for the effect of initial stress on the resonator. Secondly the frequency response of the resonator was determined through eigenfrequency analysis. Additional simulations performed with 57,117 tetrahedral elements yielded resonant resonant frequencies that were within 0.02% of the one obtained with 7703 elements.

We also simulated the effect of the milled holes on the calculated resonant frequencies. In those simulations, linear arrays of holes with 45 nm diameter and centre-to-centre spacing of 120 nm were defined along the length of the string. Additional simulations in which the holes were substituted by a hypothetical material of Young's modulus equal to the one of the SiCN, but with a near-zero density were also conducted. These additional simulations were performed to untangle effects related to mechanical properties from effects related to density. The eigenfrequencies were computed through the aforementioned two steps analysis. Both sets of simulations employed a mesh of 92,243 elements in order to insure accurate rendering of the holes. Additional simulations involving 288,720 elements yielded resonant frequencies falling within 0.1% of those obtained with 92,243 elements. The frequency shifts were calculated with respect to the eigenfrequency of the original resonator.

3.3 Results and Discussion

3.3.1 Porous SiCN nanostring

Figure 3.2 (a) shows an array of SiCN nanostrings milled with a helium ion beam. Figures 3.2 (b)(c)(d) shows higher magnification images of the nanostring indicated by the arrow in (a). The presence of the linear array of milled pores is clearly visible along the length on the structure.

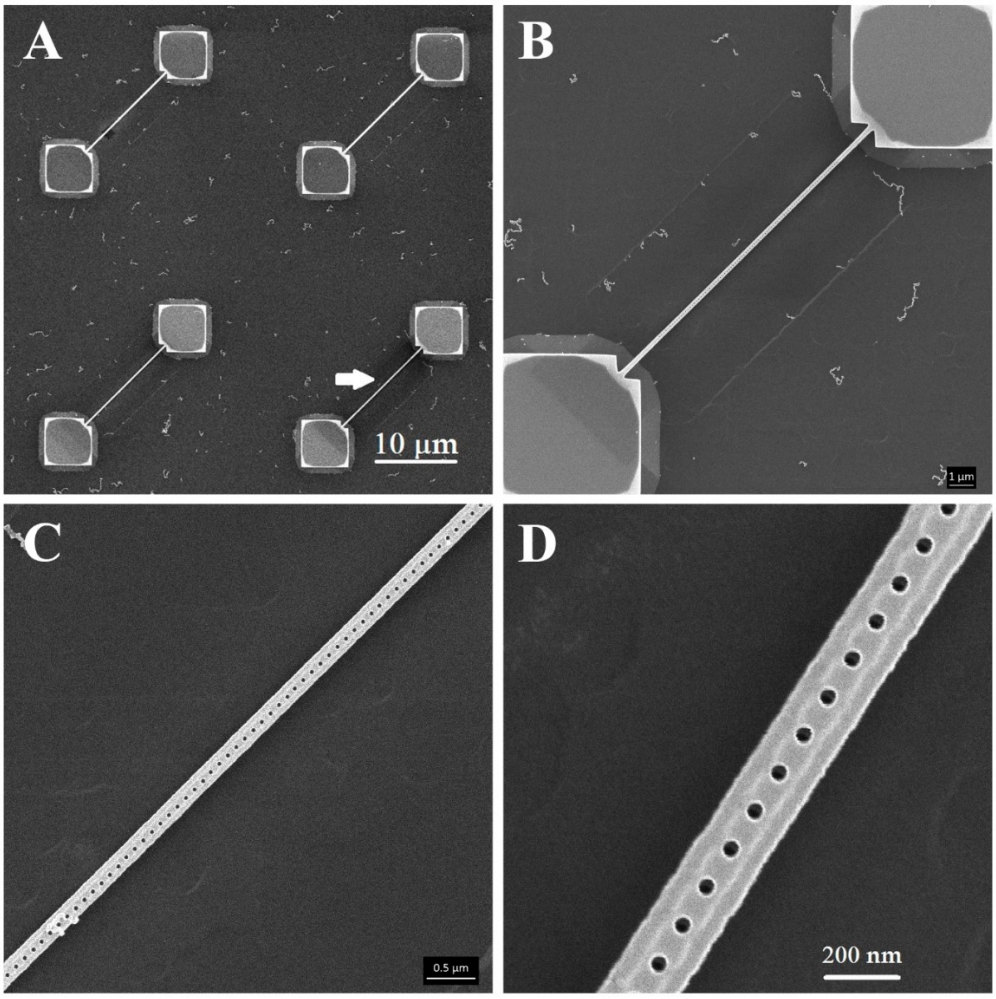

Fig. 3. 2(a) Array of nanostrings with helium ion beam-milled pores, (b)(c)(d) High magnifications images of milled nanostring shown by arrow in (a).

The disadvantage of involving FIB technique for porous nanostring fabrication is low etching speed of nanopores- compared to normal top-down fabrication. As shown in Fig. 3.3, the FIB moves to the designed location, sputters away the material until etching through, then moves to the next location, repeating the same action. Similar to the case of EBL, this time consuming procedure is not suitable for batch fabrication. Nevertheless, by the nature of FIB, the HIM milling based post-fabrication method is a flexible, controllable and repeatable process with high yield.

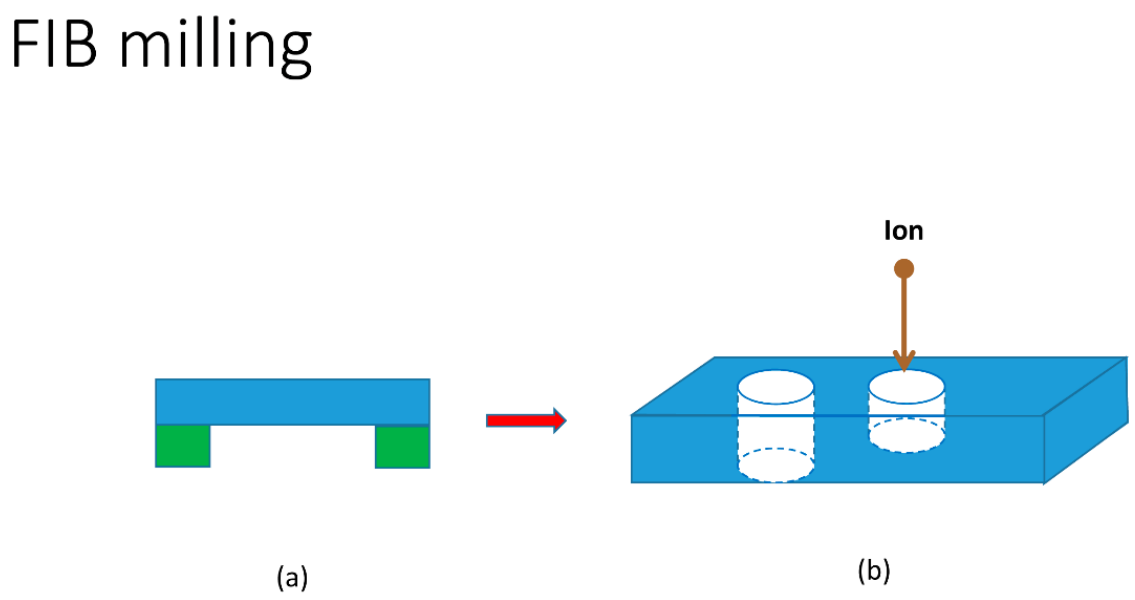

Fig. 3.3 FIB milling of nanostring: (a) regular nanostring; (b) ions mill through the string and form the pores

3.3.2 Tuning of resonant frequency of porous nanostrings

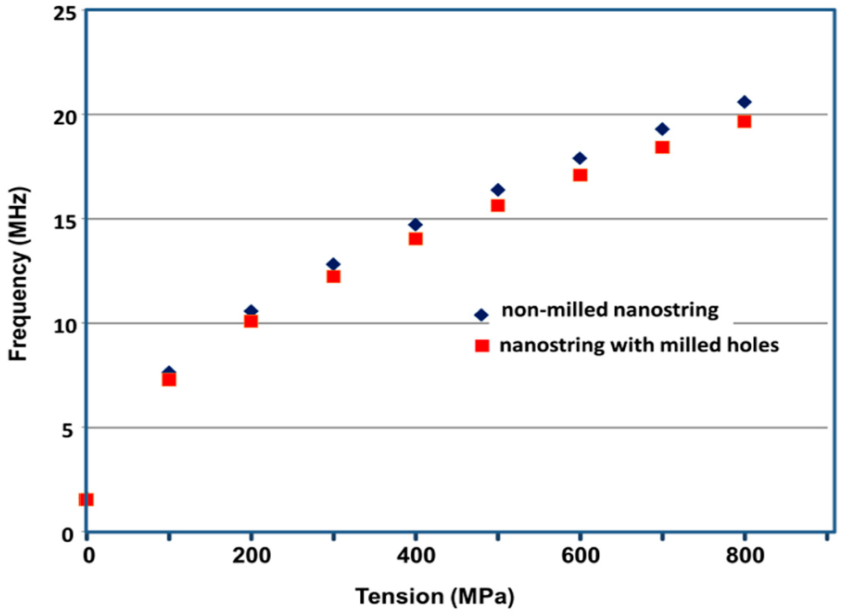

Fig. 3. 4 Finite element analysis of the resonant frequency of SiCN nanostrings of length L = 15 mm, width W = 200 nm and thickness t = 50 nm under varying tensile stress. Results for non-milled strings and strings milled with linear array of pores of diameter D = 45 nm and center-to-center spacing s = 120 nm are shown.

The fundamental resonant frequency of a beam of rectangular cross-section, clamped on both ends, under no stress, and vibrating perpendicular to is thickness is given by [126,127]:

$$f_0 = 1.028 \frac{t}{L^2} \sqrt{\frac{E}{\rho}} \tag{3.1}$$

where E, t and L are the Young'smodulus, density, thickness and length, respectively. When a tensile stress is present along the axial direction, the resonant frequency f_0 will be changed to a new value f_1:

$$f_1 = f_0 \left(1 + \frac{0.295\sigma L^2}{Et^2}\right)^{\frac{1}{2}} \tag{3.2}$$

The reader can consult ref [127] for the derivation of Equations 3.1 and 3.2. A systematic analysis of clamped-clamped resonators fabricated in this material has been reported in [98]. In that work, clamped-clamped resonators showed a $L^{\prime 0.999}$ dependence of f_0, suggesting that the devices were operating in the high-stress limit and thus dominated by the second term of Equation 3.2. The same analysis of singly clamped vs doubly clamped devices inferred a density ρ = 2200 kg/m^3 and a Young's modulus of E = 108 GPa [128]. This being said, this material was also found to present substantial variation of tensile stress within different locations of a given wafer, and from wafer to wafer. In our experiments, the tensile stress each device is under is thus a priori not precisely known.

The simulated resonant frequency of non-milled nanostrings of width W = 200 nm, thickness t = 50 nm and length L = 15 um as function of tensile stress is found in Figure 3.4. The resonant frequencies range from f_0 = 1.6 MHz for σ = 0 MPa to f_0 = 20.6 MHz for σ = 800 MPa. Once again, the relationship between frequency and stress becomes linear for stresses above 350 MPa, further confirming that the frequency becomes dominated by second term of Equation 3.2 above those values. As described later in this section, the simulation results agree with the experiment values.

The simulated resonant frequency of milled nanostrings of similar dimensions is shown on same figure. In these simulations, a linear array of holes of diameter D = 45 nm and center to center spacing s = 120 nm is included in the modelling. As seen in Figure 3.4, the presence of the holes reduces the resonant frequency by 4.5% independently of tensile stress.

The presence of holes is expected to affect both the effective mechanical properties of the string (such as Young's modulus and tension), as it does affect its effective linear density. While a reduction of tension and Young's modulus would decrease the resonant frequency, a reduction of linear density would rather increase it. To untangle the effects, another set of simulations was conducted in which the holes were rather replaced by a hypothetical material whose Young's modulus was equal to the one of the SiCN, but whose density was near zero. In that case, the nanostructuring increased the simulated resonant frequency by ~3%. Indeed, by keeping the average Young's modulus constant, these simulations now solely accounted for the reduction of linear density of the material. From Equation 3.1, the following approximate relationship is derived:

$$\left|\frac{\Delta f}{f}\right| = -\frac{1}{2}\left|\frac{\Delta \rho}{\rho}\right| \tag{3.3}$$

While the volume of the original string equals 150 x 10^6 nm^3, the combined volume of the holes totals 9.94 x 10^6 nm^3. The holes thus reduce the linear density of the string by 6.7%. Equation 3.2 would thus predict that such 6.7% reduction would result in a 3.3% increase of resonant frequency, as observed in the simulations.

As mentioned above, the presence of fully voided holes did however result in a net reduction of 4.5% of the frequency, in spite of the 3.3% increase that would result if only change of effective density would be involved. In addition, this 4.5% net relative decrease is independent of tensile stress, thus indicating that the presence of holes affects both the Young's modulus and the axial stress (second term of Equation 3.2) equally. This behavior was not unexpected given the relationship existing between Young's modulus E, stress σ and strain ε:

$$\sigma = E\varepsilon$$

Indeed, the milling of the holes is not expected to relieve the beam from the tensile strain σ it is under. This being said, the milling of holes effectively reduces the average Young's modulus E, thus in turn affecting the stress σ the device is under. Such mechanical effect would offset the effect of reduction of density with the net result of having the string's resonant frequency be reduced by the milling through reduction of both E and σ.

Non-milled and milled devices were then measured using the interferometry system. The average resonant frequency of non-milled devices was measured at 13.5 ± 0.2 MHz. The devices showed a resonant quality of Q = 5500 as measured from the full-width at half-maximum. When comparing this result to the simulated values (Figure 3.4), this corresponds to a tensile stress approximately 375 MPa, within the range usually observed from this material. In turn, the resonant frequencies of the milled devices were measured to be 12.8 ± 0.3 MHz. A ~5% net reduction of frequency is thus observed, as was predicted by the FEA analysis of the devices. The quality of the resonance was not measurably affected by the milling. This being said, this reduction of resonant frequency is accompanied by a net increase of surface-to-volume ratio. Indeed, a 15 μm x 50 nm x 200 nm non-milled string possesses a volume of 150 x 10^6 $nm^3$and a

surface area of 7.5 x 10^6 nm^2, corresponding to a surface to volume ratio of 0.05 nm^{-1}. In turn, the milling of pores with diameter of D = 45 nm and center to center spacing of s = 120 nm reduces the volume of the beam to 140 x 10^6 nm^3, while augmenting its available capture surface to 8.38 x 10^6 nm^2. This corresponds to a new surface to volume ratio of 0.06 nm^{-1}, a 20% increase compared to the non-milled devices.

3.4 Conclusion

We have reported the use of helium ion milling for the post-fabrication modification of nanomechanical resonators. More precisely, arrays of pores were fabricated along the length of glassy nanostrings. This patterning resulted in a slight reduction of the resonant frequency of the devices, while increasing their surface to volume ratio. Helium ion milling could therefore be used for the post-fabrication tuning and trimming of nanomechanical resonators. This HIM milled porous nanostringis an alternative way to achieve small-mass compared with narrowing down the regular nanostrings. Without putting challenge to the limitation of EBL, this method opens a new route to enhance the sensitivity of nanomechanical string biosensors. Helium ion milling could therefore be used for the post-fabrication tuning and trimming of nanomechanical resonators. This post-fabrication method has the advantage of flexible and precise control over the dimension, locations and numbers of the milled patterns. Therefore, strings can be customized for target biochemical analytes.

Chapter 4 Diazonium functionalization of SiCN material

4.1 Introduction

4.1.1 Surface modification for biosensors

A biosensor is composed of a physical transducer, which converts biological analytes information into an output signal, and interfacial functional layers, which activates the interaction between the molecules of the sensor surface and environment [37], as shown in Fig. 4.1. Usually, the physical transducer determines the merits and limitations of the sensor detection. However, it is the functional layer that determines the selectivity and stability of the biosensor.

Before the nanostring can be used as a platform for biological sensing, the string surface needs to be bio-functionalized. Bio-functionalization is a technique for modifying material surface properties with biologically-relevant moieties. In general, the surface functionalization process of a biosensor is achieved in three steps as shown in Fig. 4.2 [129]. The first step is surface modification to produce chemical functional groups. The second step is to immobilize the probing agent by bio-conjugation to the functional groups. A third step is to passivate with blocking agent to avoid non-specific binding and guarantee the selectivity.

This surface modification, including the surface chemistry process and the immobilized bioactive molecules, are critical to the stability and selectivity of any biosensing system[130,131]. For a high

quality, stable and reliable biosensor, a robust bio-interface functional layer should have important properties such as strong adhesion to the substrate, control of density of functional groups and long term thermal, ambient and mechanical stability [131,132]. Biocompatibility is another desired property of surface modification, in which the chemistry process keeps both the substrate and environment natural and not disturbed. Foreign introduced toxic agents affect the interactions between analytes and the substrate which results in error of sensitivity and selectivity.

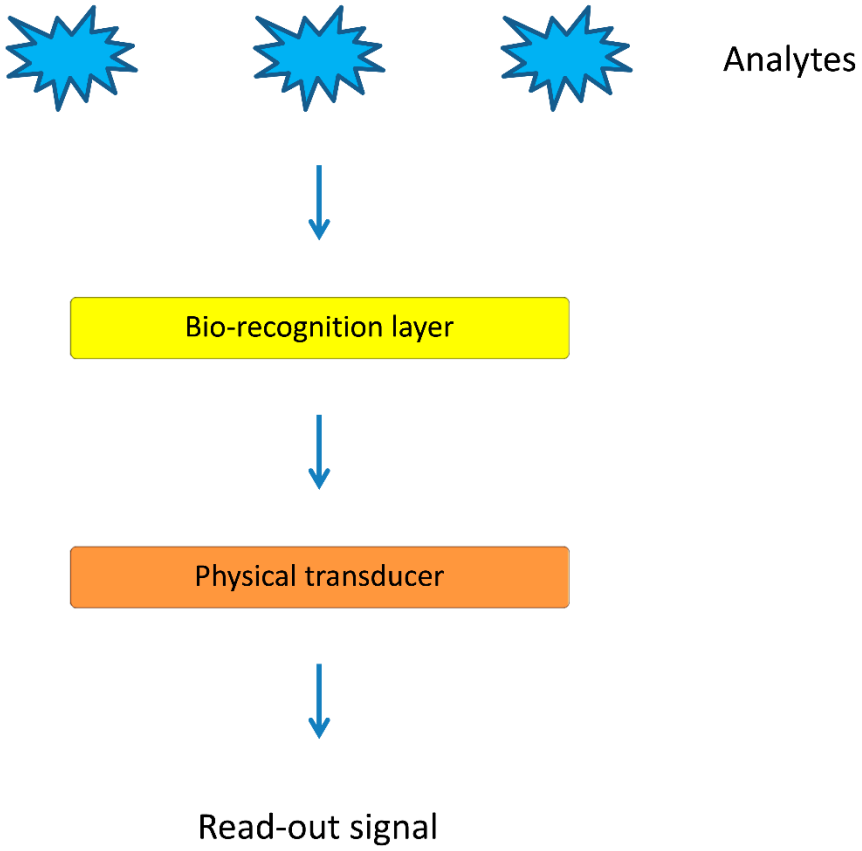

Fig. 4.1 Elements of a typical biosensor

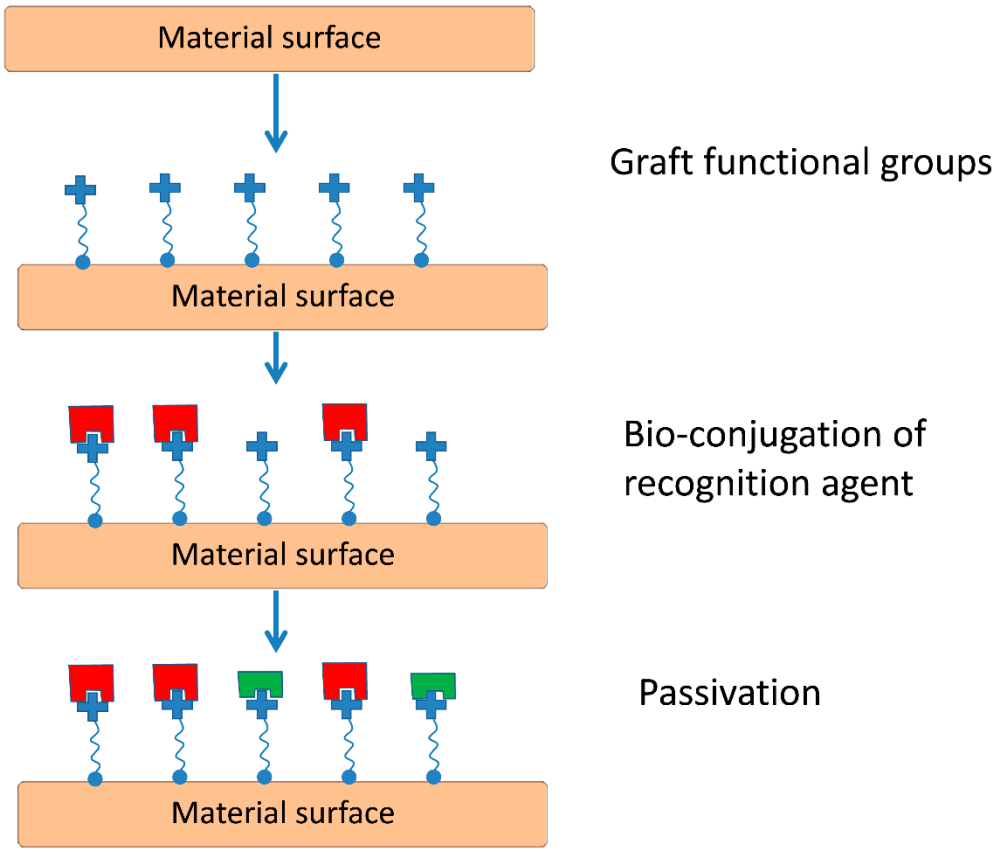

Fig. 4.2 General procedure of surface functionalization of a biosensor

4.1.2 General methods of surface modification

Various surface modification approaches enabling the anchoring of bio-active layers or sites have been explored in the past two decades. Depending on the mechanism of adhesion between material surfaces and the modification layer, they can be roughly divided to "physisorption" and "chemisorption" [133,134]. Physisorption is an adsorption process in which Van der Waals interactions cause intermolecular forces between the material surface and adsorbent while the

structure of the molecules and atoms remain minimally perturbed. Typical examples of physisorption methods, like spin coating and painting, suffers from rather fragile and short term adhesion. Hence physisorption is not suitable for practical bio functionalization application. Chemisorption, on the other hand, involves chemical reactions, forming chemical bonds between the surface of the substrate and organic polymers. Covalent bonding is preferred as it forms strong, stable and durable adhesion between the functional layer and substrate.

There are a number of methods for chemical surface modification. The most commonly used methods are thiol and silane self-assembled monolayers (SAM). Thiol monolayers do not provide covalent bonding but the interaction is strong and stable, especially on gold surface [135]. Surface modified by thiol chemistry has ordered alkaline monolayers. This unique property favors the specific binding between target molecules and sample surfaces while minimize the non-specific binding [136]. However, thiol SAM only works on metal surfaces. Organosilanes chemistry has the flexibility to form more defined quasi-crystalline monolayers on surfaces of inorganic materials, like silicon, glass, and metals. The method of silane monolayer has been intensively studied to apply to micro- and nanoscale devices, such as MEMS electronics and optics. Silane monolayers for surface functionalization has been demonstrated to immobilize antibodies for immunoassays on NEMS strings[137–139]. However, the siloxane bonds are subject to hydrolysis when heated or exposed to alkaline pH, which cause the instability of the self-assembled monolayer. Electrochemistry is another widely used surface modification technique. Bacause electrochemistry has good controllability, uses mild chemicals, and does not cause the material surface deformation or deterioration. However, electrochemistry is restricted to materials that are conductive or at least semi-conductive. Hence, a simple, mild, versatile and biocompatible chemistry process is imperative for surface modification.

4.1.3 Diazonium induced surface modification

Recently, a versatile diazonium salt reduction-induced aryl film grafting process has been reported [133,135,140]. This diazonium chemistry process overcomes the drawbacks of traditional chemical surface modification methods and meets the requirements for ideal surface modification as mentioned above.

In this process a thin film is covalently grafted to the substrate by chemical reduction of diazonium salts induced by reducing agents. This one-step redox process is readily implemented in aqueous environments, at room temperature, atmospheric pressure, ambient pressure and does not have the requirement of sophisticated equipment. These mild processing conditions preserve the nature of the substrate and biological environment to optimize the biocompatibility. As with other types of chemical absorption, diazonium chemistry forms true chemical bonding on the material surface, which has high thermal, mechanical and ambient stability over long time periods. After being immersed in organic solvents with ultrasonic treatments, bonding between the substrate and grafted film demonstrated robust stability [140]. The thickness of diazonium-derived aryl layers is controllable and thus the density of functional groups are controllable and can be customized to the target samples [141,142]. Moreover, this chemistry modification is applicable to all types of materials.

Due to these properties, diazonium chemistry is promising as universal surface modification method for the bio functionalization of biosensors. Significant research involving diazonium-induced surface modification of biosensors has been conducted in recent years [132,142–149]. Most of these reports were however limited to electrochemical sensors and surfaces such as carbon and metals.

As stated in the Chapter 2, the unique property of SiCN makes it an optimal material for fabricating ultra-small nanowire NEMS. Hence, the stability and selectivity of SiCN NEMS biosensors rely on the quality of surface functionalization of the SiCN material. Electrochemistry, the most frequently used method, does not apply to this non-conductive material. The silane monolayer method does not form stable chemical bonds and results in inaccuracy and low repeatability of measurement. The diazonium induced surface modification process is advantageous compared to other types of chemisorption techniques in this scenario, which makes it a perfect candidate for bio-functionalization of SiCN material. An additional benefit of the diazonium chemistry is that the aryl film is homogenous and the thickness of the organic layer is controllable from tens to hundreds of nm. As stated in the previous section, the small mass of the string favors higher detection sensitivity. The ultra-thin organic layer does not add on significant mass and, if controllable accurately, does not reduce the detection sensitivity.

The investigation of functionalization of glassy SiCN material has significant impact to the entire group of glassy materials based biosensors, like the fiber-optics based biosensor.

4.1.4 Methods of surface characterization

In a surface functionalization process, after each step of surface modification and immobilization of biological reagents, the attachment of polymer and analytes needs to be verified by surface characterization. Non-spectroscopy surface characterization methods, like Zeta potential, water contact angle, and dye assays, are simple, rapid, and common because of their low cost and simple manipulation. These techniques obtain qualitative measurement results in a timely way but each technique is confined to certain types of sample and is not applicable universally. Additionally, they pose a challenge when precise and qualitative assessment is required. On the other hand, the

most commonly used surface characterization methods are spectroscopy and microscopy, which provide precise analysis of elementary composition, functional groups, chemical bonding, morphology, and topography of the top several nanometers of the sample surface. Typical surface characterization tools are X-ray photoelectron spectroscopy (XPS), time-of-flight secondary ion mass spectrometry (ToF-SIMS), Fourier transform infrared spectroscopy (FTIR), Auger electron spectroscopy, scanning electron microscopy (SEM), energy-dispersive X-ray spectroscopy (EDX), transmission electron microscopy (TEM) and atomic force microscopy (AFM). The majority of these tools requires vacuum and relatively long operation time. Thus, the analysis results may contain inevitable errors in the case that the functional group or the chemical bonding between the polymer and substrate is unstable, hyperactive, or sensitive to ambient. In circumstances where real time monitoring of bioactivity is required, these spectroscopy and microscopy tools are not suitable because of significant data acquisition time delay. These methods have instrumental limitations due to their working mechanism, like restriction to certain dimensional resolution and insensitivity to particular elements. In addition, the tools are expensive and require high maintenance. However, comprehensive and accurate information of the sample surface can be obtained by combination of surface analysis from complementary tools.

XPS, also named as electron spectroscopy for chemical analysis (ESCA), is a frequently used quantitative measurement technique. It supplies comprehensive and informative chemical analysis. Full elemental composition as well as chemical bonding of the material within a surface depth ofup to 10 nm can be obtained. Various types of materials, including semiconductors, polymers, bio-materials, inorganic compounds, and metal alloys, can be precisely analyzed by XPS. However, XPS is not able to detect elements with an atomic number less than 3 or, in another words, hydrogen and helium.

The basic physics principle of XPS is the photoelectric effect phenomenon discovered by Albert Einstein in 1905 which won the Nobel Prize in 1921 [150]. K. Siegbahn initiated photoemission as an analytical tool, now known as XPS, in the 1960s, and won the Nobel Prize for Physics in 1981. As shown in Fig. 4.3, the configuration of a XPS instrument includes an X-ray source, an electron detector, an electron energy analyzer, an electron collection lens and an ultra-high vacuum (UHV) chamber. The photons generated by the X-ray source collide with electrons in different atomic orbitals on the surface of the sample. The electrons gain the energy to escape from the binding energy of the atomic nucleus and are collected by the electron collection lens. The electron energy analyzer measures the kinetic energy of ejected electrons and the electron detector system counts the electrons. The kinetic energy of electrons is determined by the energy of the photons ($h\nu$), the binding energy of electrons ($B.E_{.F}$), and work function (ϕ_{sample}), as shown in Equation 4.1.

$$K.E = h\nu - B.E_{.F} - \phi_{sample} \tag{4.1}$$

The binding energy is obtained based on the calculation of kinetic energy of the electrons as shown in Equation 4.2 [151].

$$B.E_{.F} = h\nu - K.E - \phi_{sample} \tag{4.2}$$

XPS is the primary characterization instrument for surface analysis of biomedical samples and polymers. In this chapter, XPS is used to characterize the surface of diazonium modified material surfaces.

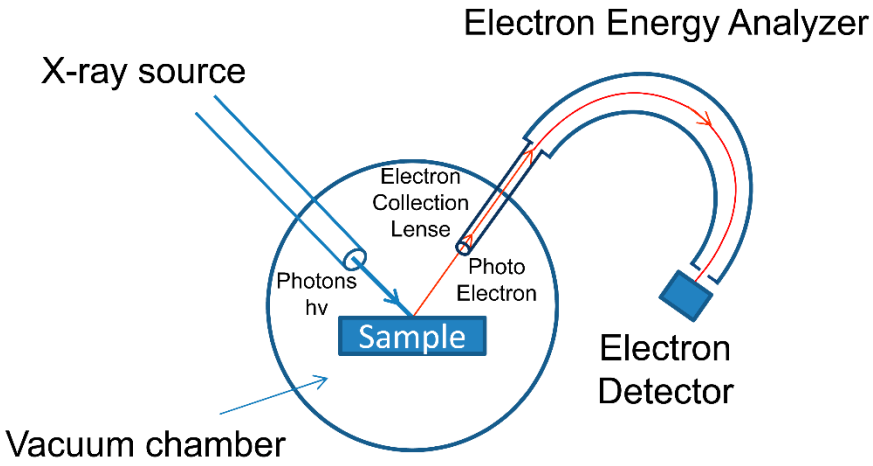

Fig. 4.3 Configuration of XPS

4.1.5 Structure of this chapter

Fig. 4.4 shows the structure of this chapter. Before applying the diazonium induced polymer grafting process as the surface modification method to functionalize the SiCN NEMS sensor, verification of the diazonium chemistry with SiCN itself was needed. Therefore, in this chapter [152], first the SiCN surface was modified by the diazonium salt induced aryl film grafting process and characterized with XPS. After the validation of XPS spectrum analysis, sandwich immunoassay was performed on the diazonium treated SiCN surface. As the most commonly used bio-conjugation strategy, carboxylic acid group terminated aryl diazonium salt was adopted as the surface modification reagent. The carboxylic acid group easily reacts with the amino group in the antibody and forms the covalent amide bond. Due to the high specific affinity of primary and secondary antibodies, typical rabbit

IgG and anti-rabbit IgG are chosen as the probe protein and target protein, respectively. FITC labelled anti-rabbit IgG and AuNP conjugated anti-rabbit IgG were used individually as markers to visually inspect the absorption of anti-rabbit IgG to the substrate. In each case, confocal microscopy and SEM microscopy were individually used for characterization of the sample and control. The conclusion of these experiments is critical for the feasibility of diazonium modification of SiCN NEMS sensors. To the best of our knowledge, this work is the first exploration of taking diazonium salt as a linker chemistry to modify the SiCN material surface as well as the first application of diazonium chemistry to functionalize nanostring-based NEMS biosensors.

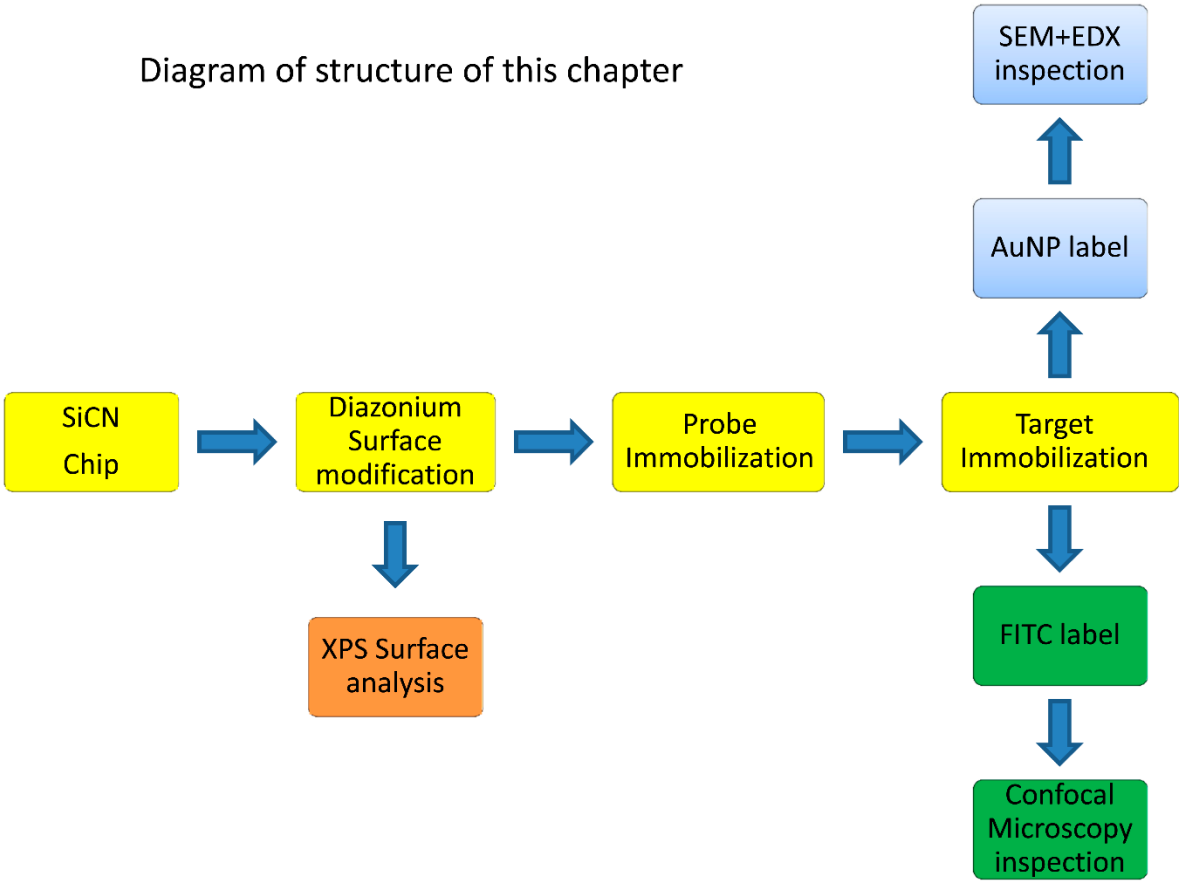

Fig. 4.4 Diagram of structure of chapter 4

4.2 Experiment

4.2.1 Synthesis of aryl diazonium salt

Diazonium salts were prepared from the corresponding anilines using a previously published method [153]. Briefly, the appropriate aniline (4-bromoaniline or 4-aminobenzoic acid, 0.1 moles, Sigma-Aldrich) was dissolved in fluoroboric acid (48%, 50 ml, Sigma-Aldrich) and then cooled in an ice water bath. After cooling to 0°C, sodium nitrite (10 g, Sigma-Aldrich) dissolved in DI water (20 ml) was added drop by drop while stirring. The reaction mixture was further cooled in an ice water bath and stirred for another 1 h. The resultant precipitate was filtered in a Buchner funnel and washed with cold anhydrous ether (Sigma-Aldrich).

4.2.2 Diazonium induced SiCN surface modification

The diazonium salt induced polymer grafting chemistry process as reported in [140]was employed to modify the SiCN material. This surface modification process was performed in an aqueous environment at atmospheric pressure and at room temperature. The modified SiCN surfaces were analyzed by XPS to verify the bonding between the grafted layer and the SiCN thin film.

As the initial verification step, diazonium salt 4-bromobenzenediazonium tetrafluoroborate ($Br\text{-}C_6H_4\text{-}N_2BF_4$) was selected as the reactant because the element Br does not exist in the material surface or ambient but only exist in the final product. If Br signal was detected in the modified SiCN surface by XPS analysis, it verifies the attachment of aryl film to substrate. Thus, Br serves as a marker element for easy subsequent XPS assessment.

4-carboxy benzenediazonium tetrafluoroborate (COOH-C_6H_4-N_2BF_4) is employed to bio-functionalize the SiCN sensor surfaces, because the carboxyl group (-COOH) is commonly leveraged for bio-conjugation. However, the compositional elements of this group, carbon and oxygen, also exist in the SiCN substrate. A carboxyl group bonding to SiCN is able to be analyzed by XPS but the analysis is more complicated than that of the Br group. For this reason, Br-benzene diazonium salt was first used for initial surface modification test and simpler XPS analysis. Once the process was validated by XPS, the SiCN chips were bio-functionalized by 4-carboxy benzenediazonium tetrafluoroborate (Fig. 4.5).

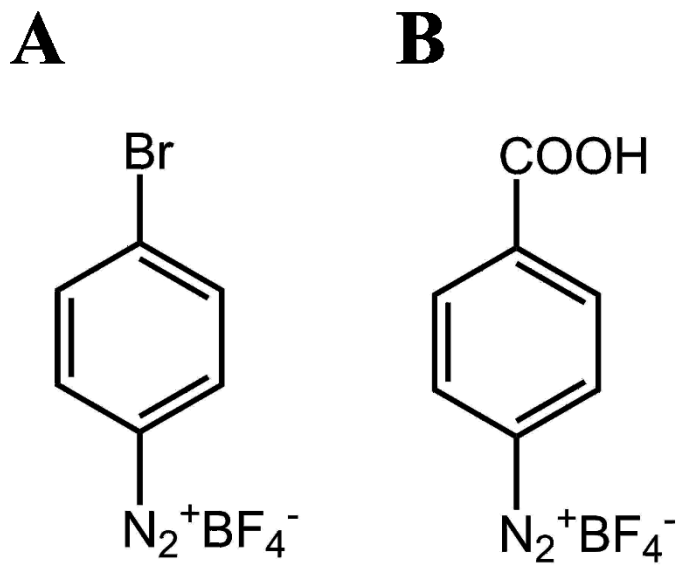

Fig. 4.5 Molecule structures of (A) 4-bromobenzenediazonium tetrafluoroborate and (B) 4-carboxy benzenediazonium tetrafluoroborate

L-ascorbic acid (VC) was selected as the reducing agent. Two identical SiCN bare chips, one as the sample and the other as control, were cleaned in cold (<40 ℃) piranha (3:1 96% H_2SO_4: 30% H_2O_2) for 15 min and BOE (buffered oxide etch, 10:1 HF: NH_4F) for 3 min to eliminate organic contamination and possible oxidation on the SiCN surface. A 0.05M 4-bromobenzenediazonium tetrafluoroborate solution and a 0.05M L-ascorbic acid solution in Milli-Q water were individually prepared. A 2 mL 4-bromobenzenediazonium tetrafluoroborate solution was poured dropwise onto the SiCN sample chip. Further, 1 mL of L-ascorbic acid (VC) solution was added dropwise to the diazonium solution. The SiCN sample chip was left to incubate in the mixture while in a glass petri dish for 60 min at room temperature. The negative control experiment was carried in parallel by immersing the SiCN control chip into a 1 mL 0.05M L-ascorbic acid (VC) solution, without any 4-bromobenzenediazonium tetrafluoroborate, for 60 min. The sample and control chips were then individually rinsed in water, ethanol, acetone, sonicated in dimethyl formamide (DMF) for 5 min, and dried under nitrogen flow.

4.2.3 XPS surface analysis

The surface of SiCN sample and control was analyzed by XPS. The XPS measurements were performed on a Kratos AXIS ULTRA spectrometer using a monochromatic Al Kα source (hν=1486.6 eV) at a power of 170 W and 90° take-off angle (TOA). The data was collected from an analysis area of 400 μm x 700 μm. The instrument base pressure was lower than 5 x 10^{-8} Pa. The resolution was 0.55 eV for Ag 3*d* and 0.70 eV for Au 4*f* peaks. The survey scans and the high-resolution spectra were carried out with a pass energy of 160 eV and 20 eV, respectively. For Br, 50 X high resolution scans were run with a step of 0.1 eV. An electron flood gun was used for charge neutralization. Data were calibrated by

setting the main C 1s component at 284.8 eV. Vision-2 instrument software was employed for data acquisition and CasaXPS was used for its processing.

4.2.4 Sandwich rabbit IgG assay

The whole strategy of Rabbit IgG antibody and rabbit IgG immobilization on SiCN sensor surface is described in Figure 4.6.

4.2.4.1 AuNP (Gold Nanoparticle) labelled sandwich rabbit IgG assay

4.2.4.1.1 Diazonium surface modification

First, SiCN chips were surface modified using 4-carboxybenzenediazonium tetrafluoroborate ($C_7H_5BF_4N_2O_2$) as a reactant. As opposed to 4-bromobenzenediazonium tetrafluoroborate, 4-carboxybenzenediazonium tetrafluoroborate supplies an active carboxylic acid group as a chemical active group to bind to the proteins The procedure was the same as the one described in section 4.2.2, except 4-bromobenzenediazonium tetrafluoroborate was replaced by 4-carboxybenzenediazonium tetrafluoroborate. Four SiCN chips (A1, B1, C1, D1) were pre-treated with the same cleaning procedure and incubated in the mixture of 0.05M 4-carboxybenzenediazonium tetrafluoroborate and 0.05M L-ascorbic acid, with a 2:1 volume ratio, for 60 min. The chips were then rinsed in water, ethanol, acetone, sonicated in DMF and nitrogen dried.

4.2.4.1.2 Activation of carboxyl groups

Fresh 0.4M EDC (N-(3-dimethylaminopropyl)-N′-ethylcarbodiimide hydrochloride) solution and 0.1M NHS (N-hydroxysuccinimide) solutions were made and mixed together in a 1:1 volume ratio. The four carboxyl-bearing SiCN chips were incubated in the mixture

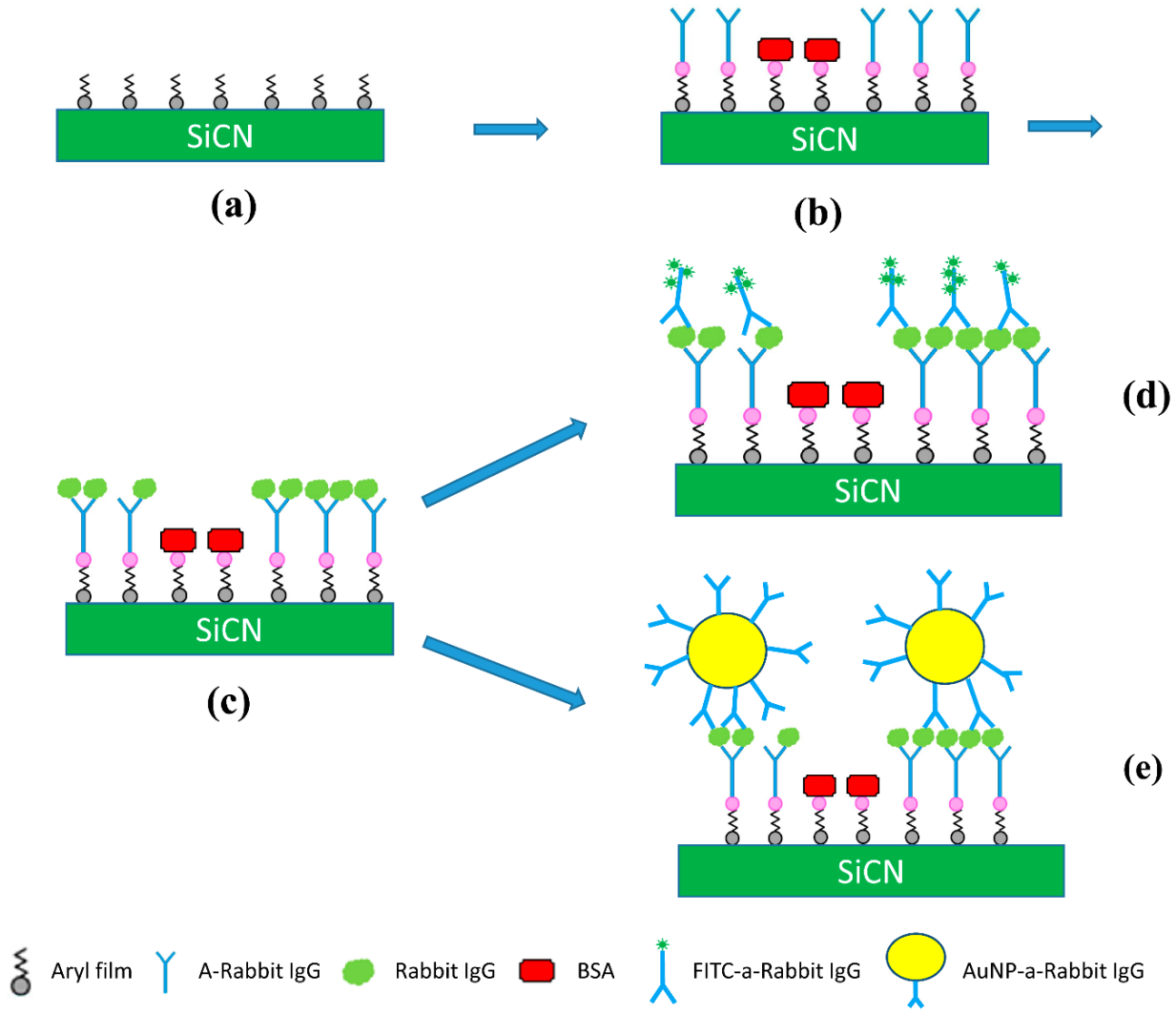

Fig. 4.6 Sandwich assay using FITC and AuNP as labels: (a) SiCN surface modification by aryl diazonium salt; (b) Bio-conjugation of recognition probe to aryl layer; (c) Rabbit IgG binds to rabbit IgG antibody; (d) FITC-a-rabbit IgG immobilization to rabbit IgG; (e)AuNP-a-rabbit IgG immobilization to rabbit IgG

for 30 min at room temperature. After this reaction time, the chips were rinsed and blow-dried in nitrogen.

In this AuNP labelled sandwich rabbit IgG assay, due to their high mutual specificity and affinity anti-rabbit IgG was selected as the recognition bioreceptor, while rabbit IgG was used as the target. AuNP conjugated anti-rabbit IgG was adopted as the detection marker.

4.2.4.1.3 Immobilization of recognition bioreceptor

The four SiCN chips baring activated carboxyl groups were incubated in 100µg/ml goat anti-rabbit IgG solution (polyclonal, Sigma-Aldrich) at room temperature for 2 h. The chips were rinsed with PBST (Phosphate Buffered Saline Tween-20) and then incubated in 5% BSA (bovine serum albumin) at room temperature for 1 h to block the non-specific binding sites. After that, the chips were rinsed in PBST.

4.2.4.1.4 Immobilization of target

Two chips (A1 and B1) were immobilized with the detection target by incubating in 200µg/ml rabbit IgG solution (polyclonal, Sigma-Aldrich) at room temperature for 1 h. In parallel, as a control, the other two chips (C1 and D1) were incubated in 200µg/ml goat IgG solution (polyclonal, Sigma-Aldrich) at room temperature for 1 h. After that, the chips were rinsed in PBST.

4.2.4.1.5 Immobilization of detection marker:

Chips A1 and C1 were immersed in 40nm AuNP (4.5 x 1011/ml) conjugated anti-rabbit IgG solution (10µg/ml, Ted Pella) at room temperature for 1 h. Chips B1 and D1 were immersed in 1:3

diluted solution of 40nm AuNP conjugated anti-rabbit IgG at room temperature for 1 h. After incubation, the chips were water rinsed and nitrogen dried.

4.2.4.2 SEM and EDX

A high resolution field emission scanning electron microscopy (Zeiss Sigma FE-SEM) was used to detect the presence of the gold nanoparticles immobilized on the surface of chips A1, B1, C1 and D1. Images were obtained at magnification from 10 000x up to 200 000x under an acceleration voltage of 15 kV by using secondary electron (SE) in-lens and backscattered electron (BSE) detector.

An energy-dispersive X-ray detection instrument (EDX) was used to identify the elemental composition of the surfaces of chips A1, B1, C1 and D1. An Oxford Instruments X-Max^N 150mm^2 Silicon Drift Detector (SDD) detector was used for point analysis and mapping of elemental spatial distributions.

4.2.4.3 FITC labelled sandwich rabbit IgG assay

The FITC labelled sandwich rabbit IgG assay was similar to the AuNP labelled sandwich rabbit IgG assay except that FITC conjugated anti-rabbit IgG was used as the detection marker.

Four SiCN chips (A2, B2, C2, D2) were surface modified with carboxyl group by diazonium chemistry and activated by EDC and NHS mixture with the same procedure as stated in section 4.2.4.1. The method for immobilization of the bioreceptor and target is similar to that shown in section 4.2.4.1. Briefly, the four chips (A2, B2, C2, D2) were incubated in 100µg/ml goat anti-rabbit IgG solution (polyclonal, Sigma-Aldrich) for 2 h and 5% BSA (bovine serum albumin) for 1 h at room temperature in consequence. Chips A2 and B2 were incubated in 200µg/ml rabbit IgG

solution (polyclonal, Sigma-Aldrich) for 1 h whereas chips C2 and D2 were subject to 200 µg/ml goat IgG solution (polyclonal, Sigma-Aldrich) as a control for 1 h at room temperature, respectively.

Chips A2 and C2 were immersed in 1:200 diluted FITC conjugated anti-rabbit IgG solution (Sigma-Aldrich) while Chips B2 and D2 were immersed in 1:400 diluted FITC conjugated anti-rabbit IgG solution at room temperature for 1 h respectively.

4.2.4.4 Confocal microscopy imaging

Chips A2, B2, C2, D2 were individually imaged on a Zeiss LSM 710 Laser scanning confocal microscope mounted on an Axio-observer inverted microscope (ZEN 2011, Jena, Germany) with a plan Apochromat 20x (NA 0.8) lens. Fluorescence signal was collected with a 488nm laser excitation and with an emission wavelength range of 492nm-590nm. Images were digitized at 16 bit with a Nyquist sampling rate using a pinhole size of one airy unit.

The above mentioned positive samples and negative controls for AuNP and FITC labelled sandwich rabbit IgG assay are summarized in Table 4.1.

Table 4.1 Description of Samples

Sample	Control type	Dilution ratio	Label
A1	positive	1:1	AuNP
B1	positive	1:3	AuNP
C1	negative	1:1	AuNP
D1	negative	1:3	AuNP
A2	positive	1:200	FITC
B2	positive	1:400	FITC
C2	negative	1:200	FITC
D2	negative	1:400	FITC

4.3 Results and Discussion

4.3.1 One-step modification of the SiCN surface

The SiCN surfaces have been modified in one simple step of redox reaction in an aqueous environment, at ambient pressure and room temperature. The mechanism of aryl diazonium salt induced surface modification is due to the dediazonation caused by one electron reduction and the creation of free aryl radical [133,140,143]. In the case of the SiCN surface modification described here, shown in Fig. 4.7 (A) and (B), the aryl diazonium salt is reduced by L-ascorbic acid, and the free aryl radical forms strong chemical bonds to the SiCN surface atoms.

The SiCN sample modified by 4-bromobenzene diazonium tetrafluoroborate and the negative control were surface analyzed by XPS. Bromine was used as the marker element to indicate if aryl films were successfully grafted on the sample surfaces. Bromine is indeed a component of the aromatic ring but not a component of the pristine samples. The XPS high resolution spectra, as shown in Fig. 4.7 (C) and (D), exhibited a significant peak at 71 eV which are attributed to the Br 3*d*5/2 signal. Presence of such Br peak thus confirmed the bonding of the aromatic ring to the substrate. Because the SiCN was sonicated in dimethyl formamide (DMF) for 5 min after surface modification. Physisorption on the SiCN chip were removed by the vigorous ultrasonication. Hence, the bonding between aromatic ring and the substrate was due to strong chemical adhesion. It is already proven in literature that aryl film forms covalent bonding on the surfaces of carbon, silicon and gold [135,143,154–156]. Therefore, it is reasonable to assume that the aromatic ring formed covalent bonding to the SiCN substrate. The high resolution spectrum from the negative

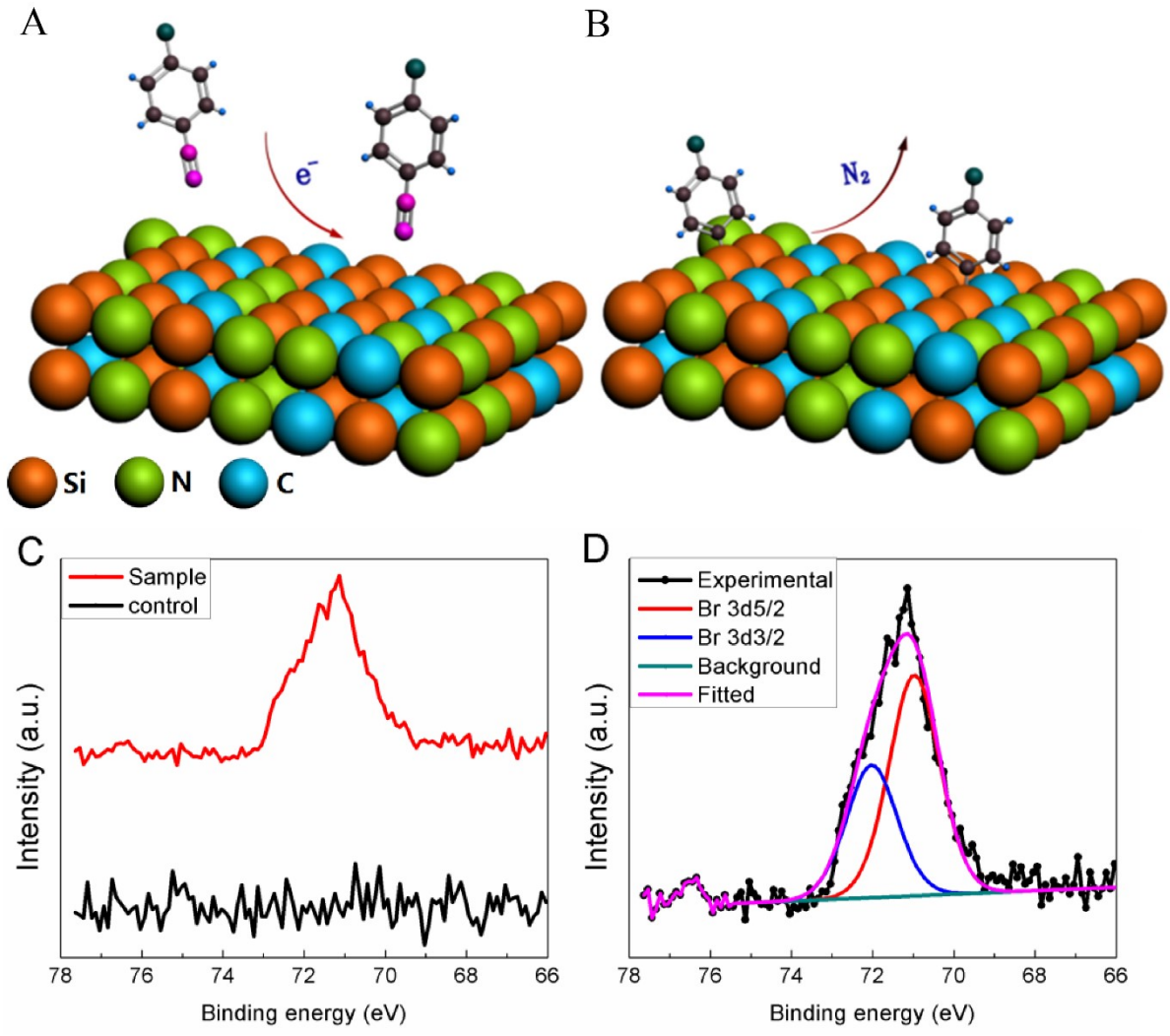

Fig. 4.7 Reaction mechanism and XPS analysis of aryl diazonium modification of SiCN surface: (a) Aryl diazonium salt reduction by electrons; (b) the created free aryl radicals strongly bond to the SiCN surface; (c) XPS high resolution scans of Br element spectra on aryl diazonium modified SiCN sample and control surfaces; (d)XPS experimental bromine spectrum and theoretical Br 3d fitted curves.

control sample is below the noise level and does not show any peak at this range. The results demonstrate the successful modification of SiCN surfaces by aryl diazonium salt and confirm the formation and grafting of aryl films on the modified SiCN surface.

4-carboxy benzenediazonium tetrafluoroborate was employed to bio-functionalize the SiCN sensor surfaces, as the carboxyl group (-COOH) is commonly employed for bio-conjugation. However, the compositional elements of this group, carbon and oxygen, also exist in the SiCN substrate. For this reason, Br-benzene diaznonium salt was first used for initial surface modification tests and XPS analysis. Once the process was validated by XPS, the SiCN chips were bio-functionalized by 4-carboxy benzenediazonium tetrafluoroborate.

The mechanism of 4-carboxy benzenediazonium tetrafluoroborate reduction induced aromatic ring grafting on the SiCN substrate is the same with that of 4-bromobenzene diazonium tetrafluoroborate. As shown in Fig. 4.8, by one electron reduction, the diazo group is lost from 4-carboxy benzenediazonium tetrafluoroborate and the aryl radical bearing carboxyl group is produced (R1). This active aryl radical strongly bonds to the SiCN and thus the surface is modified with carboxyl group (R2). In case of large availability of reducing agent or prolonged exposure time, further reduction happens and produces abundant aryl radicals. These radicals either fill the space on the SiCN surface to form a monolayer or bond to the aromatic rings, which are already on the SiCN surface, to form multilayers (R3 and R4).

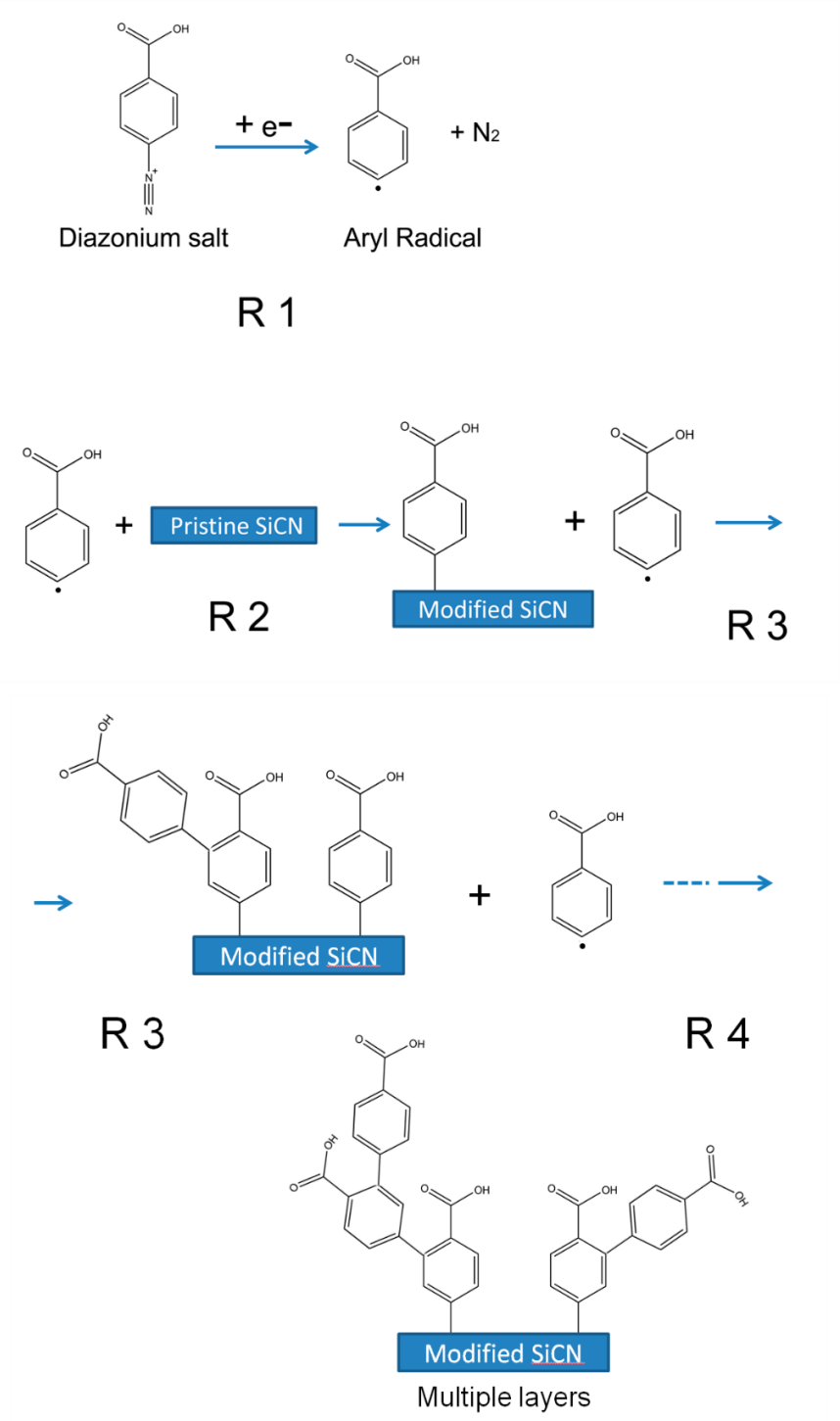

Fig. 4.8 Mechanism of diazonium reduction induced monolayer and multilayer of carboxyl group grafting on SiCN surface

The carboxyl group introduced onto the SiCN surface enabled the covalent immobilization of proteins by formation of an amide bond between proteins and the surface. EDC/NHS, the molecule structures of which are depicted in Fig. 4.9, was used to activate the carboxyl groups. The carboxylic acid group was converted to carboxyl-NHS ester using EDC as an intermediate. The NHS ester reacts with the primary amine in proteins and forms an amide bond. This mechanism is illustrated in Fig. 4.10. This strategy was thus employed to covalently bind anti-rabbit IgG onto the nanostrings.

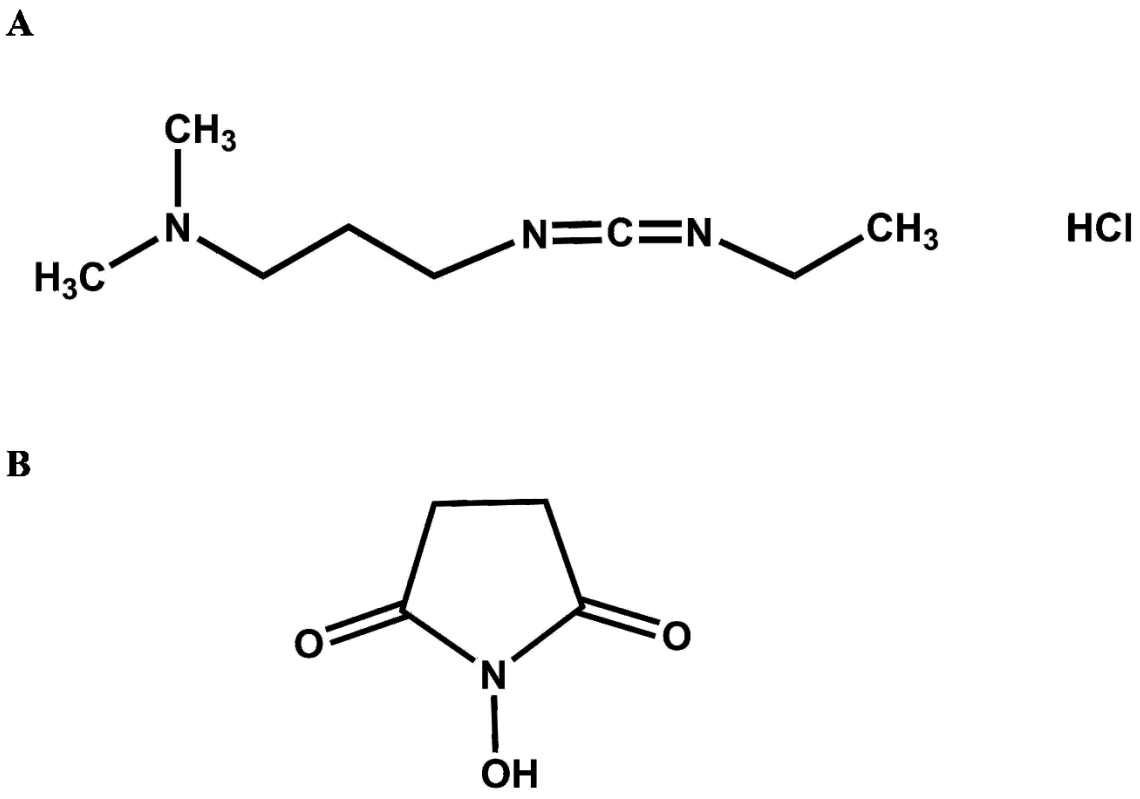

Fig. 4.9 The molecule structures of (A) EDC and (B) NHS.

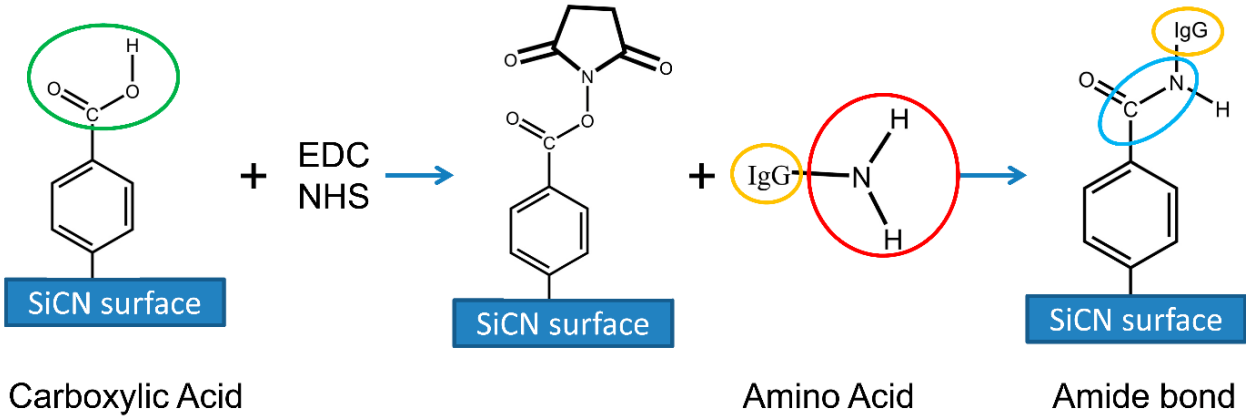

Fig. 4.10 Mechanism of carboxyl group activation via EDC/NHS and amide bond formation from carboxyl group and amino group

4.3.2. SEM and EDX of AuNP

As shown in Fig. 4.6, after immobilization of aryl molecule baring carboxylic acid group and activation of these carboxyl groups by EDC and NHS, the anti-rabbit IgG were immobilized to the SiCN chips as recognition reagent by covalent bonding. BSA, the most frequently used blocking protein, was used to prevent non-specific binding sites on the SiCN surface. Next, the detection target rabbit IgG were immobilized due to the affinity between anti-rabbit IgG and rabbit IgG. At the last step, anti-rabbit IgG labelled with AuNP and FITC were individually immobilized due to the affinity between anti-rabbit IgG and rabbit IgG. Therefore, if the labels AuNP and FITC are detected under microscopy, it proves the adsorption of the target molecule rabbit IgG on the SiCN chips.

As a control, the SiCN chips baring anti-rabbit IgG and passivated with BSA was subject to non-specific target goat IgG solution and then anti-rabbit IgG labelled with AuNP and FITC. It is known that goat IgG does not have specific bonding with anti-rabbit IgG. Therefore, if no label signal were observed under microscopy, it indicated the goat IgG does not exist on the SiCN chips. Hence, the presence of labels in sample surfaces and non-presence of labels in control surfaces could verify the specific detection.

Fig. 4.11 shows the SEM images of AuNP distribution on sample chip A1 and control chip C1. Obviously, the chip A1 has a dense and roughly uniform AuNP distribution over the random area under low magnifications of 10 000x and 20 000x, respectively. Almost no AuNP was observed on control chip C1. It is noticeable that these results were obtained under the condition that AuNP conjugated anti-rabbit IgG was in stock high concentration. To exclude the possibility of non-specific binding by saturation, a 1:3 diluted AuNP conjugated anti-rabbit IgG was applied on sample chip B1 and control chip D1. The results are shown in Fig. 4.12. B1 has roughly uniform coverage of AuNP but at a lower density of distribution compared to that of A1. Very small amount of AuNP sparsely appears on chip D1 under magnification of 10 000x, meaning tiny amount of non-specific binding of AuNP to substrate. This is possibly due to the interaction between polyclonal goat anti-rabbit IgG and goat IgG. The interaction of AuNP itself to the IgG molecules on the substrate maybe another reason. No AuNP are shown under magnification of 20 000x. The contrast of AuNP density between samples and controls in Fig.11 and Fig.12 concludes the selective binding of AuNP conjugated rabbit IgG to substrate.

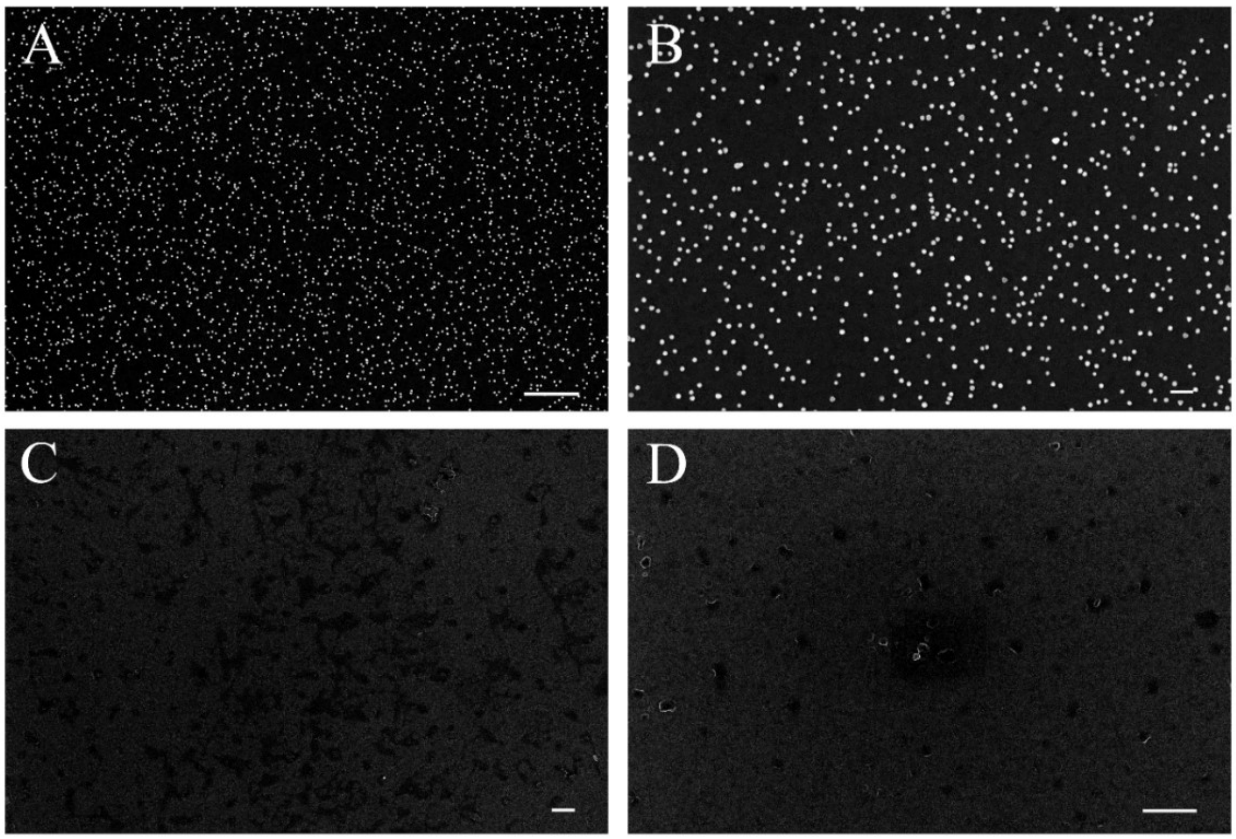

Fig. 4.11. Comparison of presence of AuNP on the surface of sample chip A1 and control chip C1: (A) AuNP distribution on chip A1 under 10 000 times magnification, scale bar stands for 1μm; (B) AuNP distribution on chip A1 under 20 000 times magnification, scale bar stands for 200nm; (C) AuNP distribution on chip C1 under 10 000 times magnification, scale bar stands for 1μm; (D) AuNP distribution on chip C1 under 20 000 times magnification, scale bar stands for 200nm.

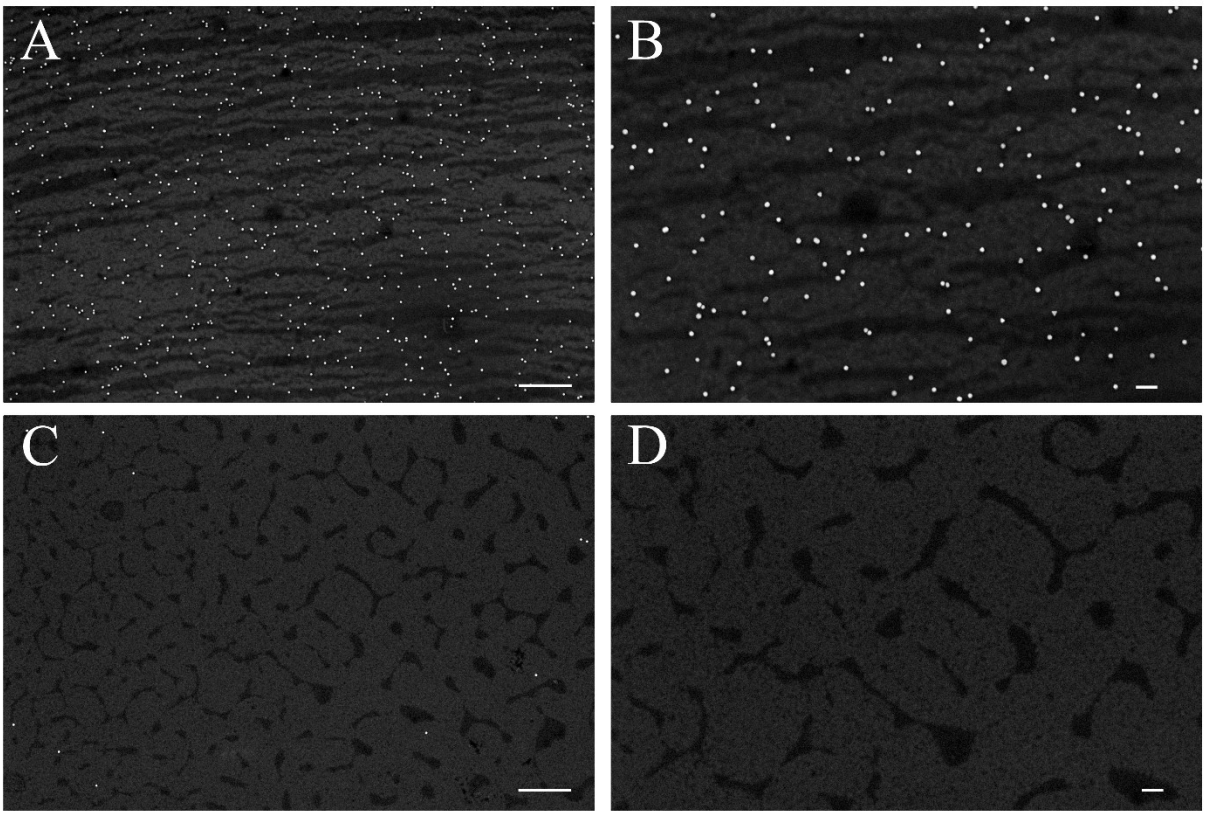

Fig. 4.12 Comparison of presence of AuNP on the surface of sample chip B1 and control chip D1: (A) AuNP distribution on chip B1 under 10 000 times magnification, scale bar stands for 1μm; (B) AuNP distribution on chip B1 under 20 000 times magnification, scale bar stands for 200nm; (C) AuNP distribution on chip D1 under 10 000 times magnification, scale bar stands for 1μm; (D) AuNP distribution on chip D1 under 20 000 times magnification, scale bar stands for 200nm.

Fig. 4.13 compares the density of AuNP on chips A1 and B1. Under 50 000x and 200 000x magnification, the ratio of AuNP of A1 to B1 is around 3:1 which is linear to the concentration of AuNP conjugated rabbit IgG. Under 100 000x magnification, the ratio of AuNP of A1 to B1 is around 2:1.

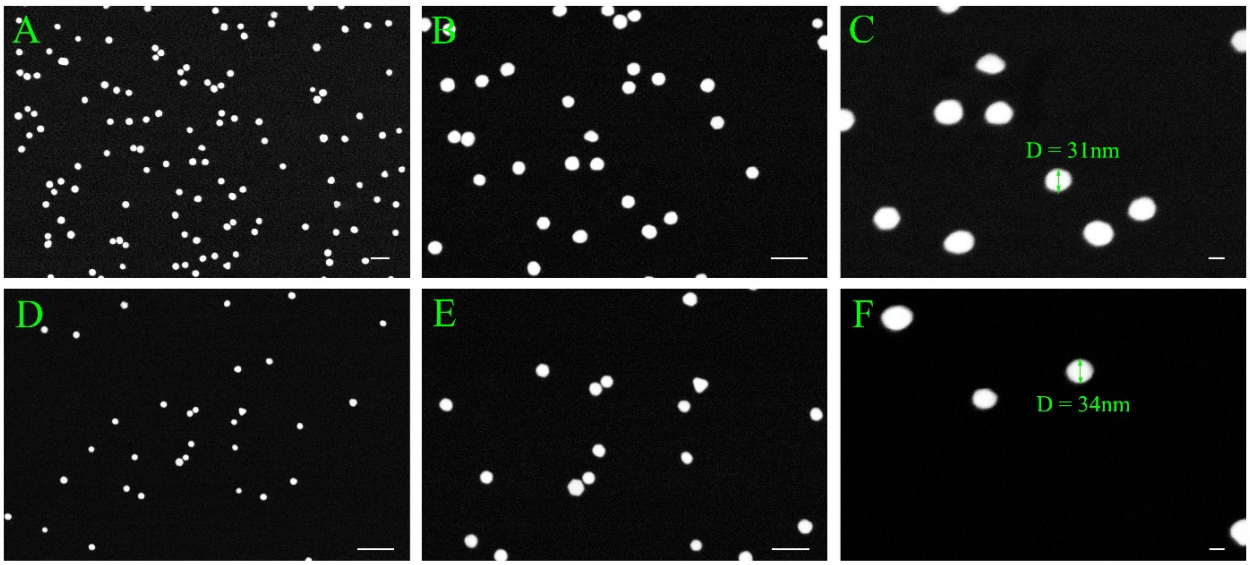

Fig. 4.13 Comparison of presence and density of AuNP on the surface of chips A1 and B1 under high magnification: (A) AuNP distribution on chip A1 under 50 000 times magnification, scale bar stands for 100nm; (B) AuNP distribution on chip A1 under 100 000 times magnification, scale bar stands for 100nm; (C) AuNP distribution on chip A1 under 200 000 times magnification, scale bar stands for 20nm; (D) AuNP distribution on chip B1 under 50 000 times magnification, scale bar stands for 200nm; (E) AuNP distribution on chip B1 under 100 000 times magnification, scale bar stands for 100nm; (F) AuNP distribution on chip B1 under 200 000 times magnification, scale bar stands for 20nm.

The SEM result shown in Fig. 4.11, Fig. 4. 12 and Fig. 4.13 verifies the fact that target molecules are immobilized onto the probe molecules by specific binding. The immobilization of recognition molecules is based on covalent bonding between amino acid and bio-active group in the aromatic ring. Diazononium derived aryl film is an effective surface modification method for specific detection.

Fig. 4.14 is a supplementary proof in addition to the SEM images. This figure shows the EDX analysis of the SiCN substrate immobilized with a sandwich rabbit IgG structure. The point analysis of the particle (panel B) shows significant peaks for elements gold, silicon, carbon and nitrogen, which proves the attachment of AuNP onto the SiCN substrate. The elements map shows their relative proportions on and off the particle. As seen from Panel C, despite of background noise of sparse gold distribution off the particle, the contrast of gold density on and off particle is high enough to prove the existence of AuNP on surface. Panels D, E, and F show less silicon, a bit more carbon and almost the same amount of nitrogen on the particle, which agrees with the fact that AuNP conjugated anti-rabbit IgG molecules contains carbon and nitrogen but not silicon. The shapes of elements mapping are slightly distorted due to the electron astigmation at high magnification but they still reflect the concentrations of the elemental distributions effectively.

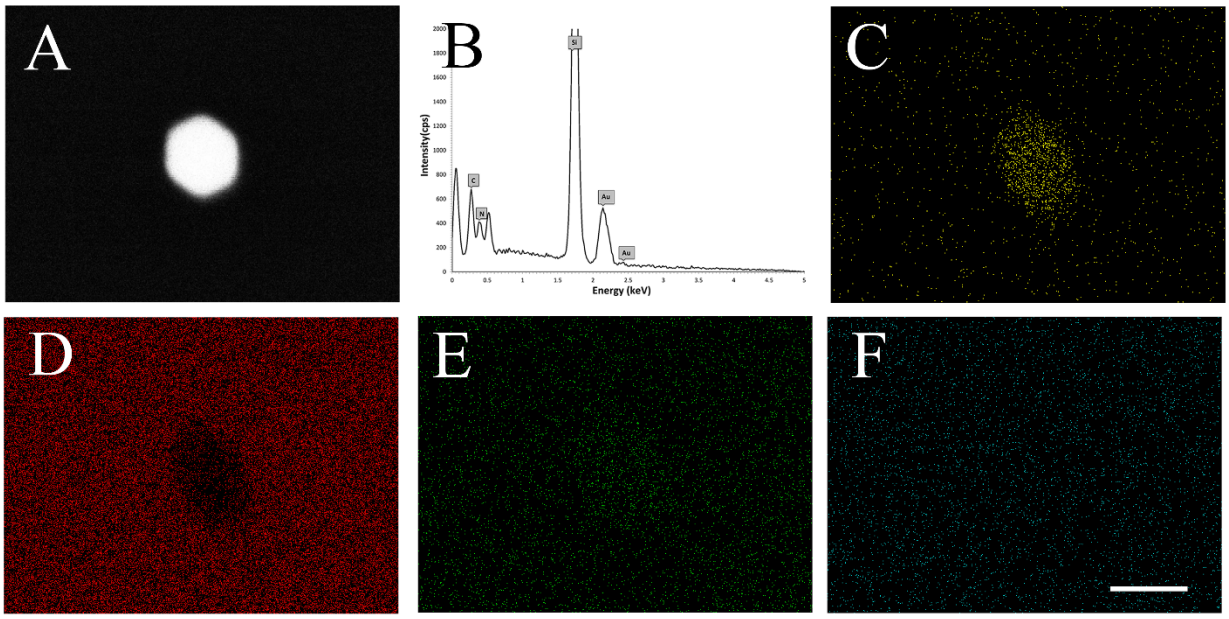

Fig. 4.14 EDX analysis of substrate immobilized with AuNP: (A) SEM image of AuNP; (B) EDX spectrum of a point of the particle, showing peaks of gold, silicon, carbon and nitrogen; (C) map of distribution and relative intensity of element gold in scanned area; (D) map of distribution and relative intensity of element silicon in scanned area; (E) map of distribution and relative intensity of element carbon in scanned area; (F) map of distribution and relative intensity of element nitrogen in scanned area. Scale bar stands for 50nm.

4.3.3. Fluorescent images of FITC

As seen in Fig. 4.15, FITC as a detection marker was present only in chips A2 and B2 but not in control chips C2 and D2. It is obvious that the FITC color in A2 is brighter than that of B2 while almost no visible color difference exists between C2 and D2.

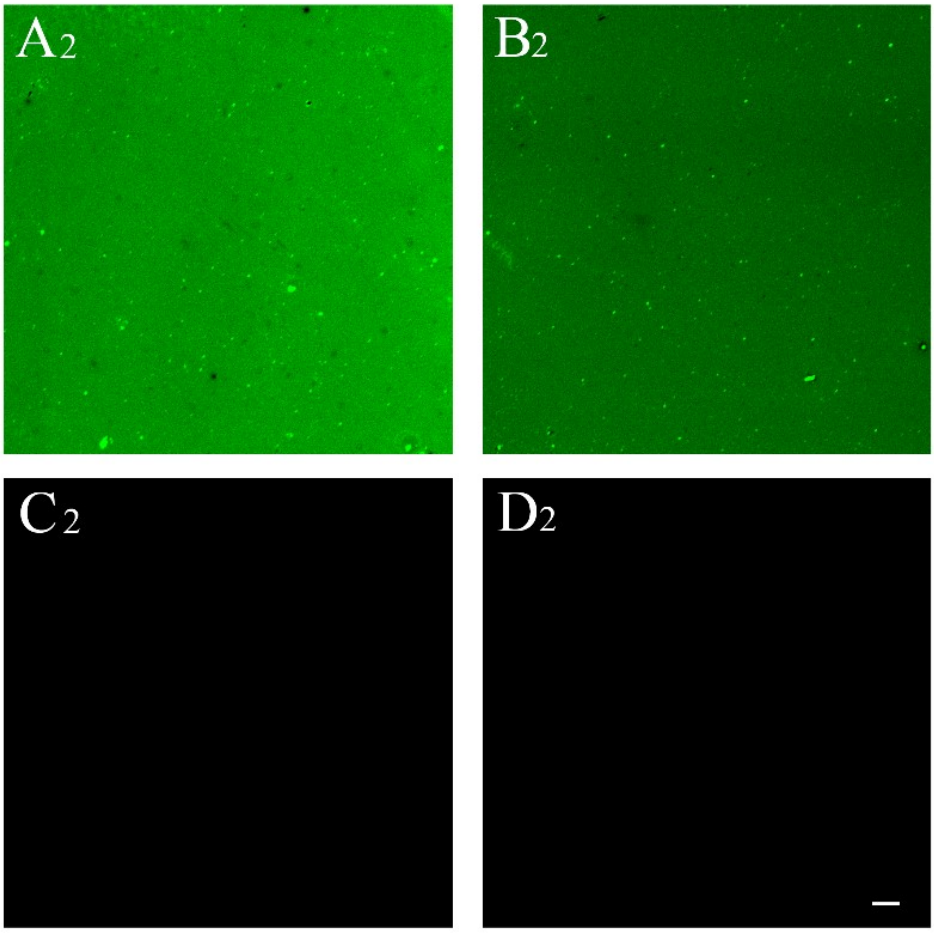

Fig. 4.15 Comparison of presence of FITC on the surface of sample chip A2, B2 and control chip C2, D2: (A) FITC distribution on chip A2; (B) FITC distribution on chip B2; (C) FITC distribution on chip C2; (D) FITC distribution on chip D2. Scale bar stands for 2um.

Table 4.2 Mean optical intensity of FITC on the surface of sample chips A2, B2 and control chips C2, D2

Sample	Intensity (AU)	Signal to Noise Ratio	Dilution Ratio of FITC Conjugated Anti-Rabbit IgG
A2	37,967	185	1:200
C2	205		
B2	25,791	105	1:400
D2	245		

To make quantitative comparison, Table 4.2 shows the mean optical intensity and the ratio of signal level compared to background noise. The signal to noise ratio of 185 and 105 under FITC dilution ratio of 1:200 and 1:400 respectively is high enough to prove the selective absorption of FITC conjugated anti-rabbit IgG to target molecule rabbit IgG. The optical intensity of A2 is 47% larger than that of B2, which means non-saturation binding of FITC conjugated anti-rabbit IgG to the substrate. The optical intensity of C2 and D2 are almost the same and does not differ with FITC concentration, which further verifies almost no non-specific binding of FITC conjugated anti-rabbit IgG to substrate. Hence, the chemical bonding of probe molecule anti-rabbit IgG to the aryl film on SiCN substrate induced by diazonium modification has been proved.

4.4. Conclusion

Diazonium salt induced aryl film grafting process has been introduced for surface modification of SiCN glassy material for the first time. To verify the grafting of aryl film to the SiCN surface, the chemical bonding between the aryl film layer and the SiCN surface was first analyzed by XPS. After this initial verification, rabbit IgG sandwich immunoassay was performed on the modified SiCN surfaces. For visual detection, FITC and AuNP were individually used as labels which were attached to detection anti-rabbit IgG. Control experiments were performed in parallel to verify the specific detection based on covalent bonding of antibody to aryl film. The resulting SEM images of AuNP distribution and confocal microscopy images of fluorescence both demonstrate uniform and dense coverage of detection target on the samples. As a contrast, the control rarely shows a signal. As a proof of concept, it can be concluded that diazonium chemistry is an effective and simple method to modify glassy SiCN materials. The next step was to apply diazonium chemistry to SiCN NEMS sensor for biofunctionalization, as shown in the next chapter.

The significant advantage of this diazonium chemistry process is its universal application to all types of materials and is a competitive alternative to electrochemistry. Potentially, this surface modification method can be expanded to sensors with various surface materials.

Chapter 5 Diazonium functionalization of SiCN nanostring biosensors

5.1 Introduction

5.1.1 Surface modification of MEMS/NEMS beam sensors

An ideal biofunctionalization layer should have high performance in the three aspects: sensitivity, specificity, and stability. As stated in the previous two chapters, based on the mass sensitive principle, the easiest way to reach high sensitivity is to lower the mass of the beam itself and make it comparable to that of the detection target. That is the primary motivation of scaling down beam resonators from micro- size to nanoscale dimensions. As with any type of biosensors, surface modification is of crucial importance to MEMS/NEMS beam sensors. However, the strategy to graft functional group onto the suspended nanostring and nanowire device is challenging compared to that of micro-beams. First, surface modification involves ionized gas (plasma, corona discharge, and flame treatment) which may not only deteriorate the surface of the material but even damage the tiny and fragile suspended nanostring. It is possible to cause permanent failure of the NEMS device itself. Second, MEMS sensors with silane monolayers easily decompose and result in desorption of bio-analytes from material surfaces [157,158]. This may not be a significant problem for micro-beam sensors due to their relatively larger size, but for the small surface size and device mass of nanostrings, the coverage of modification layer and analytes is largely reduced when the silane monolayer decomposes. The decomposition of the silane layer can result in inaccurate

quantitative measurement and reduction of the detection sensitivity. The wet chemical and electrochemistry surface modification methods seem to be a good candidate for the case of NEMS surfaces due to their flexible adaptability to different materials. As stated before, SiCN material is chosen for its amenability to nanometer-scale machining. However, electrochemistry requires electron transfer at the surface which is not suitable for SiCN. The traditional wet chemical surface modification methods often use harsh chemicals, organic solvents, or strong bases, which cause side effects to common biosensors. In particular circumstances when vigorous fluid wash is needed, there is a potential risk to physically damage the nanostrings. To summarize, compared to larger, static biosensors, the NEMS biosensor requires a special type of surface modification.

Beyond the general requirements for all type of biosensors, additional restrictions are preferred for the surface modification for nanostring biosensors. First, the surface modification process should be gentle enough not to physically or chemically deteriorate the material surface and structure of the device. Second, the bonding between the functional group and substrate is robust and stable to maintain constant coverage of the layer. Third, the thin functional layer with small added mass should not lower the sensitivity of the device. Fourth, etching the material or introducing contamination should be avoided as they change the mass of the nanostring. Finally, stiction effects often takes place when MEMS/ NEMS beams are removed from liquid and dried. The proper solution is one factor in preventing possible stiction of the nanostrings to the substrate.

5.1.2 Diazonium chemistry for NEMS biosensors

As investigated in literature, diazonium induced aryl film bonding to the substrate is thermally and mechanically stable [143]. This ensures a stable coverage of functional groups. Various methods of diazonium salt induced polymer grafting [143] has been investigated and reported in recent

years, as depicted in Fig. 5.1. The key to diazonium chemistry is the loss of the diazonium group from aryl diazonium salt and the creation of aryl radicals, which reacts with the material surface and forms bond between the aryl layer and the substrate. Multiple trigger mechanism that are able to cause the dediazonation reactions have been explored on different materials [143]. These methods include electrochemisty, photochemistry, ultrasonication, heating and microwave, mechanical grafting, reducing substrate, reducing agent. However not all of them fit the specific needs of fragile nanostrings. For instance, ultrasonication and mechanical grafting can cause the breaking of nanostrings. For heating induced dediazonation, the aryl layer and the nanostring cools down to room temperature after chemical reaction. The heating temperature required for diazonium group lost is relatively high. But in the case of suspended nanostrings, the mismatch of material properties between the functional layer and substrate can be a factor which can alter their mechanical properties and thus their resonant frequencies. Depending on the photosensitivity of the material surface itself, the wavelength and dose of light used in the photochemistry may need to be studied and minimized. Electrochemistry requires substrate to be conductive and restricted from non-conductive insulators. Spontaneous diazonium reduction takes place only on the surface of the reducing substrate.

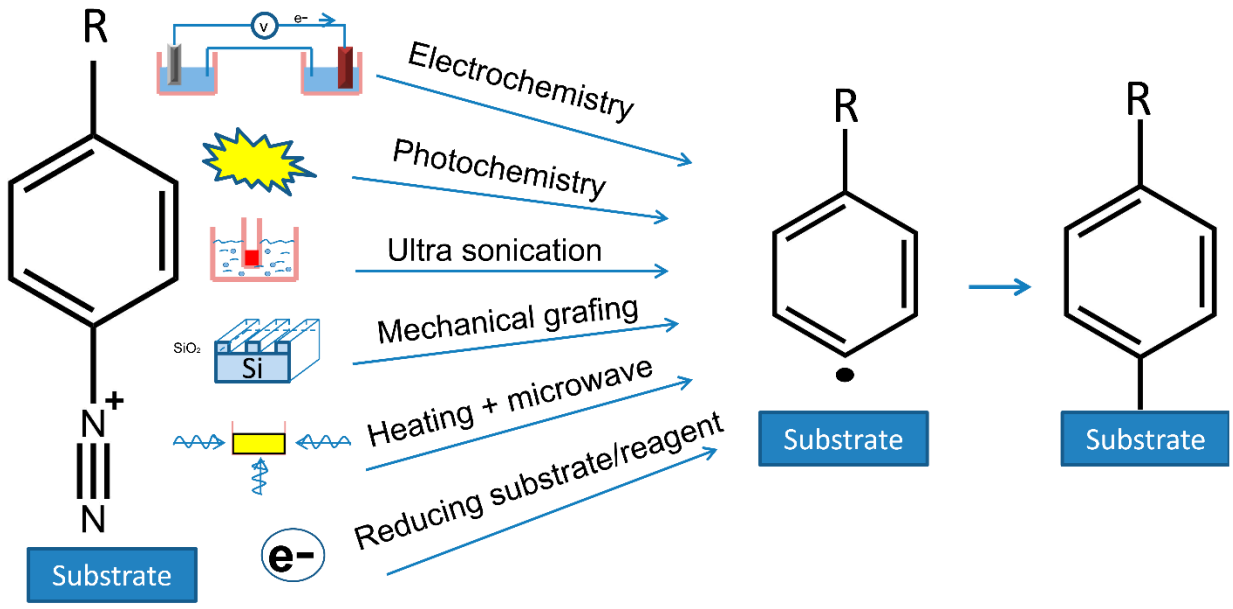

Fig. 5.1 Methods for diazonium salt reduction and aromatic ring grafting

In contrast, a variety of reducing reagents are effective for providing electrons for dediazonation and producing aryl radicals [133,159]. This process is conducted in room temperature, open air, ambient pressure and aqueous. No strong solvents, electricity, light or mechanical vibration is needed. Hence, this process is considered to be both chemically and physically harmless to the nanostring surface. The simple reagent involved in this one step chemistry reaction does not produce byproducts. Another benefit is that aryl molecules terminated with active functional groups are directly bonded to the surface of the material itself without any intermediate layer, which only adds a small amount of extra mass of the modified layer. For nanostrings, a mass as small as possible is preferred, thus this chemistry maintains the high sensitivity of the nanostring.

During the device nanofabrication process, after the nanostring is released from KOH etching of bulk Silicon, the device is water rinsed and nitrogen blow dried. It is observed that the suspended nanostring does not encounter the problem of stiction in water. No critical point drying is required. No transition from water to IPA is required to prevent stiction. Therefore, it is reasonable to assume that the water based diazonium reduction chemistry has a small chance of causing stiction of the nanostrings. Based on the above merits of the diaznonium reduction induced chemical process, diazonium chemistry is a promising functionalization method for nanostrings in high sensitivity detection.

5.1.3 Structure of this chapter

The previous chapter presented the initial validation of the effectiveness of diazonium induced aryl film grafting chemistry process as a surface modification method of SiCN material. This chapter shows how diazonium salt chemistry has been developed to bio-functionalize the SiCN nano-string resonators[70]. The same covalent bio-functionalization protocol, as used on SiCN bare chips previously, has been employed and applied onto the SiCN nanostrings to keep the agreement with the XPS analysis and immunoassay. Anti-rabbit IgG proteins were covalently immobilized onto the nanostring surface by forming amide bonds. A blocking layer was then added to inhibit non-specific binding. The nanostrings were then exposed to solutions containing the target analyte, rabbit IgG. The mass-sensitive resonant frequency was assessed before and after the immobilization of the protein in each step. The added mass of the recognition agent and target protein were individually calculated from the resonance frequency shifts. Negative control experiments were performed by exposing similarly functionalized devices to solutions containing goat IgG. Helium ion microscopy (HIM) was conducted on the functionalized and pristine nanostrings to further observe the immobilized analytes wrapped on the nanostrings.

5.2 Experiment

5.2.1 Laser interferometry measurement

The resonant frequency of the nanostrings are measured using the same method as described in section 1.3.1.2

5.2.2 Nanostring resonator surface biofunctionalization

Similar to the biofunctionalization procedure of SiCN chips described in details in chapter 4, the biofunctionalization of the double clamped nanostrings includes diaznonium salt induced surface modification, immobilization of molecular probe, adsorption of molecular target, and non-adsorption of control analyte, as illustrated in Fig. 5.2. Three identical SiCN resonator chips (A, B, C) were chosen for this experiment. Each of the chips has an array of SiCN nanostrings, with lengths of 15 μm and varying widths ranging from 180 nm to 300 nm, as shown in the SEM image (Fig. 2.13). For the purpose of clarity, it is noted that chip A is immobilized with only the probe molecules onto the nanostring, which corresponds to the case shown in panel B of Fig. 5.2. Chip B is used to absorb the target molecules onto the nanostring, as shown in panel C of Fig. 5.2. Chip C is used as a control in which nanostrings are exposed to non-target molecules, as the case in panel D of Fig.5.2.

5.2.2.1 Diazonium surface modification of nanostring resonators

The protocol of diazonium surface modification of nanostring resonators are exactly the same as the protocol used for surface modification of SiCN bare chips as described in chapter 4.2.4. First, the three identical SiCN resonator chips (A, B, C) were pre-cleaned with cold (<40 ℃) piranha (3:1 96% H_2SO_4: 30% H_2O_2) for 15 min and BOE (buffered oxide etch,

10:1 HF: NH4F) for 3 min. A 0.05M 4-carboxybenzenediazonium tetrafluoroborate solution and a 0.05M L-ascorbic acid solution in Milli-Q water were individually prepared.

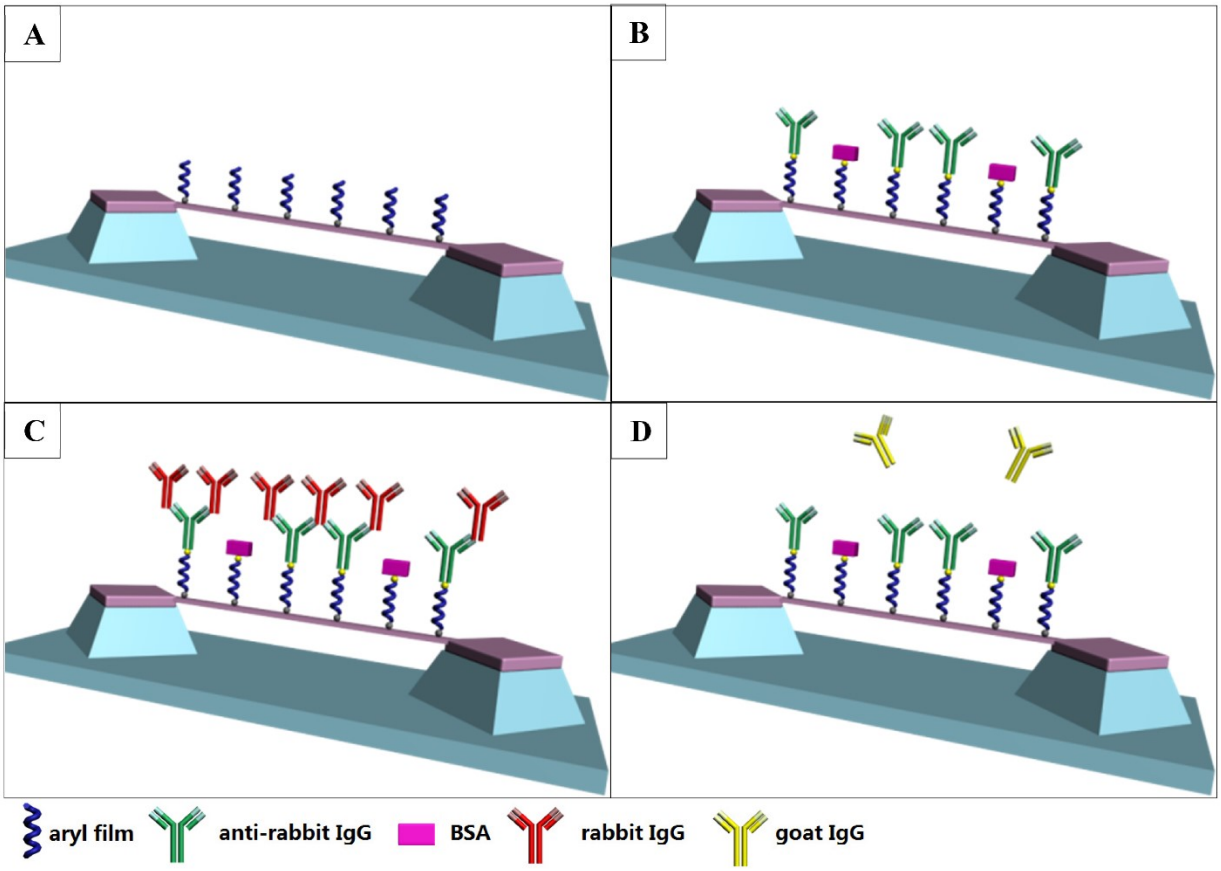

Fig. 5.2 Surface modification and immobilization of molecular probe and target onto SiCN nanostrings. (a) SiCN resonators were modified by aryl diazonium salt; (b) The probe anti-rabbit IgG antibody was immobilized onto the diazonium layer; (c) The target rabbit IgG binds to the probe rabbit IgG antibody; (d) The control goat IgG does not bind to the probe rabbit IgG antibody.

A 2 mL 4-carboxybenzenediazonium tetrafluoroborate solution was poured dropwise onto the SiCN nanostring resonator chips. 1 mL of L-ascorbic acid (VC) solution was added dropwise to the diazonium solution. The SiCN resonator chips were incubated in the mixture for 60 min at room temperature. Then the chips were individually rinsed in water, ethanol, acetone, and DMF without sonication to prevent mechanical damage to resonator strings, followed by gentle nitrogen blow dry. The aromatic polymer layer with carboxyl group was then grafted onto the nanostring surfaces.

5.2.2.2 Activation of carboxyl groups

Immediately after surface modification, the carboxyl-bearing SiCN resonator chips were incubated in the mixture of 1:1 volume ratio of 0.4M EDC (N-(3-dimethylaminopropyl)-N′-ethylcarbodiimide hydrochloride) solution and 0.1M NHS (N-hydroxysuccinimide) solution for 30 min at room temperature and then were rinsed by PBS (phosphate buffered saline).

5.2.2.3 Immobilization of recognition bioreceptor

Three resonator chips (A, B, C) were individually immersed in a solution of 1 mL goat anti-rabbit IgG (100μg/ml in PBS, polyclonal, Sigma-Aldrich) and incubated at room temperature for 2h. The goat anti-rabbit IgG was immobilized onto the SiCN resonator surface by covalently binding to the activated carboxyl groups. The chips were rinsed and then immersed in 1% BSA at room temperature to block the non-specific binding sites of the surface. After 1 h, the chip surfaces were rinsed and dried.

One resonator chip (A) was loaded in the interferometry system to measure the resonance frequency associated with the added mass of anti-rabbit IgG and BSA. The other two

samples (B and C) were used for the further capture of the target protein and for the negative control experiments, respectively.

5.2.2.4 Capture of target and negative control

The target protein rabbit IgG was adsorbed to the sensor surface by incubating the bioreceptor-grafted resonator chip B in 1 mL of rabbit IgG solution (200μg/ml in PBS, polyclonal, Sigma-Aldrich) for 1 h at room temperature. This chip was rinsed and nitrogen blow dried. The shift of resonant frequency of chip B due to the total mass of anti-rabbit IgG, BSA and rabbit IgG was measured by the optical interferometry system.

Control experiment was conducted to observe the non-specific absorption of non-target analyte onto the recognition reagent. Specific detection of target molecule rabbit IgG need to be verified by compare with control experiment. For this purpose, chip C was incubated in 1 mL goat IgG solution (200 μg/ml in PBS, polyclonal, Sigma-Aldrich) for 1 h at room temperature, rinsed and dried. Finally, chip C was also subjected to resonant frequency measurement to evaluate the shift of resonant frequency caused by absorption of anti-rabbit IgG, BSA and possible non-specific bonding of goat IgG.

5.2.3 Helium ion microscopy inspection of functionalized nanoresonators

Helium ion microscopy is a relatively novel ultrahigh resolution imaging technique. One outstanding merit of helium ion imaging compared to SEM is that no charge is built on the surface of non-conductive samples. HIM does not require deposition of a conducting layer of metal on top of the insulating samples and therefore is able to provide a true rendering of topography especially when the surface roughness and feature size are smaller than tens of nanometers. As additional

validation of the absorption of proteins onto the nanostrings, high resolution HIM (Zeiss ORION NanoFab) was performed to inspect the surface protein coverage of both the functionalized resonator chip B and a pristine chip as contrast. Both chips were inspected at beam energy of 31 kV, beam current of 0.4 pA and stage tilt angle of 45°.

5.3 Results and Discussion

5.3.1 Covalent immobilization of Anti-Rabbit IgG to SiCN resonator

The resonant frequency of a clamped-clamped beam of rectangular cross-section under a tensile stress σ, vibrating in the direction perpendicular to its width, is given by [126]:

$$f_i = \frac{22.373}{4\pi}\sqrt{\frac{Et^2}{3\rho l^4} + \frac{4\sigma}{22.373\rho l^2}} \tag{5.1}$$

where l, t, E, and ρ are the length, thickness, Young's modulus and density, respectively. A prior study conducted on similarly fabricated nanostrings showed that a tensile stress of 100 – 150 MPa was sufficient to have the nanostring deemed as operating in a high-stress limit [96]. With an average tensile stress of ~175 MPa, the nanostrings reported here are thus similarly operating in this regime. The second term of Equation 5.1 thus dominates over the first one, and the relationship becomes:

$$f_i = \frac{\sqrt{22.373}}{2\pi}\sqrt{\frac{\sigma}{\rho}}\frac{1}{l} \tag{5.2}$$

More specifically, the strings employed in this study possessed a length l = 15 μm and a density of ρ = 2200 kg/m3 [96]. The frequency of the first resonance mode is thus expected to be f_i = 14.2 MHz. Fig.5.3 shows that the bare devices displayed resonant frequencies ranging from f = 14.0 MHz to f = 14.6 MHz, thus in agreement with Equation 5.2. The range of experimental frequencies observed is attributed to local variations of stress within the wafer, as was observed in prior studies [31,96,98].

The binding of anti-rabbit IgG and BSA onto the nanostrings was quantified through assessment of resonant frequency downshifts. Fig.5.3 (A) reports the resonant frequency of the nanostrings before and after the immobilization of anti-rabbit IgG and BSA.

Significant average frequency downshifts from 251.5±22.8 KHz to 419.4±31.3 KHz, corresponding to different resonator string widths, were observed. The corresponding added mass was calculated using Equation. 5.3:

$$\Delta f = \frac{f_0 \Delta m/s}{2\rho}\left(\frac{1}{t} + \frac{1}{w}\right) \qquad (5.3)$$

where f_0 and Δf are the unloaded resonant frequency and the absolute value of frequency shift induced by the loaded mass, $\Delta m/s$ is the mass-per-area; and ρ, s, v, l, t, w are the density, effective area, volume, length, thickness and width of the nanostring, respectively.

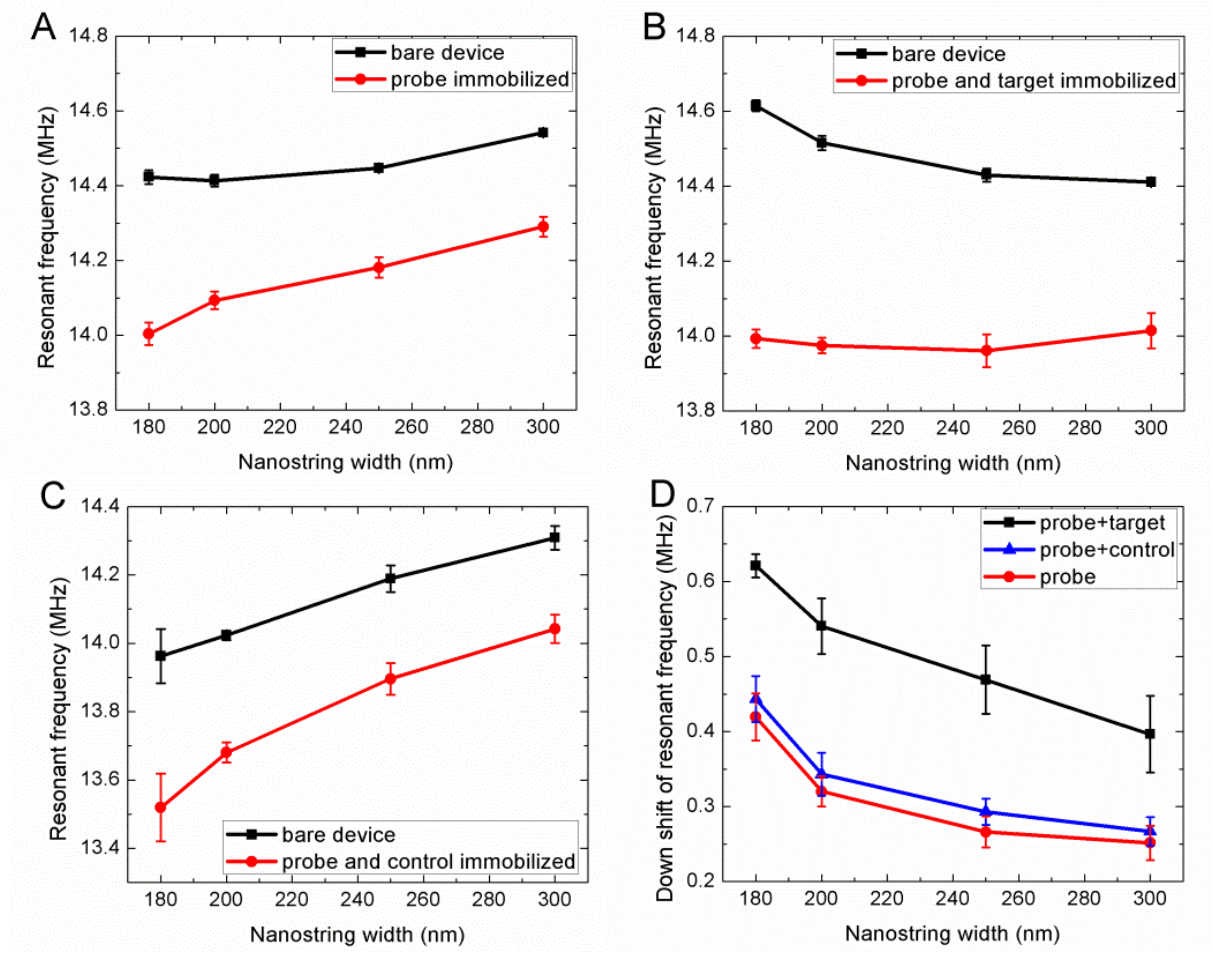

Fig. 5. 3 Resonant frequency change of nanostring resonators in samples A, B and C due to surface functionalization. Each of the chips has an array of 20 devices. The resonant frequency is obtained based on statistical analysis of 5 devices of the same string width. (A) Chip A: bare device versus the attachment of aryl film, anti-rabbit IgG and BSA. The black squares and red circles respectively designate the bare resonators and resonators immobilized with probe *i.e.* anti-rabbit IgG and BSA. (B) Chip B: bare device versus the attachment of aryl film, anti-rabbit IgG, BSA and rabbit IgG. The black squares and red circles respectively designate the bare resonators and resonators immobilized with probe *i.e.* anti-rabbit IgG and BSA and target rabbit IgG. (C) Chip C: bare device versus the

attachment of aryl film, anti-rabbit IgG, BSA and goat IgG. The black squares and red circles respectively designate the bare resonators and resonators immobilized with probe *i.e.* anti-rabbit IgG, BSA and control goat IgG. (D) Comparison of down shifts of resonant frequencies due to the surface adsorption of probe, probe and target, and probe and control. The red circles designate the resonators of chip A immobilized with probe *i.e.* anti-rabbit IgG, BSA. The black squares correspond to the resonators of sample B immobilized with probe and target rabbit IgG. The blue triangles designate the resonators of sample C immobilized with probe and control goat IgG.

Table 5.1 Analysis of average resonant frequency shift and added mass of the resonator array of sample A due to the attachment of aryl film, anti-rabbit IgG and BSA.

Nanostring width (nm)	300	250	200	180
Average unloaded frequency f_0 (MHz)	14.54±0.01	14.45±0.01	14.41±0.02	14.42±0.02
Average shift frequency due to probe Δf (KHz)	$(2.5\pm0.2)*10^2$	$(2.7\pm0.2)*10^2$	$(3.2\pm0.2)*10^2$	$(4.20\pm0.3)*10^2$
Added mass of probe Δm (fg)	17±2	15±1	15±1	17±1
Added mass-per-area of probe Δm/s (fg/μm^2)	1.6±0.2	1.7±0.1	2.0±0.12	2.5±0.2

Table 5.1 summarizes the added mass inferred from these experiments. An average mass-per-area of 1.94 ± 0.20 fg/μm^2 was obtained for different string widths. It was observed that the frequency shift increased as the string width decreases, *i.e.*, narrower strings showed more sensitive response. This can be expected from the following argument. Since f_0 does not change with string width [96], Δf is proportional to the ratio of the effective surface area and the volume of the string, assuming that the bio molecules are uniformly distributed on the string surfaces *i.e.* the added mass-per-area remains constant for different string widths. Further derivation shows Δf increases when the string width decreases (Eq. 5.3).

The mass sensitivity δm of a mechanical resonator is:

$$\delta m = 2M_e \sqrt{\frac{\Delta f}{Q\omega_0}} 10^{-DR/20} \tag{5.4}$$

where M_e is the effective mass of the resonator, Δf is the measurement of the bandwidth of the instrument, $Q$is the quality factor of the resonator, $\omega_0 = 2\pi f_0$, DR is the dynamic range. Considering $Q = 5000$, $DR \approx 40$, $\Delta f = 100$, the calculated mass sensitivity for the resonator arrays are in the range of 90 zg to 149 zg depending to the different widths. The experimental results of added mass are in the fg level, well within the sensitivity. This also indicates that these resonators are potentially able to detect samples of much lower concentrations.

5.3.2 Specific detection of target rabbit IgG attached to resonator

Fig.5.3 (B) shows nanostring frequency shifts due to the immobilization of anti-rabbit IgG, BSA and rabbit IgG (sample B). In turn, Table 5.2 summarizes the total added mass inferred from these shifts. The mass of the target rabbit IgG was obtained by subtracting the combined mass of the anti-rabbit IgG and BSA from the total combined mass of rabbit IgG, anti-rabbit IgG, and BSA. An average added mass-per-area of 1.2 ± 0.1 fg/μm² is thus attributed to the capture of rabbit IgG.

Table 5.2 Analysis of average resonant frequency shift and added mass of the resonator array of sample B due to the attachment of aryl film, anti-rabbit IgG, BSA and target rabbit IgG.

Resonator string width (nm)	300	250	200	180
Average unloaded frequency f_0 (MHz)	14.41±0.01	14.43±0.02	14.52±0.02	14.61±0.01
Average shift frequency due to probe and target Δf (KHz)	(4.0±0.5)*10^2	(4.7±0.5)*10^2	(5.4±0.4)*10^2	(6.2±0.2)*10^2
Added mass of probe and target Δm (fg)	27±4	27±3	25±2	25±1
Added mass-per-area of probe and target Δm/s (fg/μm^2)	2.6±0.3	3.0±0.3	3.3±0.2	3.7±0.1
Added mass-per-area of target Δm/s (fg/μm^2)	1.0±0.3	1.3±0.3	1.4±0.2	1.1±0.2
Total number of target molecules	(41±1)*10^3	(47±1)*10^3	(43±7)*10^3	(30±6)*10^3

Previous study shows that during the process of antibody bio-conjugation to the carboxylic acid group by EDC/NHS activation, only 20% to 25% of the antibody is oriented on the surface of the sample [160]. In this experiment, less than 1/3 of the anti-rabbit IgG molecules were able to bind to the target rabbit IgG. As each anti-rabbit IgG molecule has two binding sites, the expected number of target molecules is 40% to 67% of the number of anti-rabbit IgG molecules. However, the aggregation effect between rabbit IgG molecules may result in non-specific binding. Hence, the number of target rabbit IgG molecules can be estimated in Equation 5.5.

$$N_{r-IgG} = 2R_o * N_{a-r-IgG} + N_A \tag{5.5}$$

In which $N_{a-r-IgG}$ is the number of anti-rabbit IgG molecules immobilized on the surface of the sensor, R_o is the ratio of the number of the oriented anti-rabbit IgG molecules to the number of immobilized anti-rabbit IgG molecules and R_o<1/3, N_{r-IgG} is the number of the rabbit-IgG molecules, N_A is the number of aggregation rabbit IgG molecules. Further, the mass of the rabbit-IgG molecules can be obtained in Equation 5.6

$$M_{r-IgG} = 2R_o * M_{a-r-IgG} + M_A \tag{5.6}$$

in which $M_{a-r-IgG}$ is the mass of anti-rabbit IgG molecules immobilized on the surface of the sensor, M_{r-IgG} is the mass of the rabbit-IgG molecules immobilized on the surface of the sensor, M_A is the mass of aggregated rabbit IgG molecules.

From Table 5.1, the mass of probe is known, which includes the mass of both anti-rabbit IgG and BSA molecules. Therefore,

$$M_{r-IgG} < 2/3 * M_P + M_A \quad (5.7)$$

in which M_P is the mass of the probe immobilized on the surface of the sensor.

To verify the experimental results with the theoretical prediction, take the values of mass-per-area of probe and mass-per-area of target shown in Table 5.1 and Table 5.2 respectively into Equation 5.7, it can be seen that the binding of target to probe was saturated for the nano resonators with string length of 250 nm and 200nm. Besides, there were small amount of aggregation of target molecules. The binding of target to probe for resonators with string width of 180 nm and 300 nm was not saturated. One possible reason for this difference is the non-uniform distribution of aryl film modified on the sensor surface. Another possible factor may be the less or no aggregation in the sensor surface.

Table 5.3 Analysis of average resonant frequency shift of the resonator array of sample C due to the attachment of aryl film, anti-rabbit IgG, BSA and control goat IgG.

Resonator string width (nm)	300	250	200	180
Average unloaded frequency (MHz)	14.31±0.03	14.20±0.04	14.02±0.01	13.97±0.08
Average shift frequency due to probe and control (KHz)	(2.7±0.2)*10^2	(3.0±0.2)*10^2	(3.5±0.3)*10^2	(4.4±0.3)*10^2
Average shift frequency due to control (KHz)	(2±3)*10	(3±2)*10	(2±5)*10	(2±5)*10
Average shift frequency ratio of control to target (percentage)	11%	13%	10%	13%

Negative control experiments were performed to verify the specificity of this detection (sample C). The negative controls consisted of exposing nanostrings similarly functionalized with anti-rabbit IgG to a solution rather containing goat IgG. Fig. 5.3 (C) reports the nanostring frequencies before and after their exposure to anti-rabbit IgG, BSA and goat IgG. The frequency shift due to any attachment of goat IgG was obtained by subtracting the frequency shift associated to the BSA and anti-rabbit IgG probe from the shift associated to bound goat IgG, anti-rabbit IgG, and BSA (Table 5.3). As expected, the frequency shifts related to bound goat IgG are negligible compared to the frequency shift associated to bound rabbit IgG (Table 5.3). The average frequency shifts observed in those negative controls are indeed at least one order of magnitude smaller than those observed in the positive capture experiments, indicating minimal non-specific attachment of non-target protein to the nanostrings. Capture of small amounts of goat IgG remain possible given the polyclonal nature of the two targets, and thus the finite cross species reaction of goat IgG with anti-rabbit IgG. Hence, the significantly larger shift obtained from the target protein compared to the non-targeted one demonstrate the potential of this platform for molecular fingerprinting and multiplexed assays involving a large number of devices.

Given that the native frequencies of bare nanostrings vary slightly within and across chips, the net frequency downshifts for samples A, B and C are plotted for comparison purpose in Fig. 5.3 (D). As reported through Tables 5.2 and 5.3, the attachment of the probe onto the nanostring causes significant frequency downshifts and the subsequent binding of target leads to a further large shift of resonant frequency. Meanwhile, the exposure to the negative control solution results in only slightly shifts of the resonant frequency. In all three cases, nanostrings with the same length but

narrower width tend to display larger frequency shifts, as expected from the model derived in section 5.3.1. The detection threshold is thus effectively improved by using narrower strings.

The chemical processes may themselves have imparted surface stress that influenced the resonance frequencies. Such phenomena have been thoroughly studied in beam sensors [161]. Such effect is typically modelled as an effective additional tension applied to the string. This being said, the associated frequency shifts are expected to be in the range of $\delta f/f_r \sim 10^{-4}$, where f_r is the resonant frequency of the unstressed beam [162]. The nanobeams employed here would possess an unstressed resonant frequency of ~2 MHz. Any effect of surface stress would thus be in the order of a few hundreds of hertz. This range is a thousand-fold less than the net mass-loading shifts reported here, which are in the tens to hundreds of kilohertz. Evidently, surface stress effects may readily account for some of the experimental errors and noise levels observed in our negative control experiment.

5.3.3 HIM observation protein on resonator surface

As seen in the HIM images of Fig. 5.4 (a) and (b), a protein layer was wrapped onto the suspended SiCN nanostring and grafted on the SiCN anchoring pad surface of the functionalized nano resonator chip B. It is noticeable that the protein layer also formed on the Si surface of the slope of the anchoring pad and the substrate. This is to be expected given that diazonium chemistry is also known to functionalize Si surfaces [143].

In contrast, Fig 5.4 (c) shows the surface of a pristine nanostring. Both SiCN nanostrings and Si substrate are markedly smoother and devoid of the lumps associated to polymer attachment. More specifically, the thin undercut slope caused by a previous etching step is observed at the edges of

the SiCN nanostring and the anchoring pad. Such observations further support the notion that the lumpy material seen in Fig 5.4 (a) and (b) is related to the biological analytes.

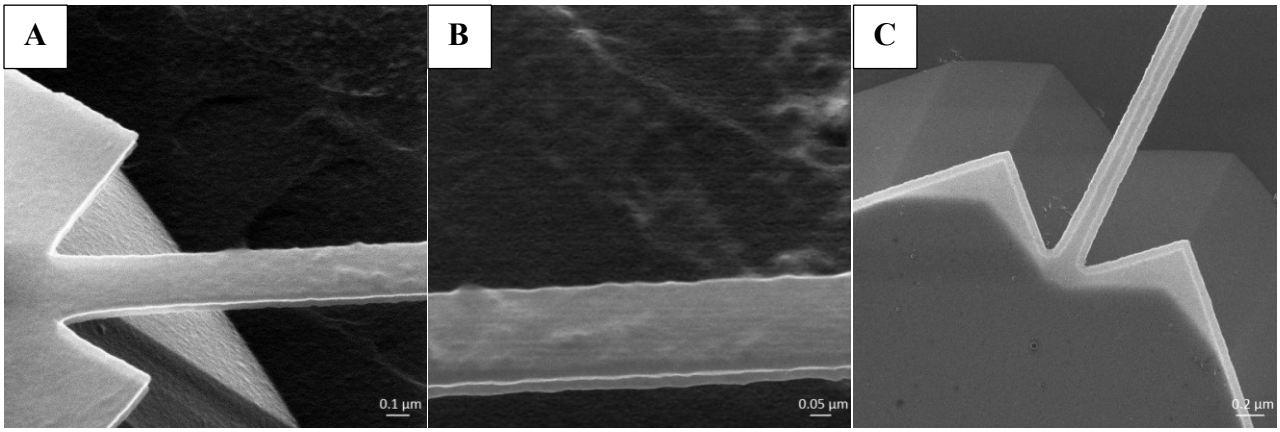

Fig. 5.4. Helium ion micrographs of a SiCN resonator immobilized with anti-rabbit IgG and rabbit IgG with contrast to its pristine surface. Images taken at a 45° tilt angle (a) The protein distribution on SiCN nano resonator anchoring pad and suspended nanostring; (b) High magnification view of protein coverage on the suspended nanostring; (c) Pristine surface of a SiCN nano resonator before functionalization.

5.4 Conclusions and outlook

Diazonium salt induced surface modification has been used as the linker chemistry for the biofunctionalization of glassy nanostring resonators. After verification of the effectiveness of diazonium chemistry for surface modification and biofunctionalization of SiCN material itself in the previous chapter, this chapter adapted the same protocol with SiCN nanostring resonator

arrays. High affinity anti-rabbit IgG and rabbit IgG were immobilized onto diazonium modified nanostrings as molecular probes and targets, respectively. Immobilization of analytes onto the nanostrings was assessed by the shift of mechanical resonant frequency due to the added mass of the analyte. Nanostrings with four different widths ranging from 300 nm down to 180 nm were studied.

Immobilization of the probes and targets were individually detected through significant resonant frequency shifts, averaged through multiple identical samples. On the contrary, negative control experiments showed negligible frequency shifts after exposing the resonator sensor to non-target analytes, confirming the high specificity of the detection. Larger number of devices are needed for experimental investigation of the quantitative relationship between the nanostring width and detection sensitivity. High resolution HIM inspection further verified the true grafting of the analyte molecules on the nanostrings. To summarize, as a proof of concept, diaznonium chemistry has been demonstrated to be an effective modification method to functionalize SiCN nanostring mechanical resonators as a biosensor. Using diaznonium modification chemistry offers greater biocompatibility and a more stable chemical bonding for such applications. Since diazonium chemistry is applicable to many types of materials, this method could readily be expanded to multiplexed assays using diazonium salts bearing different bio-conjugation groups and different molecular probes.

Chapter 6 Conclusion

6.1 Summary of contributions

Overall, this work presents novel methods to enhance the sensitivity and stability of NEMS resonator-based biosensors.

In order to increase the sensitivity relatively to the mass change, extremely small mass nanostrings and nanowires were fabricated. Two fabrication strategies were pursued to minimize the mass of the devices.

1) With traditional top-down fabrication processes, SiCN nanowires as narrow as 10 nm wide were achieved through optimization of an EBL technique.

2) Alternatively, a novel method which circumvents lithography challenges was used to perform post-fabrication modification of the nanostrings. A helium ion beam was employed to mill arrays of pores along the length of the nanostrings and effectively reduced the device mass. This novel post fabrication method has almost 100% yield. This helium ion beam milling technique is flexible, precise and highly controllable, which makes it perfect to tune and trim the physical properties, such as film stress, equivalent density, and resonant frequency, of the nanomechanical resonators.

In order to increase the stability and reliability of the nanomechanical string biosensor, a novel chemistry process was introduced for the surface modification of SiCN glassy nanomechanical resonators.

1) The diazonium salt induced aryl film grafting chemistry has been found to provide stable and strong chemical bonding to the substrate. As a first step, diazonium chemistry was tested on bare SiCN to test its feasibility as a linker on the SiCN strings. The diazonium modified SiCN surface was analyzed by XPS. The chemical bonding between the aryl film and the SiCN surface was verified. A rabbit IgG sandwich immunoassay, using FITC and AuNP as individual labels, was performed on the diaznonium modified bare SiCN surface. The imaging results concluded the capability of specific detection based on the covalent bonding of the protein to the diazonium modified SiCN suface.

2) The diazonium linker chemistry was applied to SiCN strings. High-affinity secondary and primary antibodies, as probe and target respectively, were immobilized onto the SiCN strings using diazonium chemistry as linker. Immobilization of the probe and target were individually assessed by the shifts of mechanical resonant frequencies of the nanostrings. Significant frequency shifts were observed. Frequency shifts of the control nanostring resonators are within noise-level. As a proof of concept, diazonium chemistry has been demonstrated to be an effective modification method to functionalize SiCN nanostring mechanical resonators. Hence, the stability and reliability of the nanostring resonator biosensors were largely enhanced by the diazonium modification chemistry.

6.2 Future work

One goal of biosensor research is their adoption for clinical applications. For this purpose, multiplexed detection of targets and high sensitivity is necessary. Hence, the recommended future work concerning nanomechanical string-based biosensors has two aspects:

1) Use the ultra-narrow nanowire resonators for high sensitivity detection. In this case, the detection analytes can be either with small molecule weights or at low concentrations. Compared to wider nanostrings, the frequency sensitivity relative to the loaded mass of target analyte on the ultra-narrow nanostrings and nanowires is expected to increase. The current bottle-neck preventing such a work is the difficulties in resonant frequency measurement. As stated in previous chapters, it is time-consuming and inaccurate to focus and align laser spot onto ultra-narrow nanowires using the current manual interferometry frequency measurement system. Therefore, the interferometry system need to be improved. For instance, automated laser path alignment using CCD camera technique could increase the alignment accuracy while required less operation time.

2) Use the porous nanostrings to detect small molecules at low concentrations. Resonant frequency measurement is not expected to be difficult in this case. However, the resonant frequency of porous nanostrings is slightly reduced compared to regular non-porous nanostrings with the same length and width. At this stage, it is uncertain whether the detection sensitivity will increase or not. The appeal of the helium ion beam milling method is the flexibility and controllability in the number and size of the pores. The pores on the nano-cantilevers can be milled to optimize their dimensions thus maximizing the detection of biochemical analytes. In this way, the sensitivity can be enhanced by the tailoring capability of ion beam milling.

3) In this work only one type of functional group was used in the diazonium functionalization. Aryl diazonium salts bearing functional groups other than carboxyl groups can be tested and compared to maximize detection sensitivity.

4) The nanosring arrays can be separated to sub-arrays, each of which corresponds to a certain type of detection target. This would allow multiple targets to be detected simultaneously.

5) A sensor can be tailored to minimize the mass of the nanostring and optimize the surface chemistry. This sensor could then potentially be employed for single molecule detection. This exploration could then reveal fundamental biological and physical properties of the molecules.

6) It would be interesting to systematically study the elemental composition of SiCN material. To investigate how the carbon and nitrogen composition affect the tunability of SiCN film stress might help to optimize the film deposition and annealing process.

To summarize, the technology of NEMS resonator based biosensor still remains at its infancy. Despite its unique merits, such as label-free, integration with electronics, flexible readout etc., issues of sensitivity and stability has limited its clinical application. This thesis work investigated two methods to improve the detection sensitivity and stability. These methods are expected to be further developed and optimized to implement reliable and ultra-sensitive biological detection.

Reference

1. Haes, Amanda, J.; Chang, L.; Klein, William, L.; Duyne, Richard, P. Detection of a Biomarker for Alzheimer's Disease from Synthetic and Clinical Samples Using a Nanoscale Optical Biosensor. *Expert Rev. Mol. Diagn.* **2005**, 2264–2271.

2. Tothill, I. E. Biosensors for cancer markers diagnosis. *Semin. Cell Dev. Biol.* **2009**, *20*, 55–62.

3. Giuliano, K. a; Taylor, D. L. Fluorescent-protein biosensors: new tools for drug discovery. *Trends Biotechnol.* **1998**, *16*, 135–40.

4. Keusgen, M. Biosensors: New approaches in drug discovery. *Naturwissenschaften* **2002**, *89*, 433–444.

5. Cooper, M. A. Optical biosensors in drug discovery. *Nat. Rev. Drug Discov.* **2002**, *1*, 515–528.

6. Gartia, M. R.; Braunschweig, B.; Chang, T.-W.; Moinzadeh, P.; Minsker, B. S.; Agha, G.; Wieckowski, A.; Keefer, L. L.; Liu, G. L. The microelectronic wireless nitrate sensor network for environmental water monitoring. *J. Environ. Monit.* **2012**, *14*, 3068–75.

7. Liao, J. C.; Mastali, M.; Gau, V.; Suchard, M. a.; Møller, A. K.; Bruckner, D. a.; Babbitt, J. T.; Li, Y.; Gornbein, J.; Landaw, E. M.; McCabe, E. R. B.; Churchill, B. M.; Haake, D. a. Use of electrochemical DNA biosensors for rapid molecular identification of uropathogens in clinical urine specimens. *J. Clin. Microbiol.* **2006**, *44*, 561–570.

8. Lieberzeit, P. A.; Dickert, F. L. Rapid bioanalysis with chemical sensors: Novel strategies for

devices and artificial recognition membranes. *Anal. Bioanal. Chem.* 2008, *391*, 1629–1639.

9. Cho, H.; Lee, B.; Liu, G. L.; Agarwal, A.; Lee, L. P. Label-free and highly sensitive biomolecular detection using SERS and electrokinetic preconcentration. *Lab Chip* **2009**, *9*, 3360–3363.

10. Yu, L.; Liu, G. L.; Kim, J.; Mejia, Y. X.; Lee, L. P. Nanophotonic crescent moon structures with sharp edge for ultrasensitive biomolecular detection by local electromagnetic field enhancement effect. *Nano Lett.* **2005**, *5*, 119–124.

11. Densmore, a; Vachon, M.; Xu, D.-X.; Janz, S.; Ma, R.; Li, Y.-H.; Lopinski, G.; Delâge, a; Lapointe, J.; Luebbert, C. C.; Liu, Q. Y.; Cheben, P.; Schmid, J. H. Silicon photonic wire biosensor array for multiplexed real-time and label-free molecular detection. *Opt. Lett.* **2009**, *34*, 3598–3600.

12. Ray, S.; Mehta, G.; Srivastava, S. Label-free detection techniques for protein microarrays: Prospects, merits and challenges. *Proteomics* **2010**, *10*, 731–748.

13. Taylor, A. D.; Yu, Q.; Chen, S.; Homola, J.; Jiang, S. Comparison of E. coli O157:H7 preparation methods used for detection with surface plasmon resonance sensor. In *Sensors and Actuators, B: Chemical*; 2005; Vol. 107, pp. 202–208.

14. Liu, X.; Hu, Y.; Zheng, S.; Liu, Y.; He, Z.; Luo, F. Surface plasmon resonance immunosensor for fast, highly sensitive, and in situ detection of the magnetic nanoparticles-enriched Salmonella enteritidis. *Sensors Actuators B Chem.* **2016**, *230*, 191–198.

15. Arya, S. K.; Singh, A.; Naidoo, R.; Wu, P.; McDermott, M. T.; Evoy, S. Chemically immobilized T4-bacteriophage for specific Escherichia coli detection using surface plasmon

resonance. *Analyst* **2011**, *136*, 486–92.

16. Singh, A.; Arya, S. K.; Glass, N.; Hanifi-Moghaddam, P.; Naidoo, R.; Szymanski, C. M.; Tanha, J.; Evoy, S. Bacteriophage tailspike proteins as molecular probes for sensitive and selective bacterial detection. *Biosens. Bioelectron.* **2010**, *26*, 131–138.

17. Butet, J.; Brevet, P.-F.; Martin, O. J. F. Optical Second Harmonic Generation in Plasmonic Nanostructures: From Fundamental Principles to Advanced Applications. *ACS Nano* **2015**, *9*, 10545–62.

18. Langer, J.; Novikov, S. M.; Liz-Marzán, L. M. Sensing using plasmonic nanostructures and nanoparticles. *Nanotechnology* **2015**, *26*, 322001.

19. Nguyen, H. H.; Park, J.; Kang, S.; Kim, M. Surface plasmon resonance: A versatile technique for biosensor applications. *Sensors (Switzerland)* 2015, *15*, 10481–10510.

20. Wang, P.; Bo, L.; Semenova, Y.; Farrell, G.; Brambilla, G. Optical microfibre based photonic components and their applications in label-free biosensing. *Biosensors* 2015, *5*, 471–499.

21. Kneipp, K.; Wang, Y.; Kneipp, H.; Perelman, L. T.; Itzkan, I.; Dasari, R. R.; Feld, M. S. Single molecule detection using surface-enhanced Raman scattering (SERS). *Phys. Rev. Lett.* **1997**, *78*, 1667–1670.

22. Aebersold, R.; Mann, M. Mass spectrometry-based proteomics. *Nature* **2003**, *422*, 198–207.

23. Mehrvar, M.; Bis, C.; Scharer, J. M.; Young, M. M.-; Luong, J. H. Fiber-Optic Biosensors. Trends and Advances. *Anal. Sci.* **2000**, *16*, 677–692.

24. Fung, Y. S.; Wong, Y. Y. Self-assembled monolayers as the coating in a quartz piezoelectric

crystal immunosensor to detect Salmonella in aqueous solution. *Anal. Chem.* **2001**, *73*, 5302–5309.

25. Chang, Y.-P.; Liu, W.-C.; Tseng, M.-C.; Chu, Y.-H. Ionic liquids tailored for reaction-based gas sensing on quartz crystal microbalance. *Rev. Anal. Chem.* **2015**, *34*, 77–86.

26. Länge, K.; Rapp, B. E.; Rapp, M. Surface acoustic wave biosensors: A review. *Anal. Bioanal. Chem.* 2008, *391*, 1509–1519.

27. Ilic, B.; Czaplewski, D.; Zalalutdinov, M.; Craighead, H. G.; Neuzil, P.; Campagnolo, C.; Batt, C. Single cell detection with micromechanical oscillators. *J. Vac. Sci. Technol. B Microelectron. Nanom. Struct.* **2001**, *19*, 2825.

28. Ilic, B.; Yang, Y.; Craighead, H. G. Virus detection using nanoelectromechanical devices. *Appl. Phys. Lett.* **2004**, *85*, 2604–2606.

29. Poshtiban, S.; Singh, A.; Fitzpatrick, G.; Evoy, S. Bacteriophage tail-spike protein derivitized microresonator arrays for specific detection of pathogenic bacteria. *Sensors Actuators, B Chem.* **2013**, *181*, 410–416.

30. Campbell, G. A.; Medina, M. B.; Mutharasan, R. Detection of Staphylococcus enterotoxin B at picogram levels using piezoelectric-excited millimeter-sized cantilever sensors. *Sensors Actuators, B Chem.* **2007**, *126*, 354–360.

31. Fischer, L. M.; Wright, V. A.; Guthy, C.; Yang, N.; McDermott, M. T.; Buriak, J. M.; Evoy, S. Specific detection of proteins using nanomechanical resonators. *Sensors Actuators, B Chem.* **2008**, *134*, 613–617.

32. Quitoriano, N. J.; Belov, M.; Evoy, S.; Kamins, T. I. Single-crystal, Si nanotubes, and their

mechanical resonant properties. *Nano Lett.* **2009**, *9*, 1511–1516.

33. Bausells, J. Piezoresistive cantilevers for nanomechanical sensing. *Microelectron. Eng.* **2015**, *145*, 9–20.

34. Cui, Y.; Wei, Q.; Park, H.; Lieber, C. M. Nanowire nanosensors for highly sensitive and selective detection of biological and chemical species. *Science* **2001**, *293*, 1289–1292.

35. Waggoner, P. S.; Craighead, H. G. Micro- and nanomechanical sensors for environmental, chemical, and biological detection. *Lab Chip* **2007**, *7*, 1238–1255.

36. Ilic, B.; Czaplewski, D.; Craighead, H. G.; Neuzil, P.; Campagnolo, C.; Batt, C. Mechanical resonant immunospecific biological detector. *Appl. Phys. Lett.* **2000**, *77*, 450–452.

37. Lavrik, N. V.; Sepaniak, M. J.; Datskos, P. G. Cantilever transducers as a platform for chemical and biological sensors. *Rev. Sci. Instrum.* 2004, *75*, 2229–2253.

38. Baller, M. K.; Lang, H. P.; Fritz, J.; Gerber, C.; Gimzewski, J. K.; Drechsler, U.; Rothuizen, H.; Despont, M.; Vettiger, P.; Battiston, F. M.; Ramseyer, J. P.; Fornaro, P.; Meyer, E.; Güntherodt, H. J. A cantilever array-based artificial nose. *Ultramicroscopy* **2000**, *82*, 1–9.

39. Raiteri, R.; Grattarola, M.; Butt, H. J.; Skládal, P. Micromechanical cantilever-based biosensors. *Sensors Actuators, B Chem.* **2001**, *79*, 115–126.

40. Villarroya, M.; Verd, J.; Teva, J.; Abadal, G.; Forsen, E.; Murano, F. P.; Uranga, A.; Figueras, E.; Montserrat, J.; Esteve, J.; Boisen, A.; Barniol, N. System on chip mass sensor based on polysilicon cantilevers arrays for multiple detection. *Sensors Actuators, A Phys.* **2006**, *132*, 154–164.

41. Evoy, S.; Olkhovets, A.; Sekaric, L.; Parpia, J. M.; Craighead, H. G.; Carr, D. W. Temperature-dependent internal friction in silicon nanoelectromechanical systems. *Appl. Phys. Lett.* **2000**, *77*, 2397–2399.

42. Mohammad, M. A.; Dew, S. K.; Evoy, S.; Stepanova, M. Fabrication of sub-10 nm silicon carbon nitride resonators using a hydrogen silsesquioxane mask patterned by electron beam lithography. *Microelectron. Eng.* **2011**, *88*, 2338–2341.

43. Guthy, C.; Belov, M.; Janzen, A.; Quitoriano, N. J.; Singh, A.; Wright, V. A.; Finley, E.; Kamins, T. I.; Evoy, S. Large-scale arrays of nanomechanical sensors for biomolecular fingerprinting. *Sensors Actuators, B Chem.* **2013**, *187*, 111–117.

44. Jensen, K.; Kim, K.; Zettl, a An atomic-resolution nanomechanical mass sensor. *Nat. Nanotechnol.* **2008**, *3*, 533–7.

45. Davis, Z. J.; Abadal, G.; Helbo, B.; Hansen, O.; Campabadal, F.; P??rez-Murano, F.; Esteve, J.; Figueras, E.; Verd, J.; Barniol, N.; Boisen, A. Monolithic integration of mass sensing nano-cantilevers with CMOS circuitry. *Sensors Actuators, A Phys.* **2003**, *105*, 311–319.

46. Yang, Y. T.; Callegari, C.; Feng, X. L.; Ekinci, K. L.; Roukes, M. L. Zeptogram-scale nanomechanical mass sensing. *Nano Lett.* **2006**, *6*, 583–6.

47. Gil-Santos, E.; Ramos, D.; Martínez, J.; Fernández-Regúlez, M.; García, R.; San Paulo, A.; Calleja, M.; Tamayo, J. Nanomechanical mass sensing and stiffness spectrometry based on two-dimensional vibrations of resonant nanowires. *Nat. Nanotechnol.* **2010**, *5*, 641–645.

48. Tamayo, J.; Kosaka, P. M.; Ruz, J. J.; San Paulo, Á.; Calleja, M. Biosensors based on

nanomechanical systems. *Chem. Soc. Rev.* **2013**, *42*, 1287–311.

49. McKendry, R.; Zhang, J.; Arntz, Y.; Strunz, T.; Hegner, M.; Lang, H. P.; Baller, M. K.; Certa, U.; Meyer, E.; Güntherodt, H.-J.; Gerber, C. Multiple label-free biodetection and quantitative DNA-binding assays on a nanomechanical cantilever array. *Proc. Natl. Acad. Sci. U. S. A.* **2002**, *99*, 9783–9788.

50. Sadek, A. S.; Karabalin, R. B.; Du, J.; Roukes, M. L.; Koch, C.; Masmanidis, S. C. Wiring nanoscale biosensors with piezoelectric nanomechanical resonators. *Nano Lett.* **2010**, *10*, 1769–1773.

51. Zheng, G.; Patolsky, F.; Cui, Y.; Wang, W. U.; Lieber, C. M. Multiplexed electrical detection of cancer markers with nanowire sensor arrays. *Nat. Biotechnol.* **2005**, *23*, 1294–1301.

52. Ziegler, C. Cantilever-like micromechanical sensors. *Anal. Bioanal. Chem.* **2004**, *379*, 946–959.

53. Boisen, A.; Dohn, S.; Keller, S. S.; Schmid, S.; Tenje, M. Cantilever-like micromechanical sensors. *Reports Prog. Phys.* **2011**, *74*, 036101.

54. T. Thundat, P. I. Oden, and R. J. W Microcantilever Sensors. *Microscale Thermophys. Eng.* **1997**, *1*, 185–199.

55. Meyer, G.; Amer, N. Novel optical approach to atomic force microscopy. *Appl. Phys. Lett.* **1988**, *53*, 1045.

56. Meyer, G.; Amer, N. M. Optical-beam-deflection atomic force microscopy: The NaCl (001) surface. *Appl. Phys. Lett.* **1990**, *56*, 2100–2101.

57. Evans, D. R.; Craig, V. S. J. Sensing cantilever beam bending by the optical lever technique and its application to surface stress. *J. Phys. Chem. B* **2006**, *110*, 5450–5461.

58. Lang, H. P.; Baller, M. K.; Berger, R.; Gerber, C.; Gimzewski, J. K.; Battiston, F. M.; Fornaro, P.; Ramseyer, J. P.; Meyer, E.; Güntherodt, H. J. An artificial nose based on a micromechanical cantilever array. In *Analytica Chimica Acta*; 1999; Vol. 393, pp. 59–65.

59. Tenje, M.; Keller, S.; Dohn, S.; Davis, Z. J.; Boisen, A. Drift study of SU8 cantilevers in liquid and gaseous environments. *Ultramicroscopy* **2010**, *110*, 596–598.

60. Lang, H. P.; Berger, R.; Battiston, F.; Ramseyer, J.-P.; Meyer, E.; Andreoli, C.; Brugger, J.; Vettiger, P.; Despont, M.; Mezzacasa, T.; Scandella, L.; Güntherodt, H.-J.; Gerber, C.; Gimzewski, J. K. A chemical sensor based on a micromechanical cantilever array for the identification of gases and vapors. *Appl. Phys. A Mater. Sci. Process.* **1998**, *66*, S61–S64.

61. www.concentris.ch.

62. Lim, S. H. S.; Raorane, D.; Satyanarayana, S.; Majumdar, A. Nano-chemo-mechanical sensor array platform for high-throughput chemical analysis. *Sensors Actuators, B Chem.* **2006**, *119*, 466–474.

63. Yue, M.; Stachowiak, J. C.; Lin, H.; Datar, R.; Cote, R.; Majumdar, A. Label-free protein recognition two-dimensional array using nanomechanical sensors. *Nano Lett.* **2008**, *8*, 520–524.

64. Yue, M.; Lin, H.; Dedrick, D. E.; Satyanarayana, S.; Majumdar, A.; Bedekar, A. S.; Jenkins, J. W.; Sundaram, S. A 2-D microcantilever array for multiplexed biomolecular analysis. *J. Microelectromechanical Syst.* **2004**, *13*, 290–299.

65. Mertens, J.; Álvarez, M.; Tamayo, J. Real-time profile of microcantilevers for sensing applications. *Appl. Phys. Lett.* **2005**, *87*, 234102.

66. Martin, Y.; Williams, C. C.; Wickramasinghe, H. K. Atomic force microscope–force mapping and profiling on a sub 100-Å scale. *J. Appl. Phys.* **1987**, *61*, 4723.

67. Putman, C. A. J.; De Grooth, B. G.; Van Hulst, N. F.; Greve, J. A detailed analysis of the optical beam deflection technique for use in atomic force microscopy. *J. Appl. Phys.* **1992**, *72*, 6.

68. Erlandsson, R. Atomic force microscopy using optical interferometry. *J. Vac. Sci. Technol. A Vacuum, Surfaces, Film.* **1988**, *6*, 266.

69. Carr, D. W.; Craighead, H. G. Fabrication of nanoelectromechanical systems in single crystal silicon using silicon on insulator substrates and electron beam lithography. *J. Vac. Sci. Technol. B* **1997**, 2760–2763.

70. Zheng, W.; Du, R.; Cao, Y.; Mohammad, M.; Dew, S.; McDermott, M.; Evoy, S. Diazonium Chemistry for the Bio-Functionalization of Glassy Nanostring Resonator Arrays. *Sensors* **2015**, *15*, 18724–18741.

71. Belov, M.; Quitoriano, N. J.; Sharma, S.; Hiebert, W. K.; Kamins, T. I.; Evoy, S. Mechanical resonance of clamped silicon nanowires measured by optical interferometry. *J. Appl. Phys.* **2008**, *103*.

72. Blanc, N. Scanning force microscopy in the dynamic mode using microfabricated capacitive sensors. *J. Vac. Sci. Technol. B* **1996**, *14*, 901–905.

73. Erbe, A.; Blick, R. H. Nanomechanical resonators operating at radio frequencies. *Phys. B*

Condens. Matter **1999**, *272*, 575–577.

74. Erbe, A.; Weiss, C.; Zwerger, W.; Blick, R. H. Nanomechanical Resonator Shuttling Single Electrons at Radio Frequencies. *Phys. Rev. Lett.* **2001**, *87*, 096106.

75. Binnig, G.; Quate, C. F. Atomic Force Microscope. *Phys. Rev. Lett.* **1986**, *56*, 930–933.

76. Kenny, T. W.; Waltman, S. B.; Reynolds, J. K.; Kaiser, W. J. Micromachined silicon tunnel sensor for motion detection. *Appl. Phys. Lett.* **1991**, *58*, 100–102.

77. Kenny, T. W. Micromachined tunneling displacement transducers for physical sensors. *J. Vac. Sci. Technol. A Vacuum, Surfaces, Film.* **1993**, *11*, 797.

78. G. Binnig and H. Rohrer SCANNING TUNNELING MICROSCOPY. *IBM J. Res. Dev.* **1986**, *30*, 355.

79. Scheible, D. V.; Erbe, A.; Blick, R. H. Tunable coupled nanomechanical resonators for single-electron transport. *New J. Phys.* **2002**, *4*.

80. Scheible, D. V.; Erbe, A.; Blick, R. H. Dynamic control and modal analysis of coupled nano-mechanical resonators. *Appl. Phys. Lett.* **2003**, *82*, 3333–3335.

81. Yu, J.; Xiao, J.; Ren, X.; Lao, K.; Xie, X. S. Probing gene expression in live cells, one protein molecule at a time. *Science* **2006**, *311*, 1600–1603.

82. Cai, L.; Friedman, N.; Xie, X. S. Stochastic protein expression in individual cells at the single molecule level. *Nature* **2006**, *440*, 358–362.

83. Naik, a K.; Hanay, M. S.; Hiebert, W. K.; Feng, X. L.; Roukes, M. L. Towards single-molecule

nanomechanical mass spectrometry. *Nat. Nanotechnol.* **2009**, *4*, 445–450.

84. Hanay, M. S.; Kelber, S.; Naik, a K.; Chi, D.; Hentz, S.; Bullard, E. C.; Colinet, E.; Duraffourg, L.; Roukes, M. L. Single-protein nanomechanical mass spectrometry in real time. *Nat. Nanotechnol.* **2012**, *7*, 602–8.

85. Lavrik, N. V.; Datskos, P. G. Femtogram mass detection using photothermally actuated nanomechanical resonators. *Appl. Phys. Lett.* **2003**, *82*, 2697–2699.

86. Lassagne, B.; Garcia-Sanchez, D.; Aguasca, A.; Bachtold, A. Ultrasensitive mass sensing with a nanotube electromechanical resonator. *Nano Lett.* **2008**, *8*, 3735–3738.

87. Chiu, H. Y.; Hung, P.; Postma, H. W. C.; Bockrath, M. Atomic-scale mass sensing using carbon nanotube resonators. *Nano Lett.* **2008**, *8*, 4342–4346.

88. M. A. McCord and M. Rooks Electron beam lithography. In *Handbook of microlithography, micromachining and microfabrication (vol. 1)*; SPIE, 1997; pp. 139–250.

89. Nabity, J.; Compbell, L. A.; Zhu, M.; Zhou, W. E-beam Nanolithography Integrated with Scanning Electron Microscope. In *Scanning Microscopy for Nanotechnology*; Springer New York: New York, NY, 2006; pp. 120–151.

90. Pease, R. F.; Chou, S. Y. Lithography and other patterning techniques for future electronics. *Proc. IEEE* **2008**, *96*, 248–270.

91. www.mapperlithography.com.

92. Petric, P.; Bevis, C.; Carroll, A.; Percy, H.; Zywno, M.; Standiford, K.; Brodie, A.; Bareket, N.; Grella, L. REBL: A novel approach to high speed maskless electron beam direct write

lithography. *J. Vac. Sci. Technol. B Microelectron. Nanom. Struct.* **2009**, *27*, 161.

93. www.ims.co.at.

94. Mohammad, M. A. PhD Thesis. Investigation of electron beam nanolithography processes, mechanisms, and applications, University of Alberta, 2013.

95. Fitzpatrick, N. PhD thesis. Novel Materials for the Design of Cantilever Transducers, University of Alberta, 2011.

96. Guthy, C.; Das, R. M.; Drobot, B.; Evoy, S. Resonant characteristics of ultranarrow SiCN nanomechanical resonators. *J. Appl. Phys.* **2010**, *108*.

97. Nelson-Fitzpatrick, N.; Guthy, C.; Poshtiban, S.; Finley, E.; Harris, K. D.; Worfolk, B. J.; Evoy, S. Atomic layer deposition of TiN for the fabrication of nanomechanical resonators. *J. Vac. Sci. {&} Technol. A Vacuum, Surfaces, Film.* **2013**, *31*, 21503.

98. Fischer, L. M.; Wilding, N.; Gel, M.; Evoy, S. Low-stress silicon carbonitride for the machining of high-frequency nanomechanical resonators. *J. Vac. Sci. Technol. B Microelectron. Nanom. Struct.* **2007**, *25*, 33.

99. Mohammad, M. A.; Guthy, C.; Evoy, S.; Dew, S. K.; Stepanova, M. Nanomachining and clamping point optimization of silicon carbon nitride resonators using low voltage electron beam lithography and cold development. *J. Vac. Sci. Technol. B* **2010**, *28*, C6p36–C6p41.

100. Hu, W.; Walter Ultrahigh resolution electron beam lithography for molecular electronics. *ProQuest Diss. Theses ProQuest Diss. Theses Glob. P R E V I E W* **2004**.

101. Grigorescu, A. E.; Hagen, C. W. Resists for sub-20-nm electron beam lithography with a

focus on HSQ: state of the art. *Nanotechnology* **2009**, *20*, 31.

102. Bilenberg, B.; Schøler, M.; Shi, P.; Schmidt, M. S.; Bøggild, P.; Fink, M.; Schuster, C.; Reuther, F.; Gruetzner, C.; Kristensen, a. Comparison of high resolution negative electron beam resists. *J. Vac. Sci. Technol. B Microelectron. Nanom. Struct.* **2006**, *24*, 1776.

103. Bermudez, V. M. Low-energy electron-beam effects on poly(methyl methacrylate) resist films. *J. Vac. Sci. Technol. B Microelectron. Nanom. Struct.* **1999**, *17*, 2512.

104. Olzierski, A.; Raptis, I. Development and molecular-weight issues on the lithographic performance of poly (methyl methacrylate). In *Microelectronic Engineering*; 2004; Vol. 73-74, pp. 244–251.

105. Rooks, M. J.; Kratschmer, E.; Viswanathan, R.; Katine, J.; Fontana, R. E.; MacDonald, S. A. Low stress development of poly(methylmethacrylate) for high aspect ratio structures. *J. Vac. Sci. Technol. B* **2002**, *20*, 2937–2941.

106. Wi, J.; Lee, H.; Kim, K. Enhanced Development Properties of IPA (Isopropyl Alcohol) on the PMMA Electron Beam Resist. *Electron. Mater. Lett.* **2007**, *3*, 1–5.

107. Yasin, S.; Hasko, D. G.; Khalid, M. N.; Weaver, D. J.; Ahmed, H. Influence of polymer phase separation on roughness of resist features. *J. Vac. Sci. Technol. B Microelectron. Nanom. Struct.* **2004**, *22*, 574.

108. Hu, W. (Walter); Sarveswaran, K.; Lieberman, M.; Bernstein, G. H. Sub-10 nm electron beam lithography using cold development of poly(methylmethacrylate). *J. Vac. Sci. Technol. B Microelectron. Nanom. Struct.* **2004**, *22*, 1711.

109. Cord, B.; Lutkenhaus, J.; Berggren, K. K. Optimal temperature for development of poly(methylmethacrylate). *J. Vac. Sci. Technol. B Microelectron. Nanom. Struct.* **2007**, *25*, 2013.

110. Aktary, M.; Stepanova, M.; Dew, S. K. Simulation of the spatial distribution and molecular weight of polymethylmethacrylate fragments in electron beam lithography exposures. *J. Vac. Sci. Technol. B Microelectron. Nanom. Struct.* **2006**, *24*, 768.

111. Namatsu, H.; Takahashi, Y.; Yamazaki, K.; Yamaguchi, T.; Nagase, M.; Kurihara, K. Three-dimensional siloxane resist for the formation of nanopatterns with minimum linewidth fluctuations. *J. Vac. Sci. Technol. B Microelectron. Nanom. Struct.* **1998**, *16*, 69.

112. Olynick, D. L.; Cord, B.; Schipotinin, a.; Ogletree, D. F.; Schuck, P. J. Electron-beam exposure mechanisms in hydrogen silsesquioxane investigated by vibrational spectroscopy and in situ electron-beam-induced desorption. *J. Vac. Sci. Technol. B Microelectron. Nanom. Struct.* **2010**, *28*, 581.

113. Henschel, W.; Georgiev, Y. M.; Kurz, H. Study of a high contrast process for hydrogen silsesquioxane as a negative tone electron beam resist. *J. Vac. Sci. Technol. B Microelectron. Nanom. Struct.* **2003**, *21*, 2018.

114. Fruleux-Cornu, F.; Penaud, J.; Dubois, E.; Fran??ois, M.; Muller, M. An optimal high contrast e-beam lithography process for the patterning of dense fin networks. *Mater. Sci. Eng. C* **2006**, *26*, 893–897.

115. Bell, D. C. Contrast mechanisms and image formation in helium ion microscopy. *Microsc. Microanal.* **2009**, *15*, 147–153.

116. Bell, D. C.; Lemme, M. C.; Stern, L. A.; Marcus, C. M. Precision material modification and patterning with He ions. *J. Vac. Sci. Technol. B* **2009**, *27*, 2755–2758.

117. Sidorkin, V.; van Veldhoven, E.; van der Drift, E.; Alkemade, P.; Salemink, H.; Maas, D. Sub-10-nm nanolithography with a scanning helium beam. *J. Vac. Sci. Technol. B Microelectron. Nanom. Struct.* **2009**, *27*, L18.

118. Winston, D.; Cord, B. M.; Ming, B.; Bell, D. C.; DiNatale, W. F.; Stern, L. a.; Vladar, a. E.; Postek, M. T.; Mondol, M. K.; Yang, J. K. W.; Berggren, K. K. Scanning-helium-ion-beam lithography with hydrogen silsesquioxane resist. *J. Vac. Sci. Technol. B Microelectron. Nanom. Struct.* **2009**, *27*, 2702.

119. Morgan, J.; Notte, J.; Hill, R.; Ward, B. An Introduction to the Helium Ion Microscope. *AIP Conf. Proc.* **2006**, *14*, 489–496.

120. Ramachandra, R.; Griffin, B.; Joy, D. A model of secondary electron imaging in the helium ion scanning microscope. *Ultramicroscopy* **2009**, *109*, 748–757.

121. Yang, J.; Ferranti, D. C.; Stern, L. a; Sanford, C. a; Huang, J.; Ren, Z.; Qin, L.-C.; Hall, A. R. Rapid and precise scanning helium ion microscope milling of solid-state nanopores for biomolecule detection. *Nanotechnology* **2011**, *22*, 285310.

122. Sawafta, F.; Carlsen, A. T.; Hall, A. R. Membrane thickness dependence of Nanopore formation with a focused helium ion beam. *Sensors (Switzerland)* **2014**, *14*, 8150–8161.

123. Tan, S.; Klein, K.; Shima, D.; Livengood, R.; Mutunga, E.; Vladár, A. Mechanism and applications of helium transmission milling in thin membranes. *J. Vac. Sci. Technol. B,*

Nanotechnol. Microelectron. Mater. Process. Meas. Phenom. **2014**, *32*, 06FA01.

124. Verbridge, S. S.; Parpia, J. M.; Reichenbach, R. B.; Bellan, L. M.; Craighead, H. G. High quality factor resonance at room temperature with nanostrings under high tensile stress. *J. Appl. Phys.* **2006**, *99*.

125. Zheng, W.; Li, P.; Hurk, R. Van Den; Evoy, S. Helium Ion Microscope-Assisted Nanomachining of Resonant Nanostrings. *Sensors* **2016**, *16*, 1080.

126. MLA; Weaver Jr, William, Stephen P. Timoshenko, and D. H. Y. *Vibration problems in engineering, 5th ed*; John Wiley & Sons, 1990.

127. Zhang, L. M.; Uttamchandani, D.; Culshaw, B.; Dobson, P. Measurement of Young's modulus and internal stress in silicon microresonators using a resonant frequency technique. *Meas. Sci. Technol.* **1990**, *1*, 1343–1346.

128. Cherian, S.; Thundat, T. Determination of adsorption-induced variation in the spring constant of a microcantilever. *Appl. Phys. Lett.* **2002**, *80*, 2219–2221.

129. Johnson, B. N.; Mutharasan, R. Biosensing using dynamic-mode cantilever sensors: A review. *Biosens. Bioelectron.* 2012, *32*, 1–18.

130. Grieshaber, D.; MacKenzie, R.; Vörös, J.; Reimhult, E. Electrochemical Biosensors - Sensor Principles and Architectures. *Sensors* **2008**, *8*, 1400–1458.

131. Göpel, W.; Heiduschka, P. Interface analysis in biosensor design. *Biosens. Bioelectron.* **1995**, *10*, 853–883.

132. Credou, J.; Volland, H.; Dano, J.; Berthelot, T. A one-step and biocompatible cellulose

functionalization for covalent antibody immobilization on immunoassay membranes. *J. Mater. Chem. B* **2013**, *1*, 3277–3286.

133. Mévellec, V.; Roussel, S.; Tessier, L.; Chancolon, J.; Mayne-L'Hermite, M.; Deniau, G.; Viel, P.; Palacin, S. Grafting polymers on surfaces: A new powerful and versatile diazonium salt-based one-step process in aqueous media. *Chem. Mater.* **2007**, *19*, 6323–6330.

134. Shewchuk, D. M.; McDermott, M. T. Comparison of diazonium salt derived and thiol derived nitrobenzene layers on gold. *Langmuir* **2009**, *25*, 4556–4563.

135. Laurentius, L.; Stoyanov, S. R.; Gusarov, S.; Kovalenko, A.; Du, R.; Lopinski, G. P.; McDermott, M. T. Diazonium-derived aryl films on gold nanoparticles: Evidence for a carbon-gold covalent bond. *ACS Nano* **2011**, *5*, 4219–4227.

136. Neu, C. P., & Genin, G. M. (Eds.). *Handbook of imaging in biological mechanics*; CRC Press, 2014.

137. Mooney, J. F.; Hunt, A. J.; McIntosh, J. R.; Liberko, C. A.; Walba, D. M.; Rogers, C. T. Patterning of functional antibodies and other proteins by photolithography of silane monolayers. *Proc. Natl. Acad. Sci. U. S. A.* **1996**, *93*, 12287–12291.

138. Tlili, A.; Jarboui, M. A.; Abdelghani, A.; Fathallah, D. M.; Maaref, M. A. A novel silicon nitride biosensor for specific antibody–antigen interaction. *Mater. Sci. Eng. C* **2005**, *25*, 490–495.

139. Yang, L.; Li, Y. AFM and impedance spectroscopy characterization of the immobilization of antibodies on indium–tin oxide electrode through self-assembled monolayer of epoxysilane and their capture of Escherichia coli O157:H7. *Biosens. Bioelectron.* **2005**, *20*, 1407–1416.

140. Mesnage, A.; Esnouf, S.; Jégou, P.; Deniau, G.; Palacin, S. Understanding the Redox-Induced Polymer Grafting Process: A Dual Surface-Solution Analysis. *Chem. Mater.* **2010**, *22*, 6229–6239.

141. Kariuki, J. K.; McDermott, M. T. Nucleation and growth of functionalized aryl films on graphite electrodes. *Langmuir* **1999**, *15*, 6534–6540.

142. Kariuki, J. K.; McDermott, M. T. Formation of Multilayers on Glassy Carbon Electrodes via the Reduction of Diazonium Salts. *Langmuir* **2001**, *17*, 5947–5951.

143. Pinson, J. Attachment of Organic Layers to Materials Surfaces by Reduction of Diazonium Salts. In *Aryl diazonium salts new coupling agents in polymer and surface science*; Mohamed Mehdi Chehimi, Ed.; John Wiley & Sons, 2012; p. 335.

144. Ru, J.; Szeto, B.; Bonifas, A.; McCreery, R. L. Microfabrication and integration of diazonium-based aromatic molecular junctions. *ACS Appl. Mater. Interfaces* **2010**, *2*, 3693–3701.

145. Mahmoud, A. M.; Bergren, A. J.; McCreery, R. L. Derivatization of Optically Transparent Materials with Diazonium Reagents for Spectroscopy of Buried Interfaces. *Anal. Chem.* **2009**, *81*, 6972–6980.

146. Hurley, B. L.; McCreery, R. L. Covalent Bonding of Organic Molecules to Cu and Al Alloy 2024 T3 Surfaces via Diazonium Ion Reduction. *J. Electrochem. Soc.* **2004**, *151*, B252.

147. Matrab, T.; Nguyen, M. N.; Mahouche, S.; Lang, P.; Badre, C.; Turmine, M.; Girard, G.; Bai, J.; Chehimi, M. M. Aryl Diazonium Salts for Carbon Fiber Surface-Initiated Atom Transfer Radical Polymerization. *J. Adhes.* **2008**, *84*, 684–701.

148. Shewchuk, D. M.; McDermott, M. T. Comparison of Diazonium Salt Derived and Thiol

Derived Nitrobenzene Layers on Gold. *Langmuir* **2009**, *25*, 4556–4563.

149. Laurentius, L.; Stoyanov, S. R.; Gusarov, S.; Kovalenko, A.; Du, R.; Lopinski, G. P.; McDermott, M. T. Diazonium-Derived Aryl Films on Gold Nanoparticles: Evidence for a Carbon–Gold Covalent Bond. *ACS Nano* **2011**, *5*, 4219–4227.

150. Skoog, H. and N. *Principles of Instrumental Analysis. Fifth Editon*.

151. http://wiki.utep.edu/download/attachments/51216393/XPS.pdf.

152. Zheng, W.; Hurk, R. van den; Cao, Y.; Du, R.; Sun, X. Aryl Diazonium Chemistry for the Surface Functionalization of Glassy Biosensors. *Biosensors* **2016**.

153. Solak, A. O.; Eichorst, L. R.; Clark, W. J.; McCreery, R. L. Modified Carbon Surfaces as "Organic Electrodes" That Exhibit Conductance Switching. *Anal. Chem.* **2003**, *75*, 296–305.

154. Pinson, J.; Podvorica, F. Attachment of organic layers to conductive or semiconductive surfaces by reduction of diazonium salts. *Chem. Soc. Rev.* **2005**, *34*, 429–439.

155. Combellas, C.; Kanoufi, F.; Pinson, J.; Podvorica, F. I. Time-of-flight secondary ion mass spectroscopy characterization of the covalent bonding between a carbon surface and aryl groups. *Langmuir* **2005**, *21*, 280–286.

156. Liu, Y. C.; McCreery, R. L. Raman spectroscopic determination of the structure and orientation of organic monolayers chemisorbed on carbon electrode surfaces. *Anal. Chem.* **1997**, *69*, 2091–7.

157. Xia, Y.; Zhao, X. M.; Whitesides, G. M. Pattern transfer: Self-assembled monolayers as ultrathin resists. *Microelectron. Eng.* **1996**, *32*, 255–268.

158. Wasserman, S. R.; Tao, Y. T.; Whitesides, G. M. Structure and reactivity of alkylsiloxane monolayers formed by reaction of alkyltrichlorosilanes on silicon substrates. *Langmuir* **1989**, *5*, 1074–1087.

159. Mesnage, A.; Esnouf, S.; Jégou, P.; Deniau, G.; Palacin, S. Understanding the redox-induced polymer grafting process: A dual surface-solution analysis. *Chem. Mater.* **2010**, *22*, 6229–6239.

160. Dong, Y.; Shannon, C. Heterogeneous Immunosensing Using Antigen and Antibody Monolayers on Gold Surfaces wit h Electrochemical and Scanning Probe Detect ion. **2000**, *72*, 2371–2376.

161. Chen, G. Y.; Thundat, T.; Wachter, E. A.; Warmack, R. J. Adsorption-induced surface stress and its effects on resonance frequency of microcantilevers. *J. Appl. Phys.* **1995**, *77*, 3618–3622.

162. Karabalin, R. B.; Villanueva, L. G.; Matheny, M. H.; Sader, J. E.; Roukes, M. L. Stress-Induced Variations in the Stiffness of Micro- and Nanocantilever Beams. *Phys. Rev. Lett.* **2012**, *108*, 236101.